Communications of the
LUNAR AND PLANETARY
LABORATORY

Communications Nos. 184–195

ORIGINAL CON...
COLOR ILLUSTRA...

Volume 10   Part 1

THE UNIVERSITY OF ARIZONA

Communications of the
LUNAR AND PLANETARY
LABORATORY

Communications Nos. 184–195

Volume 10   Part 1

THE UNIVERSITY OF ARIZONA

1973

i

COMMUNICATIONS OF THE LUNAR AND PLANETARY LABORATORY

These *Communications* contain research reports and observational summaries by the staff of the Lunar and Planetary Laboratory. The observational data are mostly obtained with the LPL telescopes and the NASA-Ames high-altitude facility. The articles may include rather extensive references to meteorological or geophysical material as would be expected in short monographs. Certain observational areas, such as asteroids and comets, are not systematically included as they are published in the astronomical journals. Occasionally, journal articles are reprinted in the *Communications*, when the continuity of the subject matter warrants it. Tabular material too bulky or specialized for regular journals may be included if future use of such material makes this desirable. The *Communications* are issued as separate numbers, but they are paged and indexed by volumes.

The *Communications* are mailed to observatories and to laboratories known to be engaged in planetary, interplanetary or geophysical research in exchange for their reports and publications. The University of Arizona Press can supply at cost copies to other libraries and interested persons.

The University of Arizona   GERARD P. KUIPER
Tucson, Arizona

NO. 184   REFLECTION SPECTRA OF SOLIDS OF PLANETARY INTEREST

by Godfrey T. Sill, O. Carm.

July 25, 1973

ABSTRACT

   This paper reproduces the spectra of solids which might be
found on the surfaces of planetary bodies or as solid condensates
in the upper planetary atmosphere. Among these are spectra of
various iron compounds of interest in the study of the clouds of
Venus. Other spectra are included of various sulfides, some at low
temperature, relevant to the planet Jupiter. Meteorite and coal
abstracts are also included, to illustrate dark carbon compounds.

1

1.   Earlier Results;   Method of Measurement

In his paper on the Venus cloud layers, G. P. Kuiper (1969) included a number of reflection spectra supplied by this author.   These were obtained by means of a Zeiss Spectroreflectometer, courtesy of Dr. Robert Feltham of the University of Arizona Department of Chemistry.   The instrument measures the reflection spectra of solids by illuminating the sample with monochromatic light at a 45° angle of incidence, and detecting the reflected light normal to the surface of the sample by an appropriate detector (PbS in the IR, photo-multiplier in the visible and UV).   In all cases, the radiation detected is normalized to 100% by setting the slit width of the monochromator such that the standard (finely-powdered optical LiF) registers 100% on the galvanometer. The spectrum was sampled every 100Å in the UV, every 200Å in the visible, and every 500Å in the IR.   The sample and standard are mounted on the same movable holder.   First the standard is placed in the beam, the galvanometer is set to 100, and then the sample moved into place and its reflection measured.   The spectra in this paper and in *LPL Communication No. 101* are the smooth curves drawn through the measured values.

Occasionally, the sample reflects light better than the standard LiF.   In some cases the sample reflects in a specular fashion off crystal surfaces, more so than does the standard.   This is particularly true in the UV < 3000Å.   At times the sample is drier than the LiF, so that the water absorption at 2.0μ may show as a positive feature.   Some samples cooled to liquid-nitrogen temperature had liquid-nitrogen boiling on the surface of the sample and standard, both covered with quartz plates.   This is particularly observed in Figure 1*l*.   It is stressed that whenever the sample was covered with a protective sheet of poly-ethylene or 1 mm thick quartz, the standard was likewise covered.

2.   The New Spectra

Figure 1 reproduces the absorption spectra of various sulfur compounds which might be possible constituents of the clouds of Jupiter and Saturn, or surface deposits of the satellites of the giant planets.

Figures 1*a*, *b*, and *c* are the reflection spectra of ammonium sulfide, pro-duced by reacting the two gases H_2S and NH_3 in an air-free environment.   Origi-nally the ammonium sulfide is white in color.   If air is introduced, the oxygen causes the decomposition of sulfide (S^{2-}) or hydrogen sulfide (HS^-) ions into polysulfide ions (S_x^{2-}), where the length of the sulfur chain increases with continued oxidation, until the production of a long-enough chain, probably S_8^{2-}, results in a cyclic molecule S_8, which is the molecule of elemental sulfur. Upon evacuating some yellow samples of ammonium sulfide, i.e., removing the NH_3 and H_2S decomposition gases, a yellow crust of elemental sulfur remains.   It should be pointed out that exposure to ultraviolet radiation (principally Hg 2537Å) produced the same effect as exposure to oxygen.   Solar UV should be ca-pable of similarly oxidizing sulfide to polysulfide in the upper atmospheres of planets.

The hydrogen sulfide equivalent to the polysulfide is shown in Figure 1*d*. This compound, H_2S_5, is extremely labile and decomposes spontaneously into H_2S gas and S_8 at room temperature.   At lower temperatures (-30°C) it can be stored for months in a sealed container.
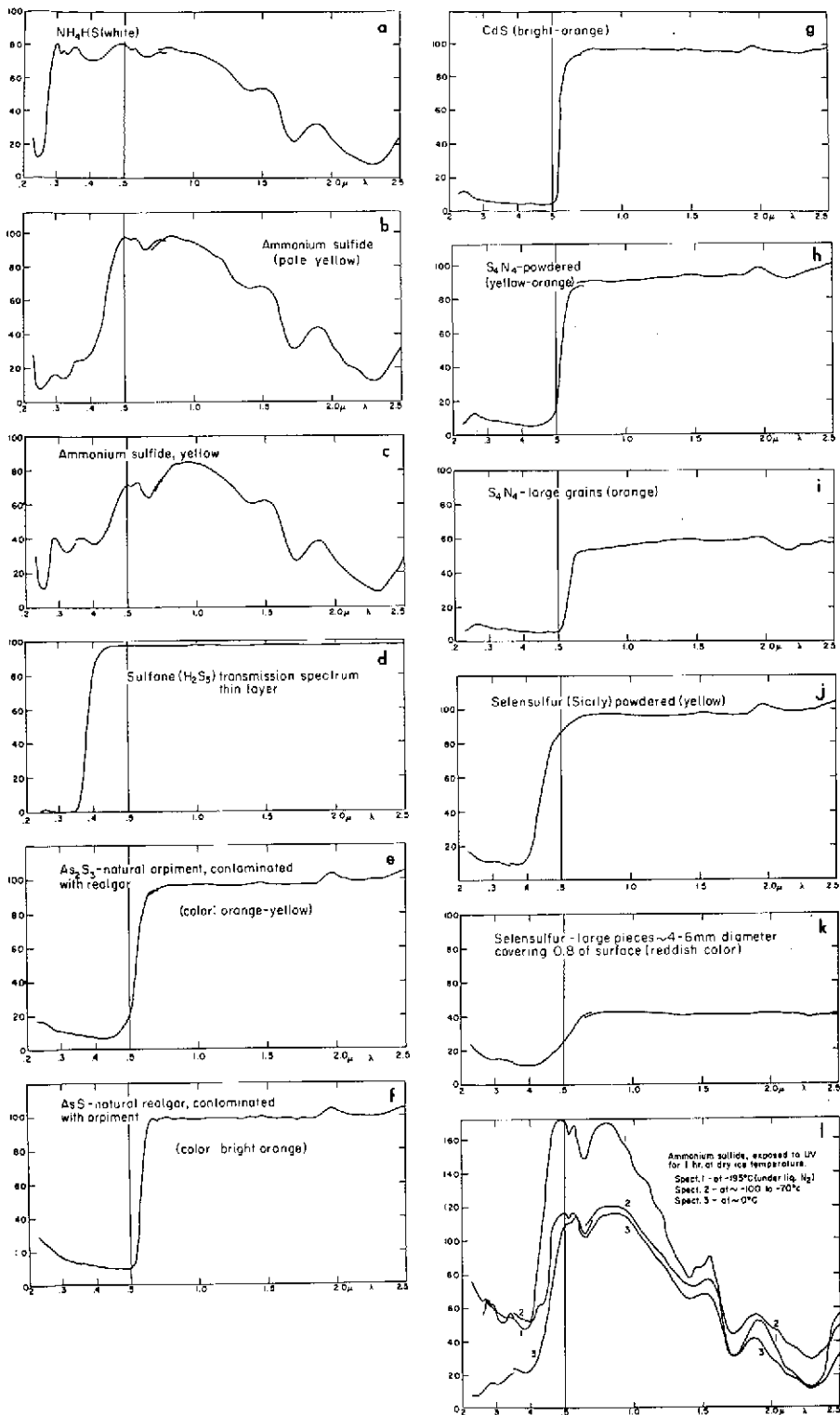
Figure 1

Ammonium sulfide cooled to liquid nitrogen temperature and intermediate temperatures is shown in Figure 1*l*. Problems with boiling liquid N_2 and the reflection off the polished surfaces of the protective quartz plates caused a reflectivity greater than the standard LiF. The positions of the absorptions are, however, accurate. It is interesting to observe the increase in absorption and the sharpness of the absorption caused by the lower temperatures in the features centered on 5350 and 6330Å.

Cadmium and arsenic sulfides (Fig. 1*e, f, g*) are representative of possible satellite surface constituents. Both they and their elements are volatile, although the metals are not cosmically abundant. Tetranitrogen tetrasulfide, S_4N_4, (Fig. 1*h, i*) is a labile, even explosive, compound that can be formed by the reaction of ammonium sulfide in liquid ammonia. It is usually formed under highly selective laboratory conditions, and is added simply to show that various orange-colored sulfides are difficult to identify conclusively on the basis of their solid reflection spectra.

Selensulfur (sulfur contaminated with a few-percent selenium) shows a spectrum (Fig. 1*j, k*) similar to sulfur but with an absorption further into the visible than pure sulfur.

Figure 2*a-g* contain compounds of interest to the clouds of Venus, a continuation of the spectra produced in Kuiper's Venus paper (1969). Figure 1*a-d* show the spectra of ferrous chloride exposed to simulated Venus surface conditions. If ferrous chloride, hydrated to a small extent (about $1H_2O$), is sublimed at 500°C under nitrogen gas, the spectrum is different from pure $FeCl_2$ (anhydrous) and $FeCl_2 \cdot 2H_2O$. The coordinated Fe^{2+} ion absorption at 1.0μ, and the H_2O hydration at 2.0μ, are evident, as are the charge transfer bands in the UV. The same substance exposed to air for three days is seen in Figure 2*b*. The coordinated Fe^{2+} ion at 1.0μ is more intense, as are the charge transfer bands in the UV. Figure 2*c* shows the reddening (oxidizing) of $FeCl_2$ when sublimed in hot CO_2 (500°C). Upon exposure to air, the ferrous (or ferric) ion is coordinated by water, observed at 1.0μ, and the water of hydration, evident at 2.0μ.

Ferric sulfate with varying water of hydration is shown in Figure 2*e, f*. The addition of sulfuric acid to ferric sulfate produced a cream-colored paste whose spectrum is shown in Figure 2*g*. The liquid paste produced greater penetration and absorption in the IR observed longward of 1.5μ. It might be mentioned that the absorption characteristics of hydrated sulfates and sulfuric acid led the author to consider whether sulfuric acid itself might not be the main constituent of the Venus clouds (Sill 1972).

Figure 3*a* shows an iron compound, coordinated with ammonia instead of water. This can be compared with the equivalent aquo-complexed ferric chloride, Figure 6 (*o*) in *LPL Communication No. 101*. The ultraviolet is virtually identical, but the visible absorption is quite different, as is obvious from their colors: $FeCl_3 \cdot 6H_2O$ is bright yellow; and $FeCl_3 \cdot 6NH_3$ is buff-colored. In the infrared, the coordinating NH_3 atom exhibits distinct ammonia-absorption bands versus the water bands of the aquo complex.

Some carbon compounds and the Orgueil carbonaceous chondrite are shown in Figure 3*b, c, d*. The Orgueil meteorite is a very dark specimen, darker than coal in the infrared. The overall dark-green color of the meteorite is due to the large
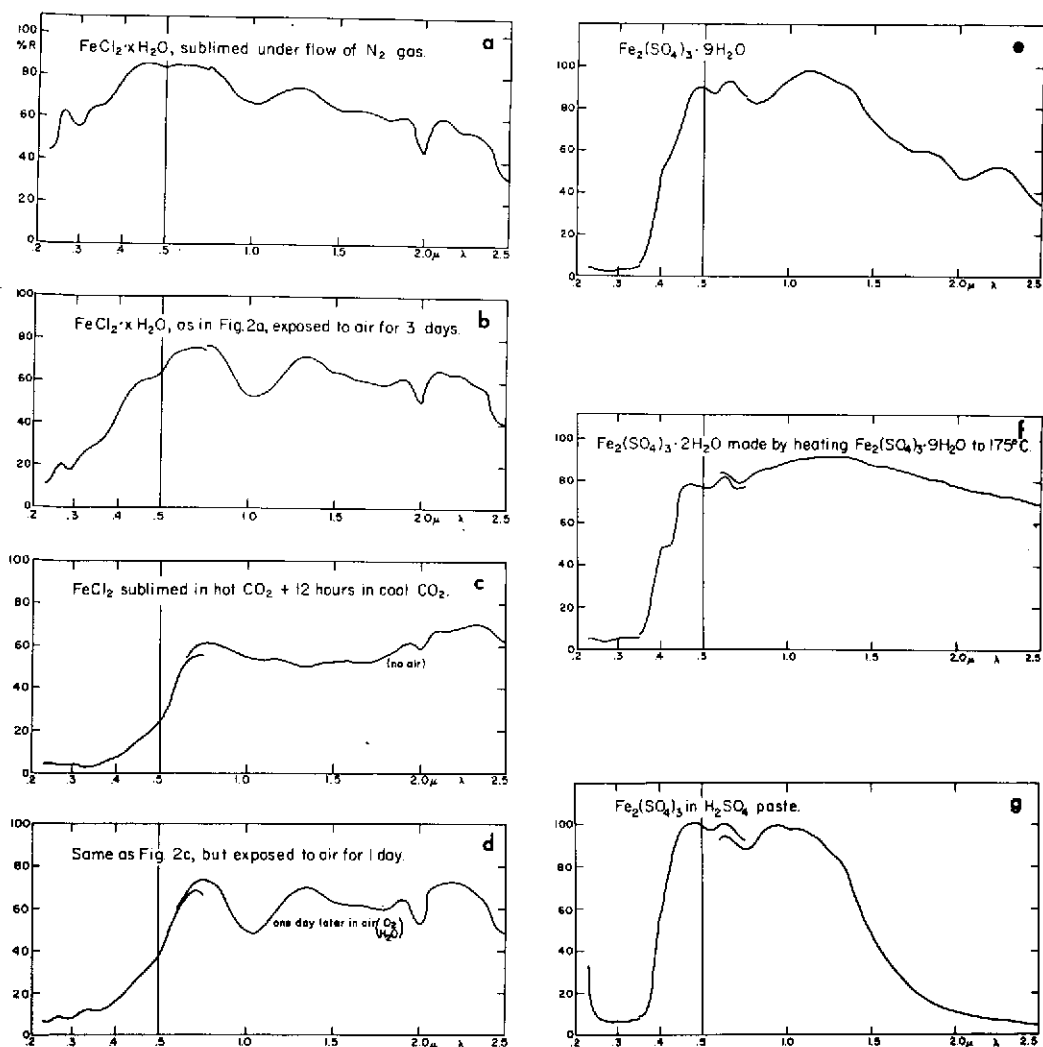
Figure 2

quantity of chlorite-type micaceous mineral present, an iron-bearing layer lattice silicate. Figure 3*d* is the spectrum of bituminous coal, not a likely object *per se* to be found on a planet, but illustrative of the chemical processes which have occurred in various carbon-bearing meteorites. Two extracts of bituminous coal are shown in Figure 3*c*. These have interesting IR reflection properties. They follow the overall IR brightening of bituminous coal, but show absorption features lacking in coal.

Figure 3*e* reproduces the spectra of elemental sulfur, both at room temperature and at about -160°C, cooled by nitrogen gas boiling off a reservoir of liquid nitrogen. The color of sulfur immersed in liquid nitrogen is *white* or, more exactly, a *faint pale green*. This is true even for large sulfur crystals a few mm thick. Liquid sulfane, H_2S_5, whose transmission spectrum is seen in Figure 1*d*, behaves
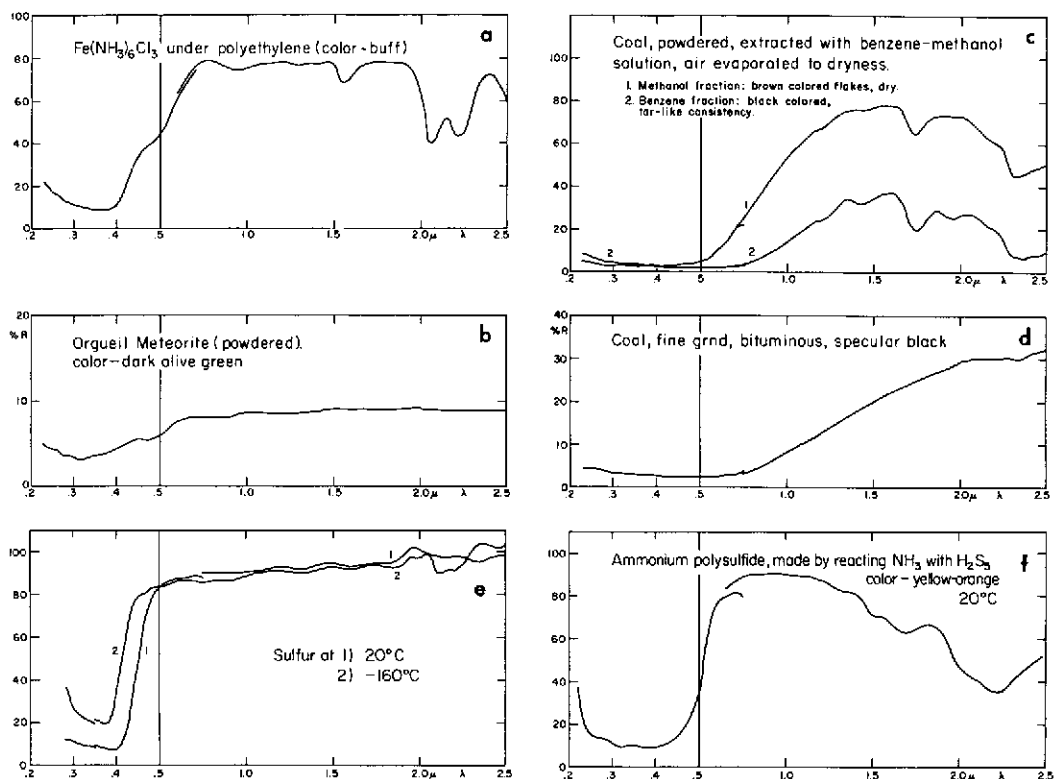
Figure 3

differently. When cooled to liquid-nitrogen temperature, sulfane still retains its *yellow* color, though not as intense as at room temperature. It should be noted that the transmission spectrum of Figure 1*d* is of a very thin layer, one drop squeezed between quartz plates, pale yellow in color. A thicker layer would cause the absorption wing to shift into the visible region of the spectrum.

Figure 3*f* shows the reflection spectrum of ammonium polysulfide at room temperature. The material was produced by reacting gaseous ammonia with liquid sulfane, H_2S_5, cooled by powdered dry-ice. Some decomposition of sulfane occurred in the reaction, namely, bubbles of H_2S were observed. The ammonium polysulfide produced ranged in color from yellow to a red-brown, russet color. The material was ground in a mortar. Unfortunately, the grinding process resulted in the apparent destruction of the russet polysulfide, especially as the dry-ice sublimed and the material was warmed up. The final product was an organge-yellow powder at room temperature, apparently quite stable. In the spectrum of Figure 3*f* it is evident that the ultraviolet and visible absorptions of polysulfide have increased in intensity, such that the absorption at 0.65μ has been lost in the long-wavelength wing of the polysulfide absorption. The ammonium ion absorptions in the IR are somewhat subdued versus the deeper absorptions of Figure 1. This is due to two sources: first, there is some elemental sulfur present with the polysulfide; second, the molar fraction of ammonium ion decreases as the polysulfide ion increases the length of the S chain.

3. Conclusions

The spectra here reproduced fill a need to identify constituents of plane-
tary surfaces and cloud layers. Caution must be utilized in making unequivocal
identifications of planetary materials on the basis of solid or particle spectra
alone. As can be seen in the illustrations, solids of different chemical com-
position can exhibit similar reflection spectra. On the other hand, there are
many features that are truly diagnostic and can indeed furnish tentative iden-
tifications. This is true especially for the bands of coordinating compounds in
metal complexes, and for the peculiar absorptions of the ammonium polysulfides.

REFERENCES

Kuiper, G. P. 1969, "Identification of the Venus Cloud Layers", *LPL Comm. No.
   101, 6,* 229-250.
Sill, G. T. 1972, "Sulfuric Acid in the Venus Clouds", *LPL Comm. No. 171, 9,*
   191-198.

NO. 185   REFLECTION SPECTRA, 2.5-7μ, OF SOME SOLIDS OF

PLANETARY INTEREST

by U. Fink and S. D. Burk

November 15, 1971

ABSTRACT

Reflection spectra of 42 compounds of possible planetary interest were run from 2.5 to 7μ. They were supplemented by some transmission spectra extending the wavelength coverage to 15μ. The spectra were organized according to their constituent radicals and an attempt was made at the identification of the absorption features.

1.   Introduction

In order to interpret the albedo measurements of the planets and, if possible, determine the composition of the surface minerals or the dust particles in a cloudy atmosphere, laboratory comparison studies must be made. The present investigation was stimulated by the proposal of G. P. Kuiper (1969) that the Venus cloud particles are made of ferrous chloride-dihydrate ($FeCl_2 \cdot 2H_2O$).

Some of our spectra of this substance have already been published by Dr. Kuiper (1969) in his article *LPL Communication No. 101*.   In this paper we present reflection spectra of 42 substances, and a few transmission spectra serving as a check and for comparison.   Two main criteria can be applied to the selection of materials: (a) The elements constituting the compound should have a reasonable cosmic and terrestrial abundance; (b) Chemical equilibrium considerations should be favorable to the compound's manufacture and existence under the conditions known to prevail at planetary surfaces or clouds.   The second criterion should not be taken too strictly, since non-equilibrium processes, in particular volcanic action, may play a major role in determining the planetary constituents visible to us.   Only inorganic materials were considered in this study.

2.   Experimental Procedure

The spectra shown were taken with a Perkin and Elmer model 137 double-beam spectrophotometer.   The instrument was modified for the reflection measurements by the arrangement shown in Figure 1.   The samples were ground to a fine powder with a mortar and pestle.   The particle diameters were approximately $25-50\mu$, as measured with a microscope. The powder was placed in the sample beam on a piece of black velvet while a similar piece with sulfur powder was placed in the reference beam. A run of sulfur-vs.-sulfur preceded each sample-vs.-sulfur run.   Because of the low intensity of the scattered light, the instrument was difficult to adjust and balance.   Most samples were analytical-reagent-grade chemicals from the University chemistry storeroom. In a few cases (particularly $FeCl_2$) they were prepared by Fr. G. Sill.

Transmission spectra were obtained with the KBr-pellet technique.   A mixture of KBr powder and sample were put into a small threaded die of about 1 cm bore. Two bolts pressed the powder into a thin transparent pellet, which was inserted with the die into the sample beam.   A pellet of pure KBr was used in the reference beam.   A run of KBr-vs.-KBr was again used to balance the instrument before a sample run.   The transmission spectra *a-d* in Figure 2 were taken without weighing the KBr or sample powder.   For the later runs however we tried to obtain more quantitative data.   A KBr pellet of 75 mg KBr was found to produce a suitable pellet.   The amount of sample added was usually about 3-6 mg.   It is listed for each spectrum in Figures *2e-h*.
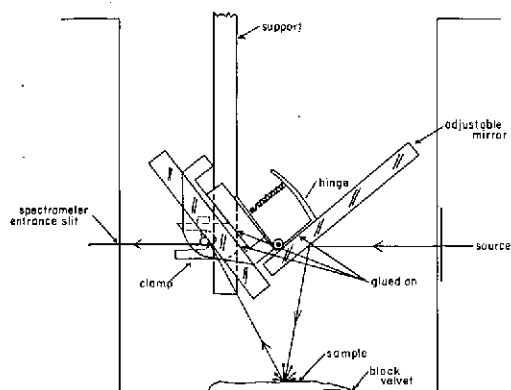
Figure 1   Arrangement for taking reflection spectra
with the Perkin & Elmer model 137 spectrophotometer

3.   Transmission Spectra

When we compared our reflection spectra with transmission spectra listed in Miller and Wilkins (1952) and the Sadtler index (1965), considerable differences were found.   In particular the nitrates and carbonates showed more features in our reflection curves than in their transmission spectra.   The three characteristic reflection peaks of the nitrates at 3.6μ, 4.1μ, and 4.7μ were absent in the transmission spectra.   We therefore decided to run some transmission spectra of the nitrates ourselves (Fig. 2ℯ).   The three peaks were practically absent in our first spectrum (Curve 1).   However, they appeared when we increased the concentration

NOT REPRODUCIBLE

Figure 2   Transmission spectra.   Breaks in spectra indicate adjustment of instrument.   Dashed lines are run at higher gain

(Curve 2), and when the gain was increased, so that the 100 per cent level was above the top of the chart, the three peaks showed up with a distinctness approaching the reflection sp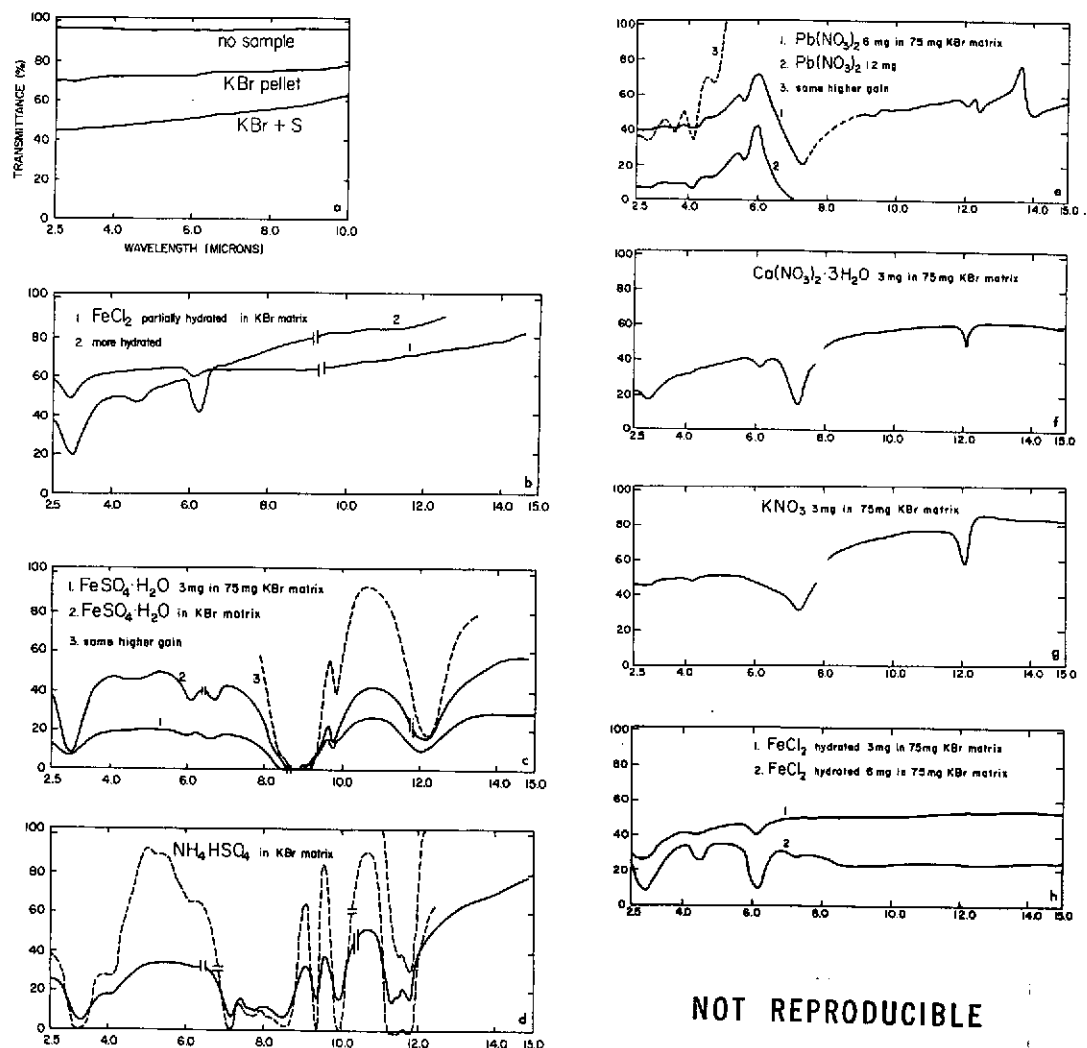ectra. This case shows very clearly that although in most instances reflection and transmission spectra are basically similar, one cannot be used to extrapolate to the other since the relative intensities of the peaks may be quite different.

The transmission spectra taken are presented in Figure 2a-h. Where the lines are broken, the gain and time constant of the instrument were readjusted. For spectra with dashed lines the gain of the instrument was increased so that the 100 per cent level is above the top of the chart. Transmission spectra were run for the following reasons: (a) to make sure that sulfur powder has no absorptions in our region of interest, since it was used as our reflectance standard; (b) to provide a check on the reality of the absorption features obtained in reflection; (c) to extend the coverage to longer wavelengths; (d) to obtain some quantitative information about the strengths of the absorptions peaks; and (e) to obtain sharper features and thus more accurate wavelength determination of the peaks.

4. Reflection Spectra

Light from the source undergoes two processes when it strikes a powder: scattering and absorption. To treat the problem of the returning light quantitatively we must know the scattering and the absorption cross sections as a function of wavelength. The scattering cross section depends on the particle size, shape and index of refraction. The absorption cross section is mostly determined by the energy level and the dipole strengths of the allowed transitions in the material. The relative magnitudes of the two cross sections can cause the reflection and transmission spectra to have quite different appearances. (An example for the nitrates is given above). In this paper we have not made a quantitative study of the two cross sections, but are interested mainly in the diagnostic absorption peaks by which a substance can be identified in a spectrum of an object under study.

For very fine particles the scattering cross section can be much larger than the absorption cross section. The light gets scattered before it can enter the particles (where the absorption takes place). No sharp features will therefore be found in reflection. On the other hand, if the particle absorbs very strongly, the absorption features become saturated and again a relatively featureless spectrum results. An example is the spectrum of $MgCO_3$ and NH_4Cl where the *strong* absorptions (present for a block and for coarse particles) are masking any *detailed* absorption features. The same effect occurs when there is much water of hydration present. Examples are hydrated and dehydrated $NiCl_2$ and $CaCl_2$ and hydrated $Ca(NO_3)_2$ which lacks the characteristic structure of the other nitrates. The spectra of the hygroscopic sulfates show very few detailed features because of this effect.

The reflection spectra are displayed in Figure 3. It is estimated that past 7μ thermal self-emission competes with the low-level scattered light from the sample. (The black body maximum of a sample at room temperature occurs near 10μ). All curves are therefore dashed past 7μ. Sulfur powder which has a high uniform reflectivity was used as a comparison in all the runs. To make sure that sulfur has no absorptions in our region of interest it was run in transmission (Fig. 2a) with the KBr pellet technique, and indeed no absorptions were found.
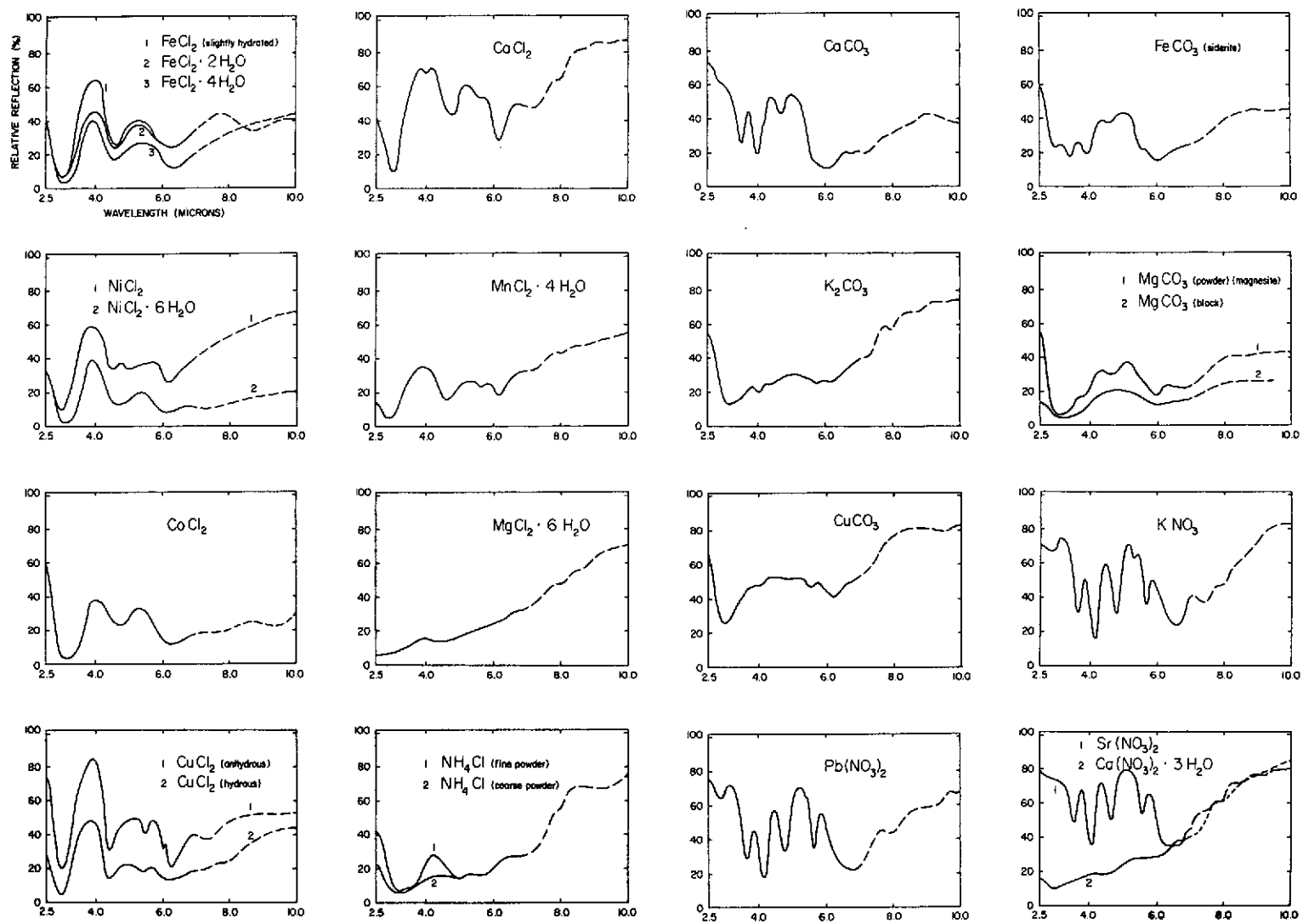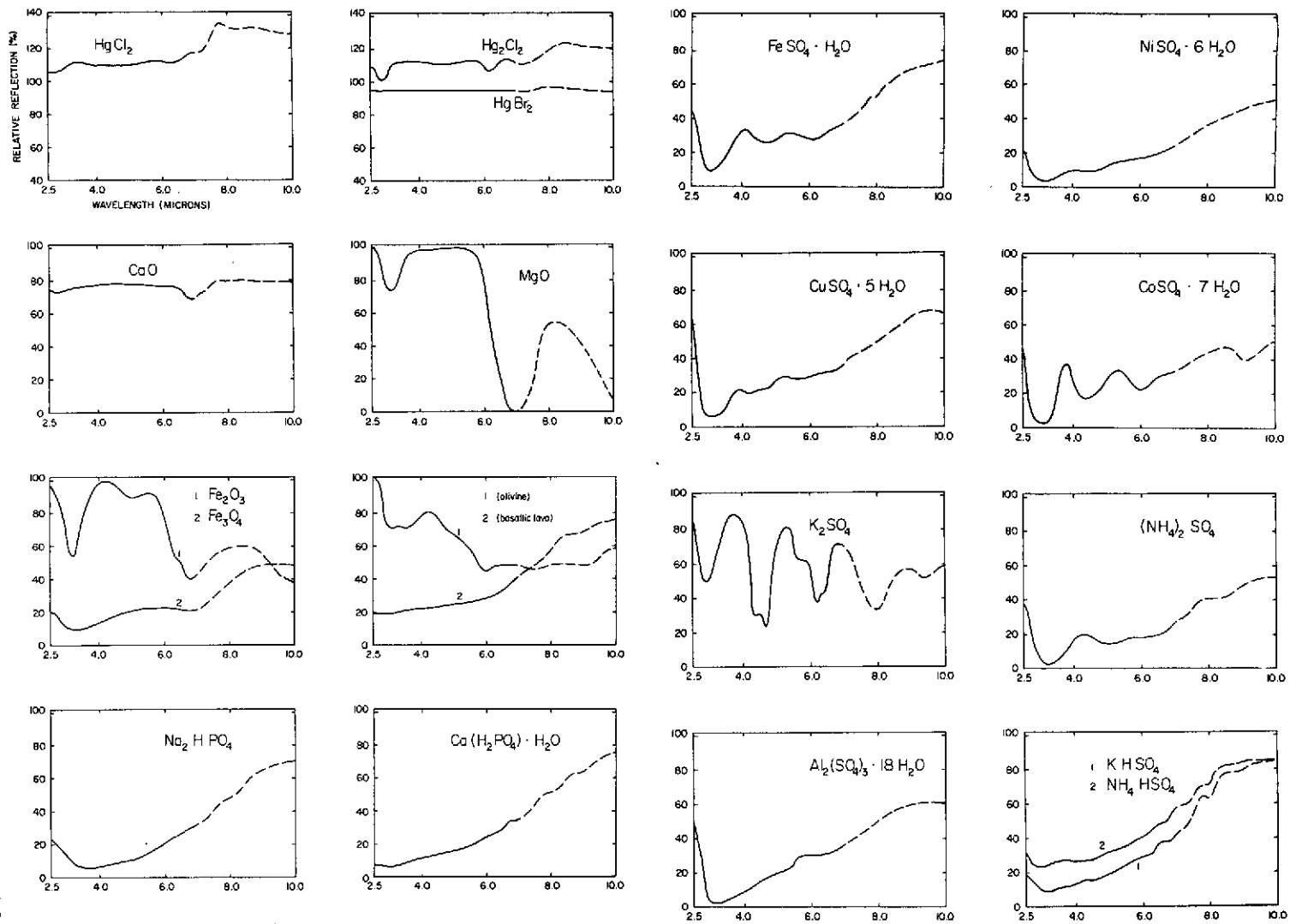
Figure 3a Reflection spectra. The spectra are dashed past 7μ because of
sample self-emission and therefore uncertainty of the spectrum

Figure 3*b* (continued)

5.   Identification of Absorption Peaks

Over a broad wavelength range, the spectra obtained from solids arise prin-
cipally from three major mechanisms. In the most energetic mechanism, electrons
of the atoms or ions making up the crystal lattice jump between energy levels
which are created by the electric field of the crystal lattice. Individual atoms
or molecules can no longer be considered as separate units. The theory describ-
ing such a process is commonly called crystal-field or ligand-field theory. The
spectra obtained usually lie in the visible, ultra-violet or near-infrared region
below one micron. The least energetic process consists of crystal lattice vibra-
tions which cause absorptions in the far-infrared region of the spectrum, past
10-20µ. The pure rotational spectra of the molecules making up the crystal can
also be found in this region.

In this study we shall be concerned with the intermediate energy range, i.e.
infrared spectra between about 1µ and 20µ. These spectra can be explained by the
chemical-bond vibrations of the molecule. When a free, gaseous molecule is con-
densed into the liquid or solid state, the molecular vibrations persist with only
minor alterations: (a) The bands usually lose their rotational structure and become
much broader; (b) The frequencies of the free molecule shift slightly,usually to
lower values, due to the interaction with other molecules, and (c) new frequencies
which are absent in the gaseous state may appear. Some of these frequencies are for-
bidden in the gaseous state, but become allowed in the liquid or solid states due to
perturbations of neighboring molecules; or new frequencies may appear due to poly-
merization of the molecules. Basically, however, in an analysis of solid spectra
one can use the fundamental frequencies of the free molecule and the extensive
theory developed to explain the gaseous spectra (Herzberg 1945).

In identifying the spectra taken, there is one characteristic which helps
greatly in classifying the observed spectral frequencies. Although a molecule
may be fairly complex, there exist "characteristic" frequencies of certain groups
of molecules which persist even when that group is attached to different molecules.
Examples are the C-H and O-H stretching or bending frequencies or the natural fre-
quencies of radicals such as SO_4^{-2}. There are two conditions under which the group
frequencies persist well. In the first one, a light atom such as hydrogen is at-
tached to a heavy atom such as carbon or oxygen, so that most of the vibratory
motion is performed by the H atom. Attaching such a group to another molecule
does not change the motion of the light atom very much.. The other condition re-
quires that the natural frequencies and thus the "spring constant" of the groups
are quite different. No strong interactions between groups can then take place
and they vibrate essentially with their natural frequencies.

Below we discuss the major features of each group that is listed in Tables
I-VII, and any peculiarities shown by the group. Because a large number of these
substances hydrate very easily, many are contaminated with water of hydration and
the spectra of both the pure substance and its hydrate must be considered.

I. Carbonates:

The positions of the major absorption peaks are listed in Table I. Also
given are the fundamental frequencies of the carbonate ion taken from Herzberg
(op. cit., p. 178). Since the reflection spectra become uncertain at about 7µ,
the peak of the absorption listed as 6µ is probably farther in the infrared and

can then be identified as the strong fundamental ν_3. This agrees with transmission spectra by Miller and Wilkins (*op. cit.*) and the Sadtler index (*op. cit.*). The identification of the other absorptions follows the combination principle and appears to be quite reasonable. Characteristic of $CaCO_3$ and $FeCO_3$ is the double peak at 2.85 and 3.45μ. This double peak coalesces into a single feature for K_2CO_3 and $CuCO_3$.

II. Nitrates:

The nitrates possess the same structure as the carbonates (plane symmetric) and the fundamental frequencies are quite similar. The nitrate spectra are therefore not too different from the carbonates. However, the nitrates show in reflection a distinct triple structure at 2.9, 3.6, and 4.1μ. Three nitrates were run in transmission: lead nitrate, hydrated calcium nitrate, and potassium nitrate. They showed that, as in the case of the carbonates, the strong absorption near 6.6μ can be attributed to the fundamental ν_3 at 7.15μ. Lead nitrate was run at the highest concentration and showed the three peaks which are so characteristic in reflection. Past the fundamental ν_3 it showed the fundamentals ν_1 (at 1050 cm^{-1}), ν_2 (at 830 cm^{-1}) and ν_4 (at 720 cm^{-1}). The fundamentals ν_1 and ν_2 seem to be split. Potassium and calcium-nitrate only showed the fundamentals ν_2 and ν_3, with the latter having in addition the water absorptions.

III. Sulfates and Bisulfates:

Sulfates are tetrahedral molecules and therefore have only four fundamentals (instead of the expected nine) of which only two are infrared active. All except K_2SO_4 contained considerable water of hydration so that the spectra are rather flat with the most conspicuous features the OH stretch frequency at 3300 cm^{-1} and the bend frequency at 1600 cm^{-1}. Potassium sulfate shows other distinct structure for which an identification is given. The consistent feature at 4.7μ is either due to water of hydration or is characteristic of the ion. Iron sulfate and ammonium bisulfate in transmission show a host of features, not all of which could be classified. Identified were the fundamentals ν_3, ν_2, and ν_4 of the ammonia ion and the fundamentals ν_3 and ν_1 of the sulfate ion plus some combination bands. The fundamental ν_4 of the sulfate ion seems to be missing in both.

IV. Chlorides:

These constitute the largest group of samples that were run because of their possible importance for the Venus clouds (Kuiper, *op. cit.*). Since all the chlorides hydrate easily, the OH stretch and bend frequencies show rather prominently. There is in addition a consistent feature at 2120 cm^{-1}. This can be tentatively attributed to an overtone of a metal-chloride (M-Cl) stretch frequency. However, most of these frequencies in diatomic molecules (Herzberg 1950) group around 300 cm^{-1} and 800 cm^{-1}, so that a rather high overtone would be required. More probably the peak is due to water of hydration since it is almost coincident with the unidentified peak in the sulfates. Reflection and transmission spectra of $FeCl_2$ were quite similar and thus serve as a check on each other. No major features were found past the water absorption at 6.3μ.

V. Ammonium Chloride:

The chloride of ammonia represents a special case due to the presence of the ammonium radical, which has much higher fundamental frequencies than any of the radicals discussed so far. (Table V). The fundamental ν_1 is not infrared active, but all of the others are and can be identified with absorption features in the spectrum. There is an unidentified absorption at 5.0μ which again is either a water of hydration peak or a NH_4-Cl stretch overtone.

VI. Oxides:

For the oxides it was difficult to identify any of the observed absorption frequencies. The fundamental frequencies of the diatomic oxide molecules are quite low (Table VI) so that it is difficult to associate any of the observed frequencies with some overtone band. In addition many of the oxides hydrate quite easily and form hydroxides which have a different structure from the pure oxide. The OH bands are therefore present with the OH bend frequency slightly shifted. It looks as if the absorptions at 4.85μ and 6.15μ may be characteristic of the FeO structure. Since olivine is composed mainly of FeO and SiO_2 the iron oxide peaks are observed together with the absorption at 3.6μ attributed to quartz.

VII. Potassium Cyanide:

Two water-of-hydration peaks show up in the spectrum in addition to the fundamental CN stretch frequency at 2100 cm^{-1} which should be quite characteristic for cyanides.

TABLES OF MAJOR ABSORPTION PEAKS AND THEIR TENTATIVE IDENTIFICATION

TABLE I   Carbonates CO_3^{-2}

Fundamental Frequencies(cm^{-1})	ν_1 1060		ν_2 880	ν_3 1410		ν_4 680
Compound	Major absorptions (microns)					
CaCO$_3$ (Calcite)	2.8		3.5	4.0	4.7	6.0
K$_2$CO$_3$		3.1		4.05		6.0
CuCO$_3$		3.0		4.0		6.2
FeCO$_3$ (Siderite)	2.9		3.4	3.9	4.6	5.6	6.0
MgCO$_3$ (Magnesite)	2.9			3.8	4.6	6.0
Av. position of absorptions(cm^{-1})	3480		2900	2530	2160	1790	1660
Tentative identifications (cm^{-1})	OH stretch or $2\nu_1+\nu_3$ 3530		$2\nu_3$ 2820	$\nu_1+\nu_3$ 2470	$2\nu_1$ 2120		OH bend or $2\nu_2$,ν_3 1660,1440

TABLE II   Nitrates NO_3^-

Fundamental Frequencies (cm^{-1})	ν_1 1050		ν_2 830		ν_3 1400		ν_4 720	
Compound	Major absorptions (microns)							
KNO_3	2.9		3.6	4.1	4.75	(5.3)	5.7	6.5
$Pb(NO_3)_2$	2.9		3.6	4.1	4.75	(5.4)	5.6	6.7
$Sr(NO_3)_2$	2.8		3.6	4.1	4.7		5.6	6.5
$Ca(NO_3)_2 \cdot 3H_2O$		3.1	strongly absorbent, decomposed while taking spectra					
Av. position of absorptions (cm^{-1})	3540		2780	2440	2120		1780	1520
Tentative identifications (cm^{-1})	OH stretch or $2\nu_1+\nu_3$ 3500		$2\nu_3$ 2800	$\nu_1+\nu_3$ 2450	$2\nu_1$ 2100		$\nu_1+\nu_4$ 1770	$\nu_3,(\nu_2+\nu_4)$ 1440,(1550)

TABLE III   Sulfates SO_4^{-2}

Fundamental Frequencies (cm^{-1})	ν_1 980	ν_2 450	ν_3 1100		ν_4 613	
Compounds	Major absorptions (microns)					
K_2SO_4	2.9	4.4	4.7	5.7	6.2	6.4
$FeSO_4 \cdot H_2O$	3.0		4.7		6.1	
$CuSO_4 \cdot 5H_2O$	3.0		4.5		6.0	
$NiSO_4 \cdot 6H_2O$	3.2		4.6		6.0	
$CoSO_4 \cdot 6H_2O$	3.2		4.5		6.0	
$(NH_4)_2 \cdot SO_4$	3.2		4.9		6.1	
$Al_2(SO_4)_3 \cdot 18H_2O$	3.1				6.0	
Bisulfates						
$KHSO_4$	3.3					
NH_4HSO_4	3.0					
Av. position of absorptions (cm^{-1})	3230	2280	2140	1760	1650	1560
Tentative identifications (cm^{-1})	OH stretch 3700	$2\nu_3$? 2200	H_2O combination or $\nu_1+\nu_3$ 2080	$\nu_3+\nu_4$ 1710	OH bend 1600	$\nu_2+\nu_3$ 1550

TABLE IV   Chlorides Cl^-

Compound	Major absorptions (microns)					
FeCl$_2$ (slightly hydrated)		3.0		4.6		6.3
FeCl$_2 \cdot$2H$_2$O		3.0		4.6		6.3
FeCl$_2 \cdot$4H$_2$O		3.0		4.6		6.3
CoCl$_2$		3.1		4.7		6.3
NiCl$_2$		2.9	4.4	4.9		6.1
NiCl$_2 \cdot$6H$_2$O		3.0		4.6		6.0
CuCl$_2$		3.0	4.4		5.4	6.3
CuCl$_2$ hydrated		3.0	4.3		5.4	6.3
MgCl$_2 \cdot$6H$_2$O		3.0		4.7		
CaCl$_2$		3.0		4.8	5.6	6.2
MnCl$_2 \cdot$4H$_2$O		2.9		4.6	5.7	6.2
HgCl$_2$	2.5					
Hg$_2$Cl$_2$	2.4				6.2	
Av. position of absorptions (cm^{-1})	4100	3300	2290	2120	1800	1590
Tentative identifications (cm^{-1})		OH stretch 3700	H$_2$O combinations (or M-Cl)			OH bend 1600

TABLE V   Ammonium Chloride

Fundamental frequencies of NH$_4$+ (cm^{-1})	ν_1 3030	ν_2 1680	ν_3 3130	ν_4 1400	
Compound	Major absorptions (microns and cm^{-1})				
NH$_4$Cl	3.2 3120	3.6 2780	5.0 2000	5.6 1780	7.0 1430
Tentative identifications	ν_3 3130	2ν_4 2800	M-Cl	ν_2 1680	ν_4 1400

TABLE VI   Oxides

Fundamental Frequencies (cm⁻¹)	CaO - 650		MgO - 785		FeO - 880	
Compound	Major absorptions (microns)					
CaO	2.7					6.8
MgO		3.1				6.9
Fe_2O_3		3.2		4.9	6.5	6.8
Fe_3O_4		3.3				7.0
Olivine		3.2	3.6	4.8	6.0	
Basaltic lava		3.0				
Av. position of absorption (cm⁻¹)	3710	3170	2780	2060	1630	1460
Tentative identifications (cm⁻¹)	OH stretch		$Si-O_2$	FeO absorption		OH bend

TABLE VII   Cyanide CN^{-1}

Fundamental Frequencies (cm⁻¹)	CN stretch - 2100	CN bend - 400	
Compound	Major absorptions (microns)		
KCN	3.2	4.8	6.2
Av. position of absorption (cm⁻¹)	3130	2080	1610
Tentative identifications (cm⁻¹)	OH stretch	CN stretch	OH bend

6.   Conclusion

The purpose of this study was to find diagnostic absorption peaks of solids which may occur on bodies of the solar system. Reflection spectra of about 40 substances and a few selected transmission spectra were therefore measured. Most of the absorption peaks measured were found to be *characteristic of a certain molecular group rather than a particular molecule*. For example, it would be difficult to tell KNO_3 from $Pb(NO_3)_2$ or $Sr(NO_3)_2$ merely by their infrared spectra.

On the other hand $CaCO_3$ and $CuCO_3$ show quite distinct differences. To help in showing both the similarities and differences of such groups, we have organized the spectra and tried to identify the peaks, using the principle of characteristic group frequencies. This simplifies the identification of any planetary features that might be detected and reduces the number of comparison spectra that must be taken.

From the differences found between the reflection and transmission spectra it can be seen that reliance on transmission spectra alone can give a false picture of the reflection spectrum of a substance. (Published transmission spectra can also be quite erroneous. In the case of NH_4HSO_4, the Sadtler (*op. cit.*) index spectrum agreed with ours, but the one in Miller and Wilkins (*op. cit.*) was quite different). It can of course be argued that the reflection spectrum of a dense powder does not represent a planetary albedo curve of particles mixed in a cloud. However, the wavelength position of the absorption peaks do not change with reflection or transmission, particle size, or number density. We feel that the reflection spectrum of the powder is the best alternative and provides a close approximation even to a planetary haze.

More serious is the *temperature dependence* of the absorption peaks of some of these substances. Sulfur powder for example changes from a yellow to a pure white when immersed in liquid nitrogen. In any future study, reflection spectra at different temperatures should be examined. With some care in making quantitative transmission measurements and with the help of a scattering theory such as the Kubelka-Munk theory (Kortüm 1969), a complex index of refraction as a function of wavelength may be found. This would then allow scattering calculations for a planetary haze to be made.

REFERENCES

Herzberg, G. 1945, MOLECULAR SPECTRA AND MOLECULAR STRUCTURE, Vol. II, D. Van Nostrand Co., Inc. (Princeton).
Herzberg, G. 1950, MOLECULAR SPECTRA AND MOLECULAR STRUCTURE, Vol. I, D. Van Nostrand Co., Inc. (Princeton).
Kortüm, G. 1969, REFLEXIONSSPEKTROSKOPIE (Springer Verlag, Berlin).
Kuiper, G. P. 1969, "Identification of Venus Cloud Layers", *LPL Comm. No. 101, 6*, 229-250.
Miller, F. A. and Wilkins, C. H. 1952, "Infrared Spectra and Characteristic Frequencies of Inorganic Ions", *Analytical Chem., 24*, 1253.
Sadtler Research Laboratory, Inc., Philadelphia, 1965.

NO. 186   INFRARED SPECTRA OF THE GALILEAN SATELLITES OF JUPITER [*]

by Uwe Fink, Nicolaas H. Dekkers[†] and Harold P. Larson

October 26, 1972

ABSTRACT

Spectra of the four Galilean satellites from 1 to 4μ were
obtained with a Michelson interferometer. The spectra show
that the albedo of Io is very nearly constant with wavelength;
no absorptions are found in the region observed. Europa and
Ganymede have large amounts of water ice on their surface. Cal-
listo shows some faint ice absorptions. Upper limits of 0.5
cm-atm (STP) corresponding to 6×10^{-8} atm partial surface pres-
sure were set for CH_4 and NH_3 on all four satellites.

A sensitive test for the detection of atmospheric constituents as well as the determination of surface composition is provided by spectra in the infrared past 1μ. Despite the great intrinsic interest in the properties of the four large satellites of Jupiter, it has not been possible to obtain even low-resolution spectra with good signal-to-noise ratio. Detector sensitivities and instrumentation techniques were not sufficiently advanced to tackle such relatively faint objects. The advent of Fourier spectroscopy with its multiplex and through-put advantages for the first time permitted the acquisition of good spectra at moderate resolution.

The excellent spectra of the Rings of Saturn (Kuiper, Cruikshank and Fink 1970) and the identification of their composition as water ice, gave us the impetus to obtain new and better spectra of the Galilean satellites. Preliminary data were obtained in May 1970 and were presented in a report to NASA (Kuiper 1971). These data showed quite clearly that water ice must be present on JII and JIII. However, some unidentified features close to the noise level required additional data so that final publication was delayed. It was then decided that an effort needed to be made to improve the interferometer. Thereupon, at the opposition of Jupiter this year (June 24, 1972), we succeeded in obtaining much better spectra of the four Galilean satellites.

Earlier, very low resolution spectra had been obtained by Kuiper in the U.S. and Moroz in Russia. Kuiper discussed spectrometer tracings taken with the 208-cm (82-inch) McDonald Observatory telescope of the four Galilean satellites at the American Astronomical Society meeting in 1957 (Kuiper 1957); they are reproduced in Figure 1 of the following *Communication*. They showed that JI and JIV roughly resembled the solar and lunar curves, but that JIII and particularly JII were markedly different. He stated: "This is most readily explained by assuming that JII and JIII are covered by H_2O snow". In 1965 Moroz published spectra (Moroz 1966) of the four satellites and concluded that the surfaces of Europa and Ganymede could very well be covered with ice, if not entirely, at least in a large part. Alternatively, he thought that it was also possible that the depressions in the spectra of Europa and Ganymede could be attributed to unknown atmospheric absorptions. Later Gromova, Moroz and Cruikshank (1970) published a spectrum of Ganymede between 1 and 1.7μ which showed an unidentifiable absorption at 1.55μ.

Our spectra are shown in Figure 1. They were taken with a low-resolution Michelson interferometer, delivered by Block Associates in 1967 and modified by us extensively in 1971-72. The new observations were made with the 154-cm (61-inch) Catalina Observatory telescope at the end of June and beginning of July of 1972. Thousands of scans, each of 1.0 sec duration, were recorded on analog magnetic tape and then later in the laboratory were digitized, coherently added, and transformed with an IBM 1130 computer. The resolution limit for the spectra, which are shown unapodized, is 25 cm^{-1}. The signal-to-RMS noise ratio for the four satellites, JI to JIV, is 56, 32, 56, and 47. One night (June 27, 1972) was much drier than the rest of the nights. Spectra of Io and Callisto were taken on this night so that the water-vapor bands for these two satellites are somewhat weaker in the average.

During the observations both Moon and stellar comparisons were taken. The Moon is not well suited as a comparison for the general albedo characteristics and the broad absorptions since it has significant thermal emission between 3 and 4 microns and its own albedo is not flat but increases slowly to longer
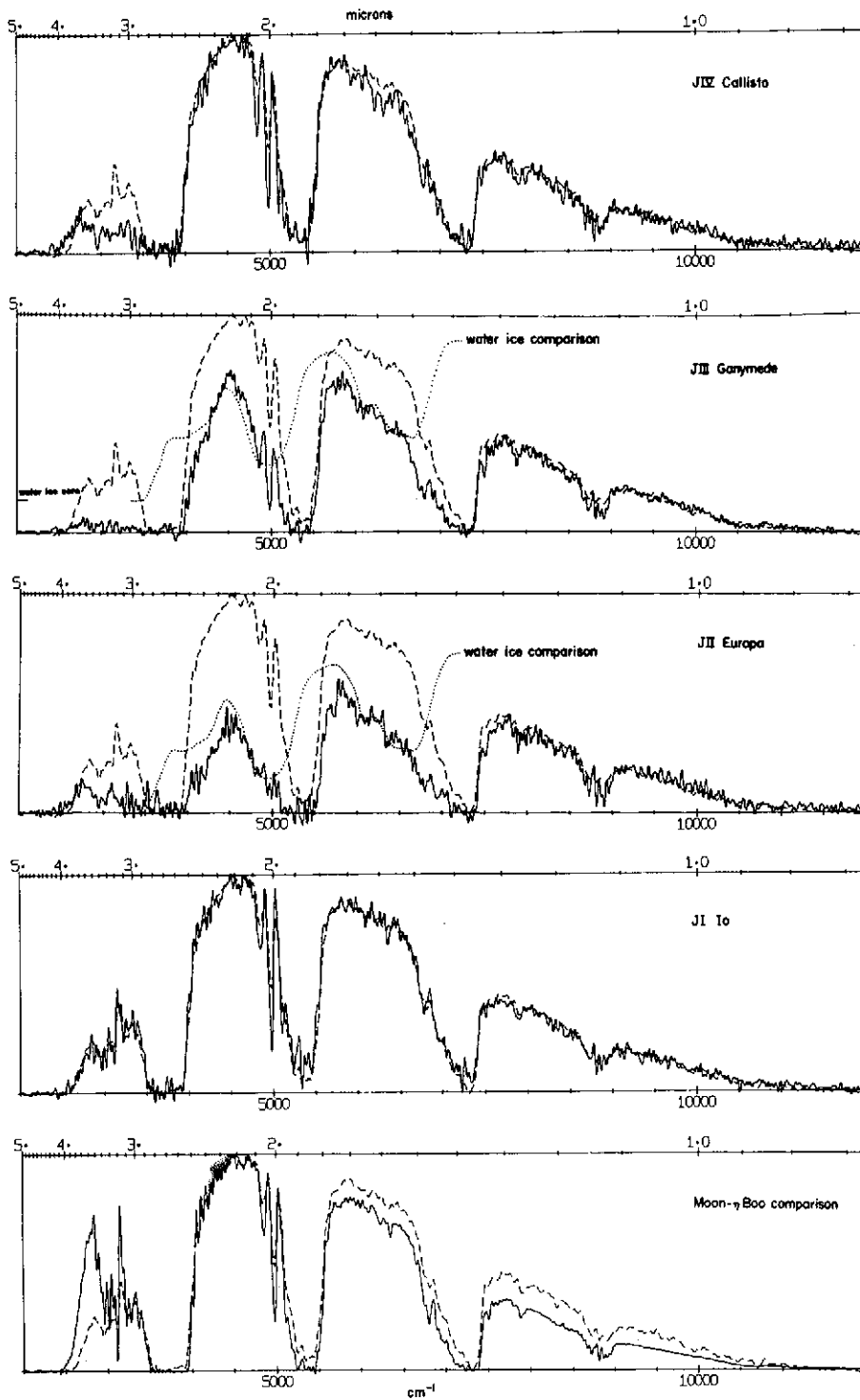
Figure 1   Spectra of 4 Galilean satellites with resolution of 25 cm^{-1} and average telluric air mass of 1.9. Moon comparison (air mass 1.94) is shown for narrow features. A solar-type star (ηBoo, air mass 1.13) is shown as dashed line for general albedo characteristics. A laboratory water-frost reflection spectrum is superimposed on spectra of JII and JIII as dotted line

wavelengths (Moroz 1965, Condron *et al.* 1966). Nevertheless, it is useful as a comparison for any narrow-absorption features which may occur in the satellite spectra since a signal-to-noise ratio in excess of 1000 was obtained in a few minutes at the telescope. At the bottom of Figure 1 we show the two comparisons used in our analysis, the Moon and ηBoo, a GO-type star, close to the Sun in spectral type. The extra thermal emission of the Moon past 3.2μ as well as the decreasing albedo below 1.8μ can be seen clearly.

When the spectrum of ηBoo is compared with the spectra of the satellites, it is found that Io follows a solar spectrum curve quite closely. The spectrum shows no absorptions that could be attributed to Io, and remarkably the albedo is perfectly flat to within its noise level of a few percent. While there are a number of compounds which show no absorptions from 1-4μ (all the IR transmitting window materials for example, sulfur powder, KBr powder, etc.), we feel that more likely Io's flat albedo is due to surface dust of such a particle size which masks the absorption features.

The spectra of Europa and Ganymede show deep absorptions in the 3-4μ window, the 1.9-2.7μ window, and the 1.4-1.8μ window. A comparison with laboratory studies of NH_3, CH_4, CO_2 and H_2O ices showed that only H_2O ice gives a good fit. An H_2O ice reflection spectrum is shown as a dotted curve on the spectra of Europa and Ganymede. Water ice has its strongest feature at 3200 cm^{-1} due to the fundamental OH stretch frequency. It also has a shoulder at 4000 cm^{-1}, an absorption at 4950 cm^{-1} and an absorption between 5700 and 7000 cm^{-1}, with a broad peak at 6500 and a sharp peak at 6080 cm^{-1}. While the earlier spectroscopic investigation of the satellites as well as broad-band photometry (Lee 1972) showed only a deficiency of light in the above-mentioned windows, our spectra show that Ganymede and Europa follow the water-ice features with remarkable fidelity. The sharp and broad feature at 6080 and 6500 cm^{-1} show up well above the noise level. These features show even more clearly on a ratio spectrum. There can therefore be no doubt that water ice is present in large amounts on the surface of Europa and Ganymede.

Strangely, the spectrum of Callisto with its low density shows very little evidence of surface ice. There is some absorption between 3 and 4μ, and slight deficiencies at the other ice absorptions. The comparison star ηBoo does not fit quite as well as in the case of Io. We conclude that Callisto is covered mostly with some type of dust but with a small amount of water ice showing through. The two absorptions near 1.6μ which show up somewhat prominently on the spectrum of Callisto are most likely telluric CO_2 (cf. Moon). The absorptions appear somewhat larger than the telluric contribution but fall within the noise level. Of course, the possibility of solid CO_2 which does have two absorptions there (Larson and Fink 1971) cannot be completely excluded.

It is difficult to infer from our data alone whether the ice absorptions are due to localized areas of ice coverings, such as polar caps, for example, or whether they are due to a fairly uniform snow over the whole surface. The almost total absorption between 3μ and 4μ on Ganymede would indicate that snow is distributed over the whole satellite, otherwise the fraction of the satellite uncovered would reflect light in that region (assuming that the surface rock material reflects light in that region, which it will if Ganymede has a similar basic composition as Io). This does not mean that polar caps with large ice concentrations do not exist, but rather that a thin frost layer must also be present over most of

the rest of the satellite surface. In fact, polar caps have been seen visually on all satellites except Io (Antoniadi, Lyot, Camichel, Gentili 1959), and would be expected on simple grounds of temperature distribution over the satellites. Our data also show possible variation of the reflection characteristics with orbital phase. In the present paper, for the sake of the best S/N ratio we, of course, present averages. The variation of albedo with orbit and the spatial distribution of the ice covering requires a more extensive analysis of partial, noisier sums of spectra which we are deferring until later.

In 1944, Kuiper discovered an atmosphere of methane on Titan and set upper limits of 200 cm-atm of CH_4 and 40 cm-atm of NH_3 for the Galilean satellites. In order of atmospheric retention ability, the large satellites of Jupiter rank right after Mars and Titan and before Mercury and the Moon. Therefore, a thin atmosphere of methane or ammonia could still be expected on these satellites. Our spectra provide a more sensitive test for these gases since their strong absorption bands lie in the infrared. For methane the most suitable region is near 2.30μ where three strong methane bands lie, the $\nu_2 + \nu_3$, the $\nu_3 + \nu_4$, and the $\nu_1 + \nu_4$ bands. The portion of the telluric absorption caused by these bands is shown as a dotted area on the Moon spectrum in Figure 1. The amount of methane causing this absorption is 1.50 cm-atm (STP). The spectrum of ammonia has its strongest band in our spectral region very close to the methane band, at 2.25μ, mostly due to the $\nu_2 + \nu_3$ transition. Its proximity to the methane band, its similar strength (about a factor of two stronger) and the close molecular weights of NH_3 and CH_4, means that an analysis for an upper limit will give roughly the same answer for each gas. Also, the similar S/N ratios of the four satellites means that the analysis described below will hold for all four of them.

We estimate that if half the absorption shown by the dotted area on Figure 1 were present for the Galilean satellites, it would be discernible in the spectra. While individual gaseous lines are, of course, not resolved with our 25 cm^{-1} resolution limit, the telluric methane absorption does show up as a series of relatively sharp features (see Moon spectrum on Fig. 1), while the ice absorptions are only slowly varying with wavelength. Any gaseous absorptions would therefore be visible as features superimposed on the smooth reflection spectrum of the surface material, so that the ice absorptions on JII and JIII do not interfere with any atmospheric upper limits. In order to interpret this absorption in terms of an upper limit for a satellite atmosphere, we made use of a high-resolution solar spectrum (0.15 cm^{-1}) as an intermediate step. The high-resolution spectrum, recorded by us on Kitt Peak with the "Connes" interferometer, shows all the individual methane lines resolved. Except for a few of the strongest ones, we found these lines to lie on the linear portion of a Lorentz curve of growth. A line of average strength had an equivalent width of about 0.030 cm^{-1}, which gives 0.015 cm^{-1} for our satellite detection limit discussed above. Using a Doppler half width of 0.0055 cm^{-1} appropriate for CH_4 at T = 140°K, we found that such an average line would be saturated by a factor of 3 on a Doppler curve of growth. For a planetary hemisphere reflecting like a Lambert surface with no limb darkening, the average air-mass factor is 4. This case should be applicable for the Galilean satellites. These arguments define a new upper limit of 0.5 cm-atm (STP) for both CH_4 and NH_3 on the four Galilean satellites. It is, of course, in the nature of the Doppler curve of growth that if our detection limit, which we set for an average line, were increased by a factor of 2 or 3, the saturation factor

can quickly become much larger. At this point, however, many weak lines would start to contribute significantly to the absorption so that the equivalent width of an average line would still be close to the linear portion of the curve of growth, and this in turn would increase the absorption above our observed detection limit.

The precision of the data and the type of analysis used should produce an upper limit reliable to about a factor of 2. Using the acceleration of surface gravity on the satellites, we can convert our abundance into a partial pressure for each gas, and obtain 6×10^{-8} atm. At these pressures Lorentz broadening will be completely negligible. This pressure is in good agreement with and even somewhat lower than the upper limit of 2×10^{-7} atm derived from the β Scorpii occultation by Io (Bartholdi and Owen 1972).

It has been realized for quite some time that the low densities of the Galilean satellites, particularly the outer two, cannot be explained by a purely silicate-rock composition alone. Some fraction of low density ices seems to be required. Also, the radioactive heating and melting of any ice have very likely driven it to the surface. In the case of Europa and Ganymede we do indeed see such a surface ice covering. Europa shows the deepest ice absorptions and the lowest temperature (~121°K, Armstrong 1971). This would indicate that the presently accepted albedo of 0.49 (Harris 1961) is probably somewhat too low. Curiously enough, Callisto with the lowest density shows very little surface ice. We conclude that the surface which we observe is covered with a dust layer which hides the underlying ice from direct view. In agreement with this, Callisto has the lowest albedo of the four satellites (0.15, Harris 1961) and the highest measured temperature (156°K, Armstrong 1971). On the other hand, the higher density of Io, even with the new value for the radius from the β Scorpii occultation (Hubbard and Van Flandern 1972), makes us believe that the absence of observable water ice on its surface is due to a depletion of ice for that satellite. No polar caps have ever been seen on Io, but instead, the polar areas have been observed to be darker than the central portion. Although the evolutionary history of the four Galilean satellites is still far from clear, the conclusions drawn from our new spectroscopic data should at least reduce the number of plausible hypotheses.

REFERENCES

Antoniadi, E. M., Lyot, B., Camichel, H., and Gentili, M. 1959, LAROUSSE ENCYCLO-PEDIA OF ASTRONOMY, Prometheus Press (New York), pp. 216-217.
Armstrong, K. R. 1971, Thesis on "Infrared Photometry and Radiometry of the Planets", Rice University, May 1971.
Bartholdi, P. and Owen, F. 1972, *A. J., 77*, 60-65.
Condron, T., Lovett, J., Barnes, W., Marcotte, L., Nadile, R. 1966, "Gemini 7 Lunar Measurements",Rept. 8, AFCRL, Bedford, Mass., 49 p.

Gromova, L. V., Moroz, V. I., Cruikshank, D. P. 1970, Astronomicheskii Tsirkular No. 569, Bureau of Astronomical Communications of the Academy of Science, USSR (in Russian).

Harris, D. L. 1961, in PLANETS AND SATELLITES, Ed. G. P. Kuiper and B. M. Middle-hurst (Chicago: University of Chicago Press), pp. 272-342.

Hubbard, W. H. and Van Flandern, T. C. 1972, *A. J.*, *77*, 65-74.

Kuiper, G. P. 1944, *Ap. J.*, *100*, 378.

Kuiper, G. P. 1952, in THE ATMOSPHERES OF THE EARTH AND THE PLANETS, Ed. G. P. Kuiper (Chicago: University of Chicago Press), pp. 306-405.

Kuiper, G. P. 1957, *A. J.*, *62*, 245.

Kuiper, G. P., Cruikshank, D. P., Fink, U. 1970, *Sky and Telescope*, *39*, 14.

Kuiper, G. P. 1971, 18th and 19th Semiannual Status Report to the National Aero-nautics and Space Administration, Feb. 11, 1971, by the Lunar and Planetary Laboratory, University of Arizona (unpubl.); *LPL Communication No. 187.*

Larson, H. P. and Fink, U. 1972, *Ap. J.*, *171*, L91-L95.

Lee, T. A. 1972, *LPL Communication No. 168.*

Moroz, V. I. 1966, Soviet *A. J.*, *9*, 999-1006.

NO. 187   COMMENTS ON THE GALILEAN SATELLITES

by Gerard P. Kuiper

September 12,1973

ABSTRACT

The surface deposits of the Galilean satellites, especially Io, are examined in the light of some early and some very recent observations. Io, with probably a thin sulfur deposit in the lower latitudes and orange polar caps presumably composed of sulfur compounds, stands apart from the other three satellites.

1.   Early Color and Spectral Observations

The unusually orange color of JI, Io, was discovered by Hertzsprung in 1911. It has been a challenge to determine its physical meaning. The author, in collaboration with the late Dr. D. L. Harris, made a number of observations of Io and the other three large satellites in the 1950's with the 82-inch telescope of the McDonald Observatory. The photometric, colorimetric, and eclipse

data were published in Harris' excellent chapter in Volume III of THE SOLAR
SYSTEM series (Kuiper and Middlehurst, 1961). Attention is called to the Io
color curve between 0.35 and 0.80μ by Harris (op. cit. p. 304), showing the
exceptional properties of Io, approximated only by the satellite Titan of Saturn,
which, however, differed in the red and near-IR owing to its CH_4 absorptions.

The writer endeavored to extend our knowledge of the Jovian satellites beyond
1μ, both by photometry and by low-resolution spectroscopy. Both were carried out
with the 82-inch telescope in 1956. My photometry was quoted by Harris in his
Table 19 (op. cit. p. 305) which is repeated for ready reference in Table I. It
was clear from this photometry that Io and Callisto had roughly constant albedos
from 1-2μ, but that Europa and Ganymede were deficient at the longer wavelengths.

TABLE I

INFRARED OBSERVATIONS OF PLANETS AND SATELLITES

Planet or Satellite	$I(2μ)/I(1μ)$	Planet or Satellite	$I(2μ)/I(1μ)$
Sun	1.00	Mars	1.00
Venus	1.61	Io	1.06
Saturn	0.47	Europa	0.66:
Saturn's Ring	0.45	Ganymede	0.63
Jupiter	0.21	Callisto	0.95
Uranus	0.06:	Titan	0.20:
Mercury	3.5		

This was shown independently in my low-resolution spectra obtained between 0.8μ
and 2.5μ. The resolution in these spectra was just sufficient to show the 1.6μ
and 2.2μ transmission peaks, well offset by the strong H_2O absorptions at 1.4 and
1.9μ. The quantities so derivable were the intensity ratios 0.8/1.6/2.2μ. Figure
1 reproduces some traces of the four Jovian satellites so obtained as well as of
the Ring of Saturn. Solar-type stars were used as comparisons, among them ηBoo,
which showed spectra almost identical to those of JI. It followed that the 1.6
and 2.2μ maxima were deficient in intensity in both JII and JIII, but not in JI
and JIV. The deficiencies were very marked in the Saturn Ring. The ratios 1.6/
0.8μ were found as follows:

Sun	0.55	JIII	0.31
JI	0.53	JIV	0.54
JII	0.27	S.Ring	0.23

On the basis of these results I stated (1957): "The spectrometer tracings show
striking differences between the four Galilean satellites of Jupiter. I and IV
roughly resemble the solar and lunar curves between 1 and 2.5μ, but III and par-
ticularly II are markedly different, in the sense that the spectrum beyond 1.5
is reduced in intensity by a factor of 2-3. This is most readily explained by
assuming that II and III are covered by H_2O snow. The albedo and color of II in
visual light are compatible with this hypothesis, while III, which is darker, may
be covered with snow contaminated with silicate dust. The rate of evaporation of
snow, even if exposed to a vacuum, is shown not to be excessive at the distance
of Jupiter. Good records of Saturn rings confirm the earlier result that they
are composed of snow".
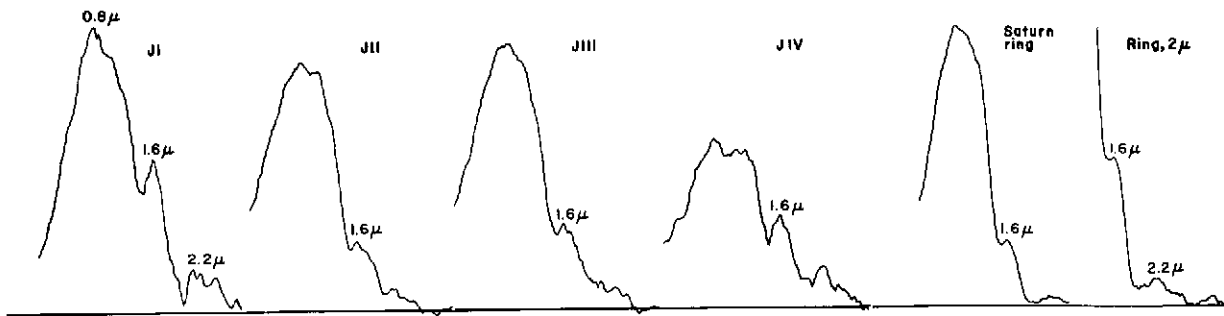
GERARD P. KUIPER

Figure 1   Spectrometer traces of Galilean satellites and Ring of Saturn,
82-inch telescope (1956)

The sensitivity of the PbS cells has not markedly increased during the
past two decades and no substantially higher-resolution spectra could be acquired
until the development of Fourier spectroscopy. A determined effort was made to
obtain such spectra for the Jovian satellites with the 61-inch telescope in 1970,
jointly with Drs. U. Fink and H. Larson. The following quotation is taken from
my 1970 report to NASA covering work done under Research Grant NGL-03-002-002:
"... preliminary results on the Jupiter satellites. The latter are rather faint
for a 60-inch aperture, so that we had to reduce the spectral resolution. The
interferometer sweeps are 2 secs. for full resolution but 1/2 sec. for the reso-
lution on the satellites. We got 8-3/4 hrs. of integration time on Ganymede,
over three nights; 5-1/4 hrs. on Io, 4 hrs. on Callisto, and 3 hrs. on Europa;
thereupon the tens of thousands of interferograms were co-added and reduced. In
spite of the considerable time spent in the reductions we have concluded that the
results are still provisional and must be strengthened by further observation,
scheduled to begin early 1971. To illustrate the records so far obtained, we are
reproducing in Figs. (2) and (3) the spectra of all four satellites compared to
the moon, plotted with two resolutions, 80 and 200 cm^{-1}. The ordinates were ad-
justed to the moon around 8000 cm^{-1} (7500-8800 cm^{-1}, or 1.14-1.33µ); no important
absorptions are expected there. These satellite spectra are provisional, and we
have omitted the parts below 3000 cm^{-1} (λ > 3.33µ), where there is evidence of
some uncompensated sky radiation in the results". (The numbers of the Figures in
parentheses have been changed to correspond to the numbers used here).

Figures 2 and 3, due to the joint efforts by Drs. U. Fink, H. Larson, and the
writer, are unaltered copies of the NASA 1970 report (dated February 4, 1971).
These results were challenging but, as stated, still considered of insufficient
quality for final publication; in particular, the reality of the features in the
Callisto spectrum near 6300 and 4700 cm^{-1} was considered in question. The ice
absorptions on Europa and Ganymede, announced in 1957, were plainly shown and
clearly real. The recent spectra in *LPL Communication No. 186* have justified our
reluctance to accept the reality of the Callisto absorptions. The earlier spectra
are reproduced here for their historical interest, in part because of the quite
large effort expended both at the telescope and in the reductions. The superior-
ity of the new spectra is due to extensive work by Drs. Dekkers and Fink on the
interferometer itself, which increased its signal-to-noise ratio by a factor of
about 4, corresponding to a gain of 16 in observing time.

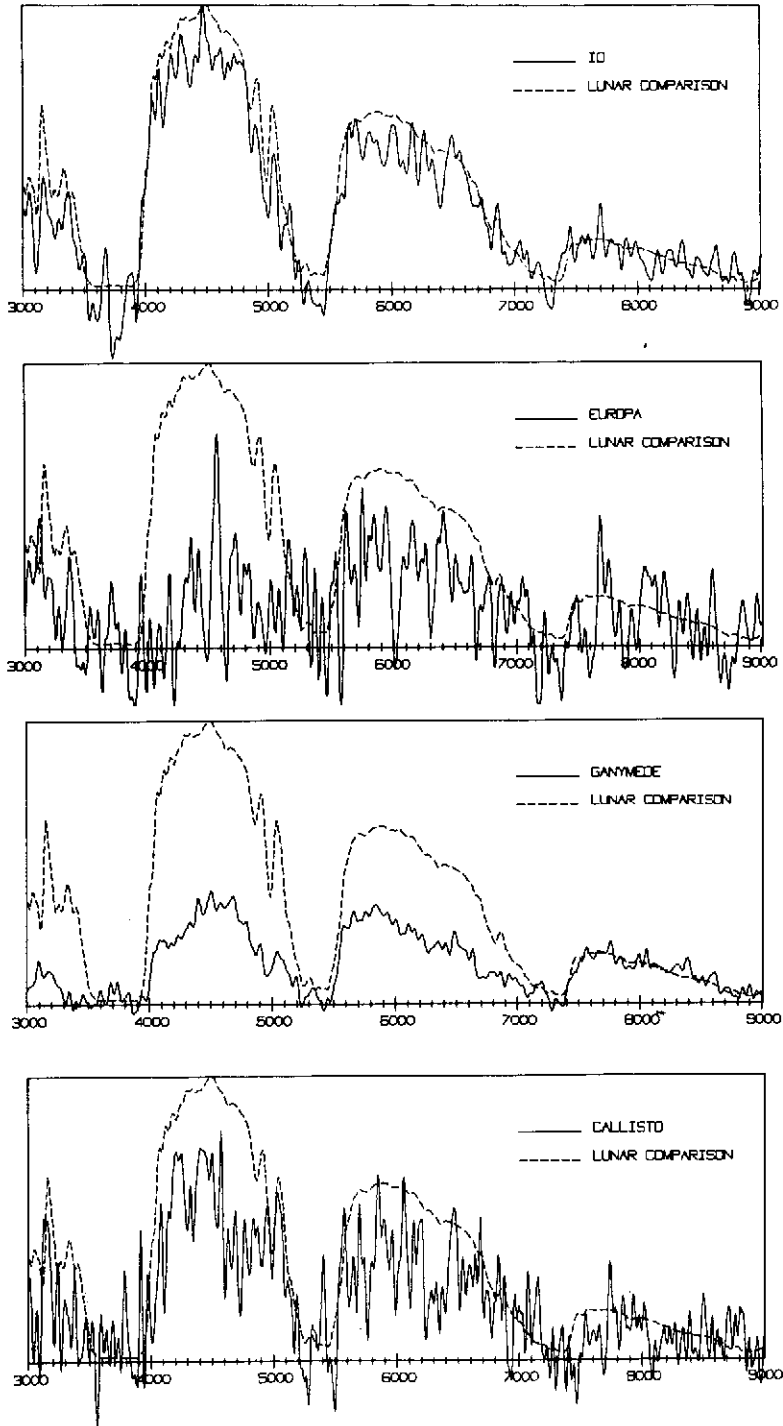Figure 2 Jupiter Satellites, spectral resolution
80 cm^{-1}, 3.3-1.1μ (scale in wave numbers).
(Provisional)

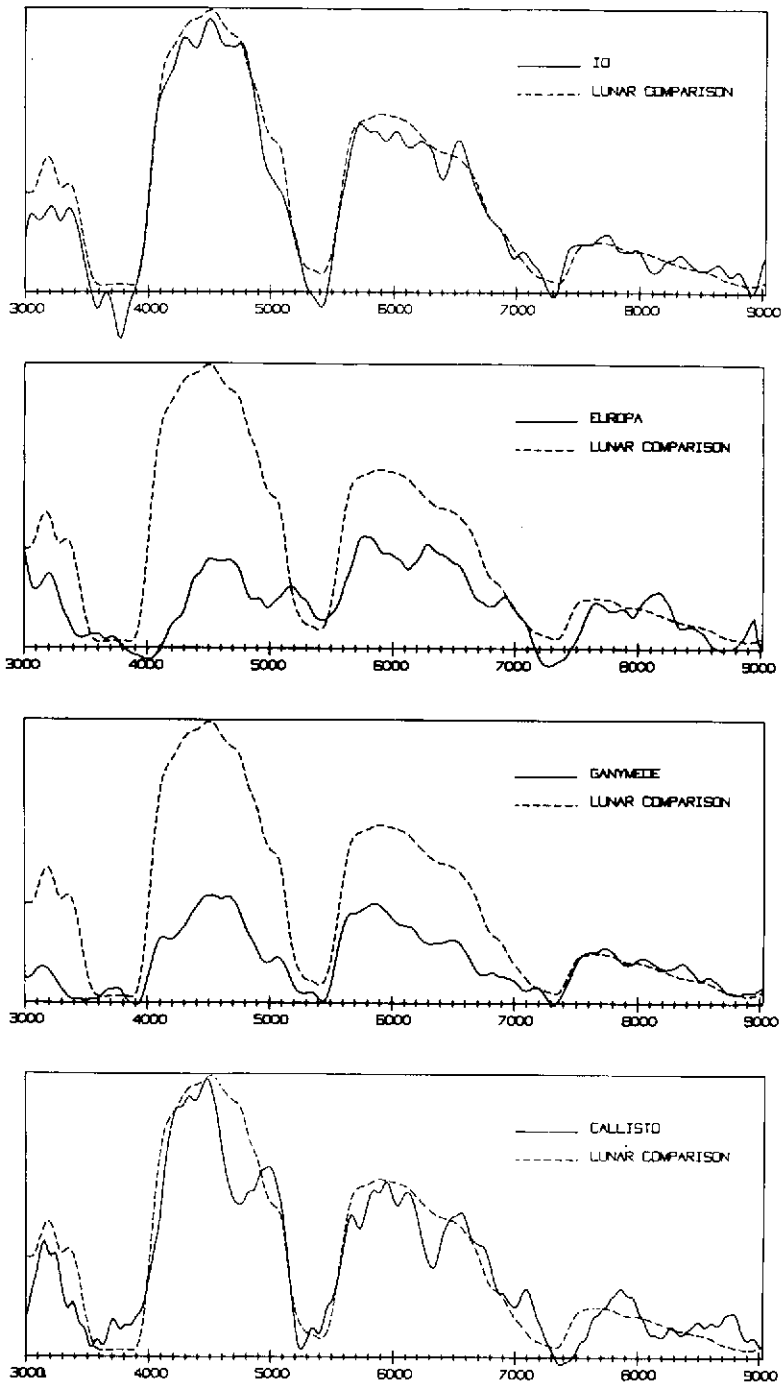GERARD P. KUIPER

Figure 3 Jupiter Satellites, spectral resolution
200 cm^{-1}, 3.3-1.1μ (scale in wave numbers).
(Provisional)

The albedo curve obtained by Wamsteker for the shorter wavelengths, 0.3-1.1μ
(*LPL Comm. No. 167*), is compatible with the reflection curve of *sulfur*, as pointed
out in Wamsteker's paper. So is the high and uniform albedo from 1-4μ. The ob-
servations at 3.5μ and 5μ by Gillett *et al.* (1970) are also consistent with Io
being covered by sulfur. *No other substance has been found that explains the
entire range, 0.3-5μ, so well.* For laboratory comparisons reference is made to
LPL Communication No. 184 by Fr. Sill and *No. 185* by Fink and Burk. The *only
deviation from the smooth sulfur reflection curve occurs around 0.56μ*, where a
10%-deep absorption feature is noted extending from 0.50-0.62μ. Wamsteker called
attention to the proximity of this feature to a band by $NH_4 \cdot HS$ at 0.65μ, seen in
the laboratory curves of Fr. Sill's publication. However, the systematic drop,
longward of 1μ and the narrower strong absorptions near 2μ, both absent from Io,
cast doubt on a substantial admixture of $NH_4 \cdot HS$.

2. Other Observations

In the following *Communication* the discovery of the russet color of the dark-
ish polar caps of Io is announced by R. B. Minton. The polar-cap colors appear to
be close to that of the Jupiter Red Spot, which we have tentatively attributed
to ammonium polysulfides. We are awaiting spectra of the Red Spot 0.3-4μ before
this matter can be resolved. Still, the integrated spectrum of Io does not appear
to contain an appreciable admixture of the type of spectrum that Fr. Sill found for
ammonium polysulfides in the laboratory. Even the Io band at 0.56μ does not agree
well with the laboratory absorption at 0.65μ.

Binder and Cruikshank (1964) discovered a brightening of Io immediately fol-
lowing a total eclipse by the planet. The observations were made in blue light
(λ4500Å) and the most natural explanation would appear to be that *the sulfur
deposit on the satellite became white at the very low temperatures during the
eclipse,* 90°-100°K (Morrison and Cruikshank 1973). If this hypothesis is correct,
the post-eclipse effect should be nearly absent in red light, and be maximum
around 4000Å. Actually, T. Johnson (1971) finds the effect on Io larger at λ4350
than at λ5600Å; but more data, including at 0.40μ, are needed before a clear answer
is at hand.

Morrison and Cruikshank (1973, p. 232) conclude from their eclipse observa-
tions at 20μ that Io and the other satellites have a low-density surface layer
only a few mm thick of very low conductivity, below which lies a layer of much
greater conductivity. They assume the upper layer of all four satellites to be
ice mixed to varying degrees with *rock powder*. We believe a thin *S* deposit to be
better in accord with the spectral data. It could be due to H_2S exhalations, with
the solar UV decomposing the gas and causing a deposit of S, with H escaping. If
the Red Spot is indeed found to be $NH_4 \cdot xS$, this may be the composition of the Io
polar cap deposits as well. Fr. Sill points out that such a deposit could be due
to occasional NH_3 exhalations causing NH_3 *ice* deposits on the *cold poles*; with H_2S
exhalations causing the NH_3 ice to form $NH_4 \cdot HS$; which would turn to the polysulfide
by the solar UV radiations, much as supposedly occurs in the Jupiter Red Spot and
other russet-colored Jupiter clouds. The polar caps are then due in the first
place to the low vapor pressure of NH_3 being able to deposit its ice only under
temperatures lower than about 100°K. The equatorial NH_3 would decompose and
escape; the equatorial H_2S cause the sulfur coating. I am indebted to Fr. Sill
for a clarifying discussion on the subject of this paragraph. A preliminary
announcement on the Io polar caps is found in *Sky and Telescope*, October 1973,
p. 228.

    Hansen (1973) similarly concludes that JI, JII, JIII require a two-layer
model to satisfy his 1971 eclipse observations made at 8-14μ. He stresses,
however, that a difference is indicated for the thin upper layers of JI, as
compared to the other two satellites, in the sense of a lower conductivity
for Io. A composition difference is certainly indicated by the spectra.

REFERENCES

Binder, A. and Cruikshank, D. F. 1964, *Icarus*, *3*, No. 4.

Gillett, F. C., Merrill, K. M., Stein, W. A. 1970, *Astrophys. Letters*, *Vol. 6*,
   247-249.

Hansen, O. L. 1973, *Icarus*, *18*, 237-246.

Kuiper, G. P. 1957, *Astron. J.*, *62*, 245.

Kuiper, G. P. and Middlehurst, B. M. 1961, THE SOLAR SYSTEM, Vol. III, 272-342.

Morrison, D. and Cruikshank, D. P. 1973, *Icarus*, *18*, 224-236.

NO. 188   THE RED POLAR CAPS OF IO

by R. B. Minton

October 1, 1973

ABSTRACT

An excellent series of Jupiter photographs obtained on August 9, 1973 showed Io to have red-brown polar caps, with the South Cap substantially larger than the North Cap. Reproductions are shown in the color Plate. The polar caps stand out by the color contrast against a white-bluish zone of Jupiter. When projected against a brown belt, only the truncated brighter equatorial region of the satellite is seen. Some 1968 images of Io also show the color of the polar caps directly.

Jupiter has been routinely photographed by the Lunar and Planetary Labora-
tory since October 1965 to the present. During this interval, the four Galilean
satellites are frequently recorded in transit across Jupiter's disk. Io is most

often recorded due to its proximity to Jupiter. Since 1972, as an aid to more
accurate longitude measures of Jupiter's clouds, Io has been routinely photo-
graphed at Inferior Geocentric Conjunction (IGC). The planet's geometrical
phase defect is exaggerated on photographs, e.g. in the UV, by less-than-normal
limb brightening at the terminator and more-than-normal at the opposite limb.
With Io measured relative to the East and West limbs at IGC, the linear dis-
placement from the measured center can be converted to a correction, applied in
calculating the longitudes of clouds.

There are quite a few images of Jupiter in the LPL collection which show
a non-uniform disk of Io. The best of these are reproduced in Plate I and Figures
1-7. Only images with Io in transit reveal surface markings provided the seeing
is excellent and the background uniform. Photographed against a dark sky, Io's
markings are not recorded with our cameras - just the yellow color of the satellite
as a whole. Prior to August 1973, our color photographs had suggested that the
polar regions of Io were simply dark. Both caps blend in well with the generally
warm yellow, brown, and red tones of Jupiter's clouds. The caps are recorded as
dark in all wavelengths used in our black-and-white photography. The equatorial
region is recorded as yellow on color films and as very bright in the photographic
infrared. In UV and blue light, the satellite as a whole is dark; but the slight
non-circularity of these images suggests the equatorial region is still slightly
brighter than the polar caps.

A combination of fortunate circumstances occurred on August 9, 1973,
whereby the polar caps were recorded and are easily discernible as being red in
color. The seeing was excellent; Io was well placed from the CM and limb; and
the background of Jupiter was bluish-white. IGC occurred at 0605 UT, with Io
appearing as an orange, ill-defined spot. Some 35 minutes later the background
of Jupiter was reduced to more nearly that of Io. At these times (2 per transit)
adjacency effects in the photographic image of Io are minimal. From 0640 to 0641
UT, 27 images of Jupiter were taken of which all but two or three, of poorer
quality, easily show the dark, red polar caps and the yellow equatorial region.
The best images are reproduced in color in Plate I. The 1968 and 1973 color
images show the South Polar Cap to be larger than the North. Of our five superior-
quality color rolls, three show a variable width (in longitude) of the equatorial
region. It appears to be widest near about 200° of Io longitude, becoming nar-
rower near the West and East limbs. The infrared photographs of Io show the
equatorial region as very bright, narrow, and to have an essentially constant
width in longitude (see Figs. 3, 5, 6). Figure 8 is my interpretation of LPL
color and infrared photographs of Io.

<div align="center">Legends for Plate I on next page</div>

a. 1968 Jan 25 08:28:16 UT   b. 1968 Jan 25 08:28:58 UT
    High Speed Ektachrome   High Speed Ektachrome

c. 1968 Feb 17 08:06:41 UT   d. 1973 Aug 9 06:40:19 UT
    High Speed Ektachrome   Ektachrome (comp. of 4)

e. 1973 Aug 9 06:40:52 UT   f. 1973 Aug 9 06:56:10 UT
    Ektachrome (comp. of 2)   Ektachrome (comp. of 8)

37
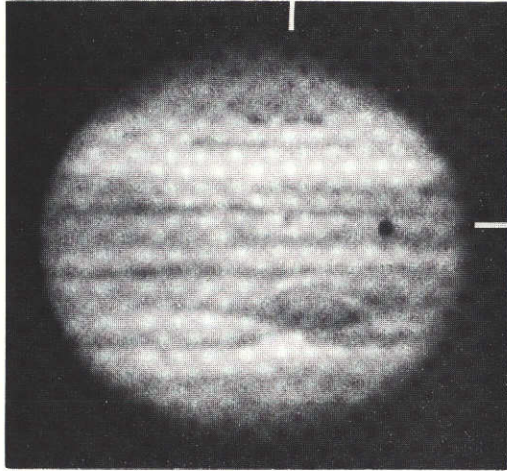
Fig. 1 1968 Jan 25 0925 UT,blue fr.color
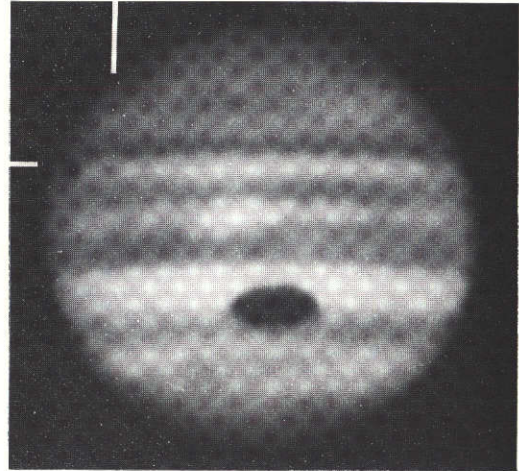
Fig.2 1971 Jun 1 0603 UT,blue fr.color
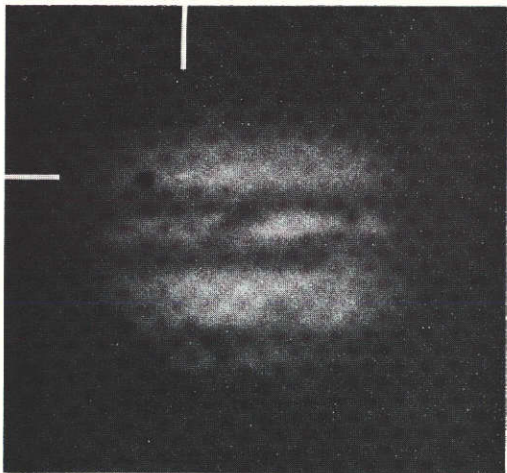
Figure 3 1971 Jun 1 0628 UT, IR
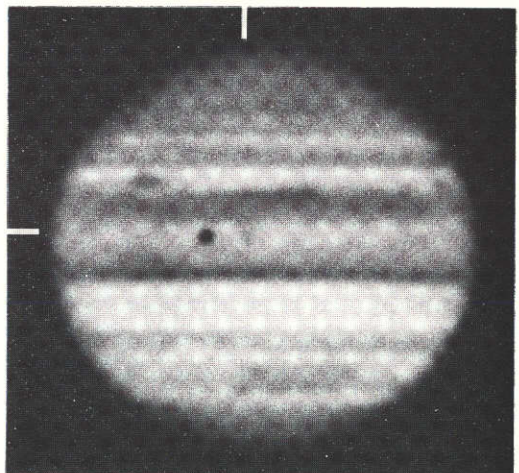
Figure 4 1973 Aug 9 0559 UT, blue
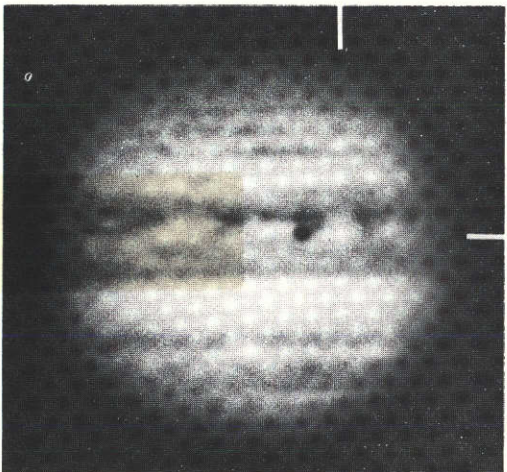
Figure 5 1973 Aug 9 0634 UT, IR
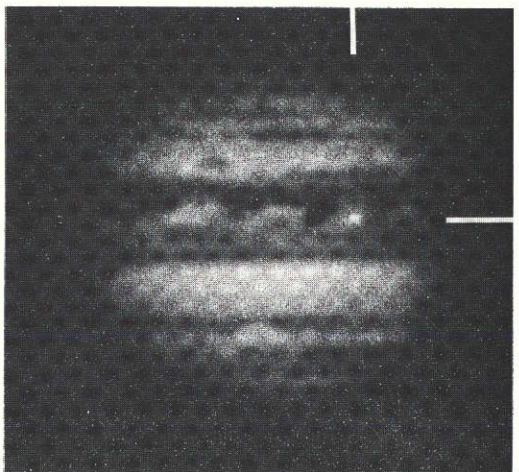
Figure 6 1973 Aug 9 0634 UT, IR

37-A
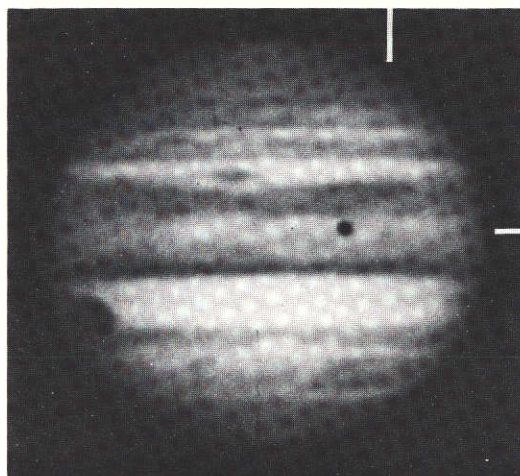
Figure 7   1973 Aug 9 0641 UT,
blue from color
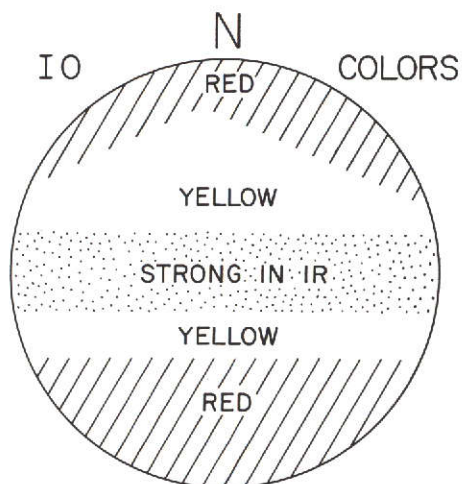
Figure 8   Regions of maximum re-
flectance at wavelengths indicated

The CM of Io was calculated from the following formula:

$$\text{CM Io} = 180° + i + 0°.14\ t$$

where i is phase angle of Jupiter, + before opposition, - after; and t is minutes
before (-) or after (+) IGC. These Central Meridians are listed in Table I.

TABLE I

	Date	UT	IGC	Δt	i	CM Io
68	Jan 25	0828	0919	-51^m	$+5°.3$	178°
	Jan 25	0829	0919	-50	+5.3	178°
	Jan 25	0925	0919	+ 6	+5.3	186°
68	Feb 17	0807	0856	-49	+1.0	174°
71	Jun 1	0603	0651	-48	-2.0	171°
	Jun 1	0628	0651	-23	-2.0	175°
73	Aug 9	0559	0605	- 6	-2.0	177°
	Aug 9	0634	0605	+29	-2.0	182°
	Aug 9	0641	0605	+36	-2.0	183°

The times at which Io most nearly matches the background in intensity at
visual wavelengths varies with its CM distance on Jupiter and the intensity of
the background. Presently these times are 30 to 40 minutes before and after
IGC. Much of Jupiter's Equatorial Zone is presently whiter than in 1972.
The red caps are also readily apparent with Io seen in projection against a
normally white zone such as the NTrZ (see Fig. 2).

It appears that an ideal instrument for further investigation would be an area scanning photometer or spectrophotometer with a slit no wider than 1/5 arc sec in width. Here, however, the satellite may be more easily studied against a dark sky. Photographic studies appear to be more fruitful with Io in transit. Because of the proximity of Io to Jupiter and the near 12° maximum phase angle of Jupiter, Io can be seen through a total of about 44° of orbital longitude during an apparition and still be seen in transit.

NO. 189 COLOR PHOTOGRAPHY OF JUPITER

by S. M. Larson, J. W. Fountain, R. B. Minton

September 1973

ABSTRACT

Selected color photographs of Jupiter taken with the 154-cm
Catalina reflector from October 1965 to September 1973 are pre-
sented. Eight oppositions are covered showing the developments
in cloud belt structure and color distribution of the Jovian
atmosphere.

Jupiter photography with color emulsions has been carried out regularly
along with black-and-white filter photography in the continuing program of
planetary photography with the NASA 154-cm reflector of the Catalina Observatory
(Fountain and Larson 1973). The time coverage over eight oppositions provides a
good base for study of the evolution of the cloud masses and their colors.

Although filter photography with black-and-white emulsions usually yields
somewhat higher resolution (and is easier to calibrate photometrically), the
color film offers several advantages. Its simultaneous recording in the three

40

broad wavelength bands produces an image with higher information content than a single black-and-white image can give. On a color photograph one can see more easily the precise spatial relationships between features of slightly different colors. This speeds up the identification of features shown on the black-and-white photographs. Although the effective bandpass and sensitivity of each emulsion layer in color film is difficult to determine precisely (and may vary from batch to batch), the great majority of the features recorded on Jupiter do not exhibit great changes in reflectivity over small wavelength intervals so that it is possible to correct for emulsion differences in succeeding copies and reconstruct the visual impression closely. The most obvious departure is that the color images reproduce the colors with higher contrast than that noted in the telescopic image. Virtually all reproduced photographs of Jupiter are subject to this, which in many cases is desirable since it produces greater visibility of features. A correlation may exist between color and composition or particle size, so that color photography may provide a convenient source of spatial distribution studies.

In the present program, Kodak Ektachrome-EF reversal film is most commonly used. Many color emulsions have been tried, and in the first few years, Kodak High Speed Ektachrome was used most often. It was found that the color fidelity in Ektachrome-EF was more consistent. Atmospheric dispersion was compensated for by the use of a non-deviating small-dispersion prism in the telescope beam.

Most of the processing was done by Kodak Laboratories since they provide more consistent results than local processing firms. In some cases, we found that an increase in resolution was obtained by reducing the exposure by as much as a factor of 4 and extending in our darkroom the development time of the first developer. The increase in contrast makes copying more difficult and the color balance may be affected so that normally processed film, even at reduced resolution, is always needed for verification.

The plates reproduced here were made by copying the original images on Kodak Ektachrome-X, normalizing density and color with a standard whose color accuracy was verified at the telescope. The plates are reproduced with North up.

<div align="center">REFERENCE</div>

Fountain, J.W. and Larson, S.M. 1973, "Multicolor Photography of Jupiter", *LPL Communication No. 175, 9.*

Editorial Note: The Laboratory intends to publish a 6-8 fold more extensive series of color photographs of the planet for the past eight oppositions, accompanied by a descriptive text.

LEGENDS FOR COLOR PLATES OF JUPITER

1. October 30, 1965; 8:21:58 UT. Red Spot (RS) prominent. Its Hollow seen by virtue of well-defined grey south component of the South Equatorial Belt (SEBs). White Equatorial Zone (EZ) is wide, with blue-festoon activity apparently originating in the North Equatorial Belt (NEB). The North Temperate Belt (NTeB) is faint, but distinctly orange.

2. January 10, 1966; 5:41:07 UT. RS has dark border. SEBs is deflected north by RS Hollow. Material appears to return to SEBs latitude in the disturbed area following RS. Dark spot is shadow of satellite Io.

3. January 20, 1967; 5:58:31 UT. Many high-latitude light and dark spots in the South Temperate Belt (STeB) region are seen as well as much detail in the SEBs. The grey NTB appears wedge-shaped and in some parts double. Note elongated grey spot near central meridian in NTeZ.

4. March 17, 1967; 3:43:43 UT. Rift in NTB. Large white spot in brown NEB.

5. April 16, 1968; 4:56:15 UT. Single blue festoon still prominent in NEB.

6. May 9, 1968; 3:47:19 UT. Large blue festoon; part of NEB also blue. STB nearly absent at these longitudes.

7. April 5, 1969; 6:12:59 UT. The SEBs had brightened. SEBn is a well-defined grey belt bordering the yellow EZ which itself is filled with many festoons. The STrZ is slightly bluish, and the region around the STZ has much spot activity. NTB is very weak.

8. May 30, 1969; 4:05:38 UT. High-latitude spots shown in and S of STrZ. Note bright spot near central meridian on north edge of NEB.

9. May 16, 1970; 6:03:21 UT. RS is prominent with interior detail. The NTB has faded away. The NEB has changed from grey to yellow-brown, bordered on south by very blue festoons. With the absence of SEBs, STrZ and SEBZ combine to be brightest area on planet. STB is much wider than No. 8.

10. June 19, 1970; 4:09:05 UT. RS prominent showing structure. Festoon activity.

11. May 2, 1971; 10:03:47 UT. More than a month *before* the onset of the SEB disturbance, RS is very pronounced. The SEBs is weak, and SEBZ and STZ show no detail. Colors of festoons in EZ now appear grey.

12. June 23, 1971; 5:57:36 UT. Five days *after* first observation of outbreak of SEB disturbance. The white spot that signaled the onset of the disturbance in the SEBZ is still the brightest feature on planet. A grey column has formed bridging the SEBs and SEBn. The "dent" in SEBn was formed by disturbance. NTZ is whiter than before. Reduced festoon activity.

41-B

This page is reproduced at the
back of the report by a different
reproduction method to provide
better detail.

41-B

41-C

41-C

41-D

41-D

13. June 28, 1971; 5:03:30 UT. The column of No. 12 is now well-developed. It slants in accord with differential rotation of the SEBs and SEBn. Material from the column is spreading out toward increasing longitude in the SEBs forming dark spots.

14. July 7, 1971; 6:56:11 UT. The area in which first spot occurred is now occupied by many spots. The column is now yellowish, and dark spots in SEBs are well-developed. Note detail in SEBn and NEB.

15. July 10, 1971; 5:05:49 UT. White spots have moved from SEBZ to SEBn, away from the disturbance toward decreasing longitudes. Column is more slanted. The SEBs spots are well shown, by now 70° from the outbreak of the disturbance.

16. August 5, 1971; 4:03:07 UT. Spectacular activity in SEBn. RS is still prominent.

17. August 7, 1971; 3:32:25 UT. The SEB, in complete turmoil, displays striking color differences, especially blues and dark oranges. The SEBs spots can be seen reaching 180° from the apparent source.

18. August 14, 1971; 2:54:53 UT. A large blue oval spot has developed in SEBn. Note the blending of blue and orange in SEBn, and the colorless SEBs.

19. July 20, 1971; 6:36:07 UT. SEB has returned to more normal appearance, except that the whole equatorial region is yellowish. Spots in NTrZ.

20. October 3, 1972; 1:18:56 UT. RS still prominent. Shadow of Europa is near W limb.

21. August 13, 1973; 7:49 UT. Most of yellow color has disappeared; whole equatorial region is dark. Most activity in NEB.

22. September 1, 1973; 4:03:59 UT. Detail in NEB.

23. September 22, 1973; 2:34:53 UT. RS prominent. Festoon activity in equatorial region. High-latitude spots in both hemispheres.

24. September 22, 1973; 4:26:51 UT. Detached orange spot N of NEB. Many belts at high latitudes at this longitude.

NO. 190   A REAL-TIME COMPUTER FOR MONITORING A RAPID-

SCANNING FOURIER SPECTROMETER [*]

by Guy Michel[†]

April 3, 1972

ABSTRACT

A real-time Fourier computer has been designed and tested as
part of the Lunar and Planetary Laboratory's program of airborne
infrared astronomy using Fourier spectroscopy. The value and ver-
satility of this device are demonstrated with specific examples of
laboratory and in-flight applications.

---

1.   Introduction

A real-time computer for Fourier-transform spectroscopy has been developed
at the Lunar and Planetary Laboratory for use as a monitoring device with a
rapid-scanning interferometer.   Its first application was in NASA's program of
spectroscopic observations of Mars from the CV-990 aircraft in August 1971.   We
found real-time monitoring invaluable for checking on the quality of the data
and for analyzing the behavior of the complex systems constituting our Fourier
spectrometer that are particularly sensitive to the hostile environment encount-
ered aboard aircraft.   This ability to evaluate objectively our experiment while
still in a position to modify its goals allowed us to record data superior to
thosepreviously acquired in airborne observations of Mars.

2.   Computer Organization

The basic computer (Connes and Michel 1971) is of the type developed and
used at Laboratoire Aimé Cotton (LAC), CNRS, Paris, France, with very-high-
resolution stepping interferometers (Connes 1971).   Its versatility and perfor-
mance have been increased to handle interferograms generated by the commercially-
produced, rapid-scanning interferometers used in LPL's programs.   We will briefly
recall its principles of operation and present the new features introduced in the
LPL computer.

This special-purpose digital computer (Figs. 1 and 2) is hard-wired to per-
form a discrete Fourier transform.   Each interferogram sample (10 bit + sign man-
tissa, 4 bit exponent) is multiplied by a sine function provided through an address
generator and a read-only memory (ROM, 1024 10 bit words) in which is stored a
quadrant of a sine table.   The result of the multiplication is then scaled accord-
ing to the exponent and fed into an adder connected to a circulating memory (1024
23 bit + sign words) storing the output spectrum points.   The spectrum is displayed
on an oscilloscope through a digital-to-analog converter.

The operation sequence is timed by a program generator.   The number of modes
or programs available for the transform calculation has been extended to three:
sine transform, cosine transform, and both sine and cosine transforms with power
spectrum display.   This latter mode is especially useful with fast-scanning inter-
ferometers where the zero-path point cannot be predetermined, thereby precluding
a simple sine or cosine transform.   After selecting the transform mode, the
operator dials the other initial settings: resolution in the spectrum, first
point of the spectral window to be displayed.

To maximize the speed we used the same techniques developed at LAC for the
first real-time computer, i.e., parallel computations and simultaneous operations;
but thanks to a new technique of multiplication, this speed has been increased by
a factor of two.   The computation time expressed in terms of spectrum point per
interferogram point is now 500 nsec.   If we sample the interferogram at 1 KHz,
the computer is able to produce 2048 spectrum points in the SIN or COS modes,
and 1024 points in the SIN-COS mode.   Technologically, the LPL computer is quite
different from the original LAC model.   Built two years apart, we have benefited
from the fast-growing field of integrated circuits.   The LPL computer is an all
TTL-MSI device in place of ECL and TTL.   The use of a single IC family greatly
simplified the design.   We introduced as an array multiplier a very interesting
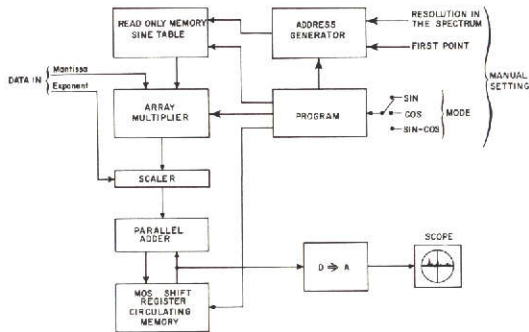
Figure 1 Block diagram of
real-time computer
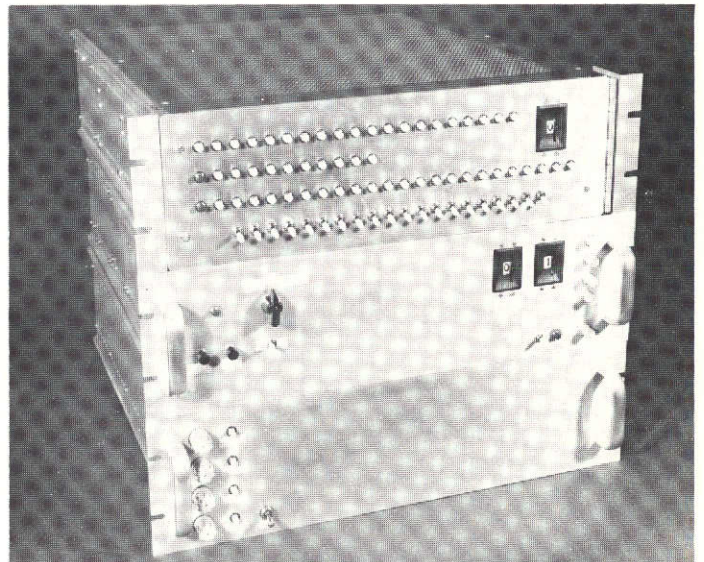
Figure 2 Complete computer system.
Top chassis is the arithmetic unit
and read-only memory. Middle chassis
houses the output spectrum memory and
function generators. Power supplies
are contained in the bottom unit
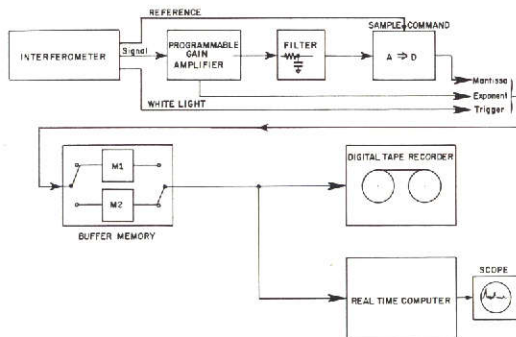
Figure 3 Connection of computer to
Fourier spectrometer. This is a
classical digitizing and recording
system for Fourier spectroscopy.
The sampling rate is always affected
by flutter due to vibrations or re-
sidual solid friction in the moving
mirror's slide. A buffer memory is
added to drive the digital tape re-
corder at a constant data rate. The
buffer memory includes two sections
of 100 words each. When one section
is accepting interferogram samples
as input, the other is reading out
at a clock rate determined by the
tape recorder
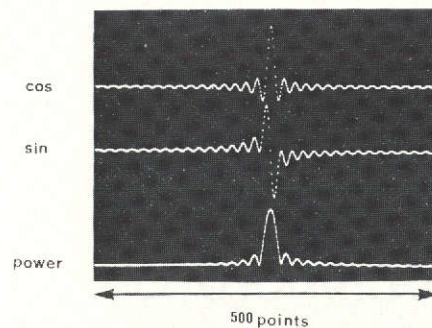
Figure 4 Transform of built-in
test function showing the three
modes of calculation available
with the real-time computer

circuit for applications where speed is at a premium (Habibi and Wintz 1970; Kingsbury 1971). In this type of multiplier the multiplication time of two N-bit words is proportional to N instead of to N^2 with the classical technique of partial products and shifts. The price paid for the increase in speed is that the number of components is proportional to N^2. The actual multiplication time of two 10 bit + sign words is less than 200 nsec. The circulating memory was built with MOS dynamic-shift registers instead of magnetostrictive delay lines. Present memory size is 1024 words with provision for extension to 8192 words. An analog apodizing interpolator using the technique of tapped delay-line filters has been built but not yet incorporated into the system.

3. Real-time Computer Mode of Operation

Figure 3 shows the connection of the computer to an experiment including the rapid-scanning interferometer, a programmable gain amplifier to handle the dynamic range of the interferogram, an analog-to-digital converter and a buffer memory necessary to drive the digital tape recorder with a constant data rate. The computer is merely connected in parallel with the recorder input and computes at full resolution a slice of the spectral range covered by the spectrometer during each scan. The computer adds coherently the successive SINE and COSINE transforms. With faint sources we can see the improvement of the S/N in the spectrum versus the number of scans. With strong sources, where a single scan is sufficient, we get from the very start an estimate of the S/N and watch the improvement in resolution.

In our rapid-scanning interferometer no provision exists to locate the zero-path point. This is not a difficulty when the interferogram is transformed later with a general-purpose computer. One usually starts the interferogram far enough before the zero-path point to include the main lobes of the interferogram. Phase correction followed by a cosine transform is one of several possible treatments that can then be used with a large, general-purpose computer. With a real-time computer this is not practical, so we have to perform a power transform where the phasing of the sampled points with respect to zero path need not be explicitly known. A power transform theoretically requires recording the interferogram over the interval (-L, +L) with the disadvantage of having to double the path difference L and the number of points to be transformed for a given resolution. To avoid these complications, we checked by simulation on a general-purpose computer that we do get a correct power transform without noticeable phase distortion if we start the interferogram a few hundreds of samples before zero path. To do so, the white-light interferogram is optically phase-shifted and its main lobe is level-detected to produce a flag pulse used to trigger the computation sequence. The computer performs the sine and cosine transforms, and displays the POWER transform by taking the square root of the sum of the squares of both transforms with fast analog circuits.

4. Preliminary Results

The following examples illustrate ways in which we have employed the computer in preparing and executing our airborne experiments. To check on its own internal functioning the computer has a built-in test generator producing the following sequence of samples: 0, +1, -1, 0, etc., which is merely the sampling of a sine

wave. The transform of this function represents the theoretical instrument func-
tion for the resolution selected. Figure 4 shows the transforms of this test
function in the three modes of computation.

Several experiments were conducted in the laboratory to evaluate the perform-
ance of our interferometer in the absence of vibrations. Real-time analysis
eliminated the need to send interferograms to a large, general-purpose computer
with consequent delays in reviewing the spectra. Figure 5 shows an absorption
band of CO used to verify the resolution achieved by the interferometer. In this
spectrum 10 scans, each of several seconds duration, were coadded.
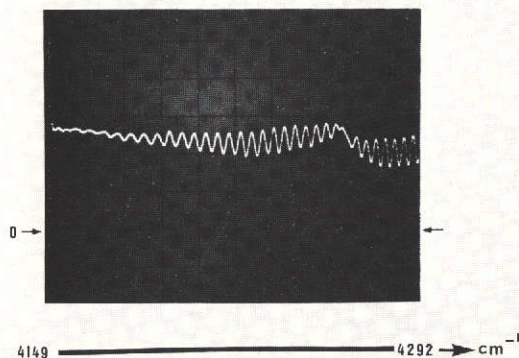
Figure 5 Laboratory test of spectrometer using
CO band at 2.35 microns. Ten power spectra were
coadded with resolution limit of 4.0 cm^{-1}

During the flights on the NASA CV-990 the computer was used in several ways
to provide important documentation on *the performance of our interferometer in the
presence of vibrations*. The first application concerned the problem of vibration
isolation of the interferometer. We designed at LPL shock mounts to attenuate
those vibration frequencies known to be severe on the aircraft. The computer pro-
vided a check on their effectiveness by serving as a real-time audio-frequency
analyzer (Bially 1970). The signal from an accelerometer located above and below
the shock mounts on our experiment was transformed, providing a real-time display
of the aircraft vibration spectrum and the residual vibrations seen by the inter-
ferometer. Figure 6 shows such vibration spectra verifying the general attenuation
of all aircraft frequencies and the absence of any resonant vibration in the inter-
ferometer's mount.

The sensitivity of the moving mirror to residual vibrations cast doubt on the
ability of the interferometer to perform efficiently at maximum resolution aboard
the aircraft. Again, the advantages of real-time analysis permitted us to study
this problem in flight with subsequent modifications to the experiment that re-
sulted in most effective use of our quite-limited and very-expensive observing time.
By examining the reproducibility of high-resolution features of single scans of the
Sun recorded in flight, we were able to select a resolution that guaranteed the best
return from our Mars observations. Figure 7 shows a resolved CO_2 band at near maxi-
mum resolution (0.67 cm^{-1}), from a single scan of the Sun used for this purpose.

Finally, the computer was used in the actual observing runs providing a con-
tinual check on the acquisition of good data. Figure 8 contains portions of the
spectrum of Mars seen by the real-time computer showing strong CO_2 bands in the
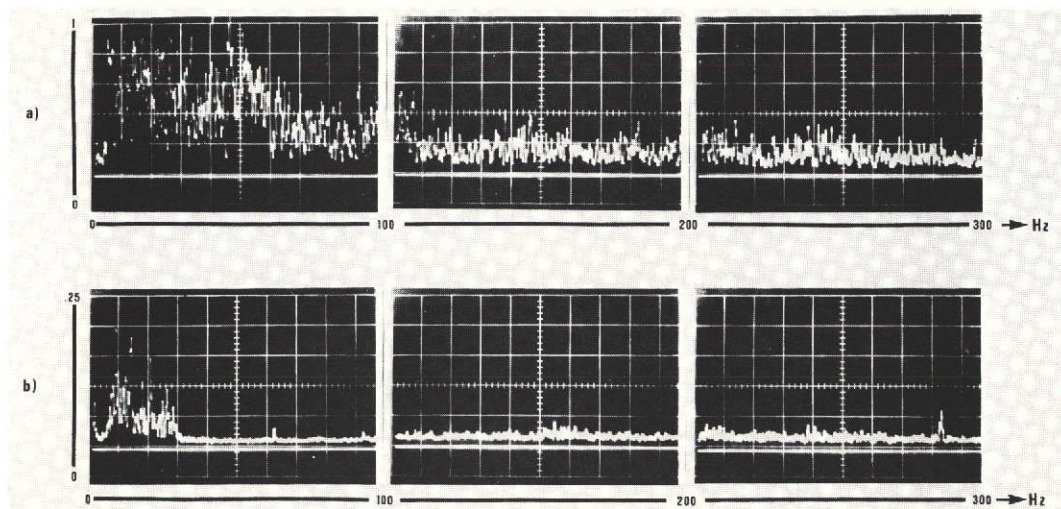
Figure 6 Aircraft vibration spectra produced by computer. The series of spectra in (a) and (b) were produced from an accelerometer located, respectively, before and after the shock mounts used to isolate the interferometer from the aircraft. The accelerometer axis was parallel to the main axis of the aircraft and to the translation axis of the moving mirror of the interferometer. Acceleration is in arbitrary units; note the change between series (a) and (b)

2 micron region. After coadding just 10 scans, each of 9 seconds duration, the continuum level has been established although only a suggestion of the CO_2 absorptions exists. After 600 scans the S/N has increased, as expected, and the CO_2 triad at 2 microns is now quite evident. In addition, the H_2O band at 1.9 microns has emerged from the noise. By watching the real-time development of the Mars spectrum during our first flight, we were able to predict with accuracy the averaged result of all four scheduled flights. We decided that following the flight schedule as planned would lead to useful spectra, a conclusion later verified by complete data reduction at LPL.

5. Conclusions

The effectiveness of the real-time analysis offered by this small, special-purpose computer has been demonstrated through actual use in an airborne spectroscopy program. The experience acquired in these first experiments will result in improvements to both the computer and the interferometer, creating an even more effective combination. In addition, this computer will be attached to another spectrometer, the first high-resolution stepping interferometer built by Dr. Pierre Connes (Connes and Connes 1966) and now in use by LPL staff at the Steward Observatory 90-inch telescope on Kitt Peak. The availability and versatility of this computer effectively eliminates a frequently-voiced criticism of Fourier spectroscopy, the inability to see the spectra until some time, often days, after recording the interferograms.
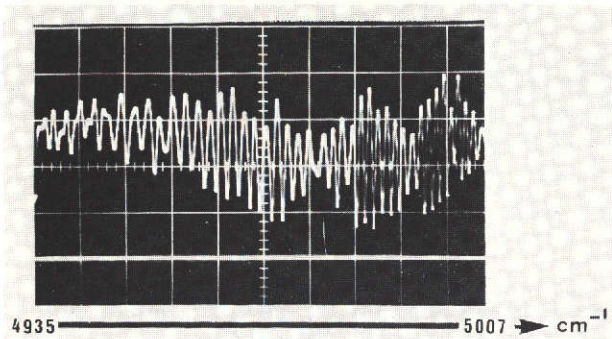
Figure 7   High-resolution test of
spectrometer in flight.   Single scan
(24.5 sec) of the Sun showing CO_2
band at 2 microns with a resolution
limit of 0.67 cm-1

Figure 8 (right)   Real-time monitoring of
spectrum of Mars. The window selected in-
cludes the strong CO_2 absorptions at 2
microns and the water-vapor band at 1.9
microns.   Upper trace is coadded result
of just 10 scans (80 secs of observing).
Lower trace includes 600 scans and exhibits
the expected improvement in S/N
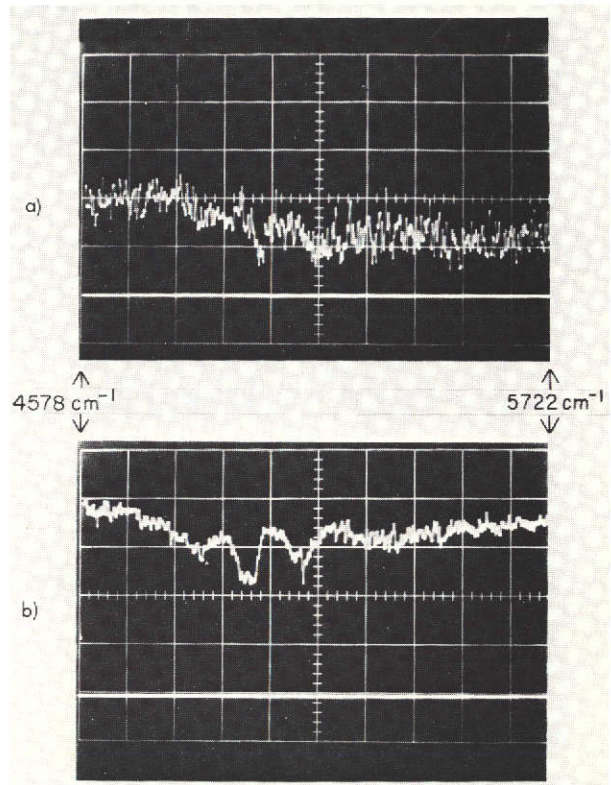
REFERENCES

Bially, T. 1970, IEEE Trans. on Audio and Electroacoustics, *AU-18*, 201-203.
Connes, P. 1971, AFCRL-71-0019 Special Reports No. 114, 121-125.
Connes, P. and Michel, G. 1971, AFCRL-71-0019 Special Reports No. 114, 313-330.
Connes, J. and Connes, P. 1966, *J. Opt. Soc. Am.*, *56*, 896-910.
Habibi, A. and Wintz, P. 1970, IEEE Trans. Electronic Computers, *C-19*, 153-157.
Kingsbury, H. G. 1971, *Electronic Letters*, *7*, 277-278.

NO. 191   ON THE CAPABILITIES OF THE SPIN-SCAN   IMAGING TECHNIQUE*

by T. Gehrels
and
V. E. Suomi and R. J. Krauss
Space Science and Engineering Center, The University of Wisconsin
Madison, Wisconsin

ABSTRACT

A summary description is made of spin-scanning devices for various space missions. Compared to television, scan-imaging has remarkable advantages and these are listed at the end of the paper.

The first spin-scan imaging camera was conceived by V. E. Suomi for the Applied Technology Satellite ATS-I and built by the Santa Barbara Research Center. It was launched into geostationary orbit over the Pacific Ocean in December 1966 and has been in continuous operation ever since. An improved

---

instrument, the Multicolor Spin-Scan Cloud Camera (MSSCC) was launched in November 1967 on ATS-III. It is situated at 35,800 km altitude above the Amazon River and still being used on a regular daily schedule.

The two cameras are quite similar in size and design, with the primary difference being that the ATS-I camera is monochromatic, using a single S-11 photomultiplier filtered to give a response of 0.475-0.630μ. The ATS-III camera has a 12.5 cm Wynn-Rosin telescope (elliptical primary and spherical secondary mirror) F/3, with three photo-etched circular apertures used as field stops in the focal plane, each 38μ in diameter, giving a resolution of 100μr or 3.6 km on the surface of the earth at the satellite subpoint.

The field stop apertures admit light to flexible glass fibers which are used to transport light to the three photomultiplier sensors mounted on the camera frame separate from the movable telescope. The photocathodes used are S-20 for the red channel (0.55-0.63μ) and S-11 for the green and blue channels (0.48-0.58μ and 0.38-0.48μ).

The telescope is stepped in latitude by 0.13 milli-radians once each spacecraft revolution. The stepping motion is from north to south, while the spacecraft spin axis is parallel to that of the earth. Thus, at 100 rpm nominal spin rate, a full disk image of the earth 18° wide is generated in 2407 lines in 24 minutes. The instantaneous field of view dwell time is 10μ sec although horizontal sampling can be done every 3.5μ sec to take full advantage of the available communications bandwith.

The principal interest for this COSPAR Symposium lies in high resolution. The resolution, generally, can be improved by reducing focal-plane aperture size and/or going to a larger focal length. Either solution will require increased information bandwidth and correspondingly degraded signal-to-noise ratio. The photomultiplier reaction time may also become a problem as the field of view dwell time decreases. All of these drawbacks can be counteracted by slowing down the *spin rate* of the spacecraft and/or using a larger *telescope diameter*. The exact trade-offs to be made depend on the practical system constraints.

As an example, the second-generation Visible Infrared Spin-Scan Radiometer (VISSR) to be flown on the Synchronous Meteorological Satellite (SMS) in October 1972 is constrained to have a 20-minute picture time, 70-kg combined instrument and electronics weight, and 1-km ground resolution with 2.8:1 signal-to-noise ratio at 0.5% albedo and a visible bandpass of 0.55-0.75μ. The thermal-imaging channels are to have $\leq$1.4°K noise-equivalent temperature difference for a 200°K scene. The resulting design is a 40.6-cm diameter F/7 all-reflective Ritchey Chrétien (aspheric) telescope with 2.91 m effective focal length. The photomultiplier sensors for the visible channels are operated in parallel behind rectangular glass fibers whose ends form 61μ x 73μ field-stop apertures in the primary focal plane, yielding resolution of approximately 25μr with a 2.4μ sec dwell time at 100 rpm. Information bandwidth and photomultiplier response time are adequate. The thermal-channel images in the 10.5-12.6μ atmospheric-window band using radiatively-cooled HgCdTe intrinsic IR detectors with 0.25 mr resolution.

The Multispectral Scanner (MSS) also being built by the Santa Barbara Research Center for the polar orbiting Earth Resources Technology Satellite (ERTS) utilizes a 23-cm aperture F/3.3 Cassegrain telescope with 59μ square glass fibers as field stops. This yields 77μr resolution from low orbit (~65 m ground resolution at nadir). Photomultipliers are used for three observation channels in the 0.5-0.8μ region and photodiodes for a 0.8-1.1μ band. In addition, HgCdTe detectors are used for thermal imaging in the 11μ window.

Infrared imaging and radiometry from earth orbiters has also been done with point scanning sensors in the Nimbus weather satellite program (the Medium Resolution and High Resolution Infrared Radiometer experiments) and in the Improved TIROS Operational Satellite (ITOS) scanning radiometer. A picture obtained on ITOS-1 is on the front cover of the 6 August 1971 issue of *Science* (Rao *et al.*, 1971). Currently, improved scanners are under development for ITOS. Two of us (Suomi and Krauss) proposed a Line Scan Radiometer (LSR) for the Mariner Venus/ Mercury 1973 (MVM) mission. The camera used the slow attitude drift of the 3-axis stabilized spacecraft to generate the line stepping function and a small focal- plane scan-mirror to generate the scan along a line, substituting for the absence of spacecraft spin. The lead time available was unfortunately not sufficient to carry the concept through breadboard stage to flight hardware and an essentially pre-existing TV system with new optics will be used on the mission instead.

Consequently, the Imaging Photopolarimeter experiment of Gehrels on Pioneer F and G (F to be launched in March 1972) is the only line scan imager now being applied to non-earth oriented missions. As such, it is not a good example for high resolution because the resolution was restricted by spacecraft capabilities. The Pioneer is small and provides for a relatively cheap reconnaissance mission of the asteroid belt and of the Jovian radiation environment, as a precursor for more sophisticated missions such as the Grand Tour of the Outer Planets, for which launch dates exist in 1977 and 1979. The Pioneer data link handles, when near Jupiter, at best 2048 bits/s. There is no on-board data storage, only a buffer, and the best ground resolution at closest encounter (2 Jupiter radii from the surface) will be 150 km compared with the best earthbased resolution of 600 km.

Considering the 5 rpm spin of the spacecraft, the 2048 bits/s data link and other spacecraft limitations, 600μr is an optimum limit to the resolution. Consequently, a 2.5-cm telescope was large enough, and the instrument itself weighs 5 kg - an optimum weight since the mission could accommodate it without eliminating other experiments. The advantages over a television system were studied at the time and the simplicity of an instrument using photomultipliers was important. Vidicons are considered to be more susceptible to the Jovian radiation belt. The fact that television would have taken a shorter exposure - a fraction of a second, compared to several minutes for a spin scan - would have reduced the image rectification problem which is considerable for a flyby of Jupiter as we are dealing with a fast trajectory of a rotating spacecraft flying past a rotating planet. The scan lines are far from straight. On the other hand, the geometric reconstruction is straightforward if good timing information and trajectory data are available. Television would be subject to smear limitations and small frame size and has its own peculiar brand of geometric distortions and photometric nonlinearities, especially at the edge of the field.

The imaging of Jupiter will be in two colors: blue (0.390-0.500μ) and red (0.595-0.720μ), and the range of visible phase angles will be quite large - much better than from earth. Besides the imaging capability, photopolarimetric data will be obtainable. These modifications are easily added to produce the combination for the Pioneer F and G Missions known as the Imaging Photopolarimeter. The data processing of the imaging is being developed by W. Swindell of the Optical Sciences Center at the University of Arizona. Details of the instrument have been published by KenKnight (1971).

A reasonable system for an outer-planet spacecraft with a sufficient data link would start with a 25-cm diameter telescope to keep the system weight down. Photo-etched field stops can be made in the 30-40μ range. Smaller sizes tend to have imperfections and rough edges. The same is true for glass fibers. While 5μ fibers can be drawn, the ends cannot be finished smooth enough to avoid large transmission losses. About 40μ is the present limit. Figure 1 shows what a 25-cm optical system can produce in resolution at 10:1 signal-to-noise ratio as a function of planet brightness (the vertical bars range from 0.1% to 100% albedo) and information bandwidth. A 10-μr resolution appears to be a reasonable limit. A relay-lens system should shorten the effective back focal length for IR imaging since smaller detectors are better. With ease, one could add a 10-μr field of view in the visible channel for highest resolution simply by increasing effective front focal length to 4 meters (F/16) and tolerating the reduction in signal-to-noise ratio.
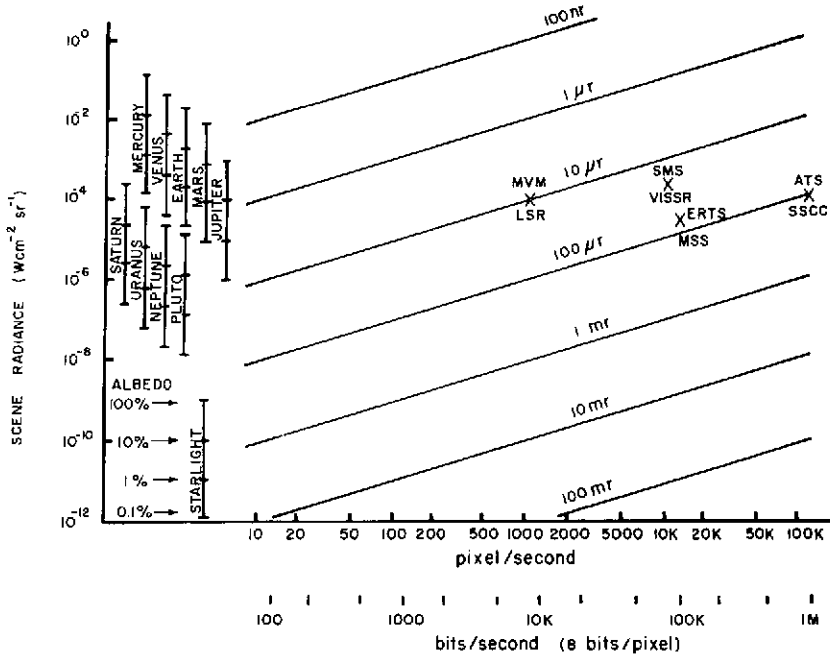
Figure 1   Resolution per scan line (25-cm optics, 10:1 signal-to-noise ratio at 50% response to 2:1 contrast target). The abbreviations of various space missions and instruments are explained in the text

In summary, the disadvantages of the spin-scan technique are (1) that it is not as "instantaneous"as television, (2) that the instrument requires a spinning spacecraft or mechanical scan mechanism, and (3) that it requires duty-cycle expansion and a buffer to best utilize the communications link.

We can name seven advantages of the spin-scan technique over a television system: (1) practically unlimited format of the field, whereas the 800-line scan of television will image only a part of the planet, and even at that the television has edge distortions; (2) the detectors are rugged and have wide dynamic range; (3) multiple detectors allow a wide spectral range; (4) multiple perfectly-registered images in several colors can be made by scanning with several detectors operating simultaneously; (5) the detectors are linear – ideal for combination with a photopolarimeter of $\pm0.1\%$ precision; (6) redundancy in detectors is implicit in the design, yielding extremely high reliability,and (7) the instrument is relatively cheap and lightweight. Even at a heavy duty cycle as on ATS-III, the instrument is proving to be a workhorse of long life.

REFERENCES

KenKnight, C. E. 1971, "Observations in the Asteroid Belt with the Imaging photopolarimeter of Pioneers F and G". In PHYSICAL STUDIES OF MINOR PLANETS, T. Gehrels, Ed. NASA SP-267, National Aeronautics and Space Administration, Washington, D. C.

Rao, P. K., Strong, A. E., and Koffler, R. 1971, "Gulf Stream and Middle Atlantic Bight: Complex Thermal Structure as Seen from an Environmental Satellite", *Science, 173,* 529-530.

NO. 192 HIGH RESOLUTION PLANETARY OBSERVATION[*]

by Gerard P. Kuiper

June 1971

ABSTRACT

High-resolution ground-based planetary observations, visual and photographic, have,for several decades,seemed to have reached a rather firm limit. The causes for this restriction are briefly reviewed. At the time when space probes make major advances possible, at incomparably higher levels of expenditure, the need arises to re-examine the limiting factors of earth-based planetary resolution. In addition to familiar refinements (of which seven are listed) carried somewhat further, a specific approach, yet insufficiently developed, is the study of the atmospheric boundary layer over the observatory site and the use of an appropriately elevated station. The required elevation may be determined acoustically.

Planetary observation, both visual and photographic, has always depended on
the best image quality (seeing) available. In this respect its main requirement
is identical to that of double-star observation. Almost any observing site ex-
periences exquisite seeing at some time. Sites differ in the *frequency* of such
occurrences and in the more readily ascertainable total fractions of clear weather.
Tropical sites have a large fraction of good seeing on the nights that are clear,
though the frequency of clear nights depends on location and on the monsoon. For
instance, at the Bosscha Observatory in Java the seeing is almost always satis-
factory whenever the sky is clear, with visual resolution of 0.2 arc sec regularly
achievable with the 60-cm visual telescope. In the latitudes 25-35° of both hemi-
spheres, the fraction of clear nights is the largest (with local exceptions) and
the seeing is good-to-excellent a fair fraction of the time, particularly close to
the western shores of various continents. Large continental masses appear to have
a disturbing effect on the air parcels so that good seeing is less frequent far
away from these shores. This rule has only a statistical validity; exceptional
weather conditions may occur anywhere.

With a large telescope of high quality, in excellent adjustment, the limit of
visual resolution is always near the theoretical diffraction limit. I have obser-
ved double stars, of $0\overset{''}{.}06$ (arc sec) separation, such as 20 Persei, repeatedly with
the 82-inch telescope of the McDonald Observatory and measured the planet Pluto,
the satellites of Saturn, and Triton of Neptune with the 200-inch Hale telescope.
The measured diameter of Pluto was $0\overset{''}{.}23 \pm 0.01$ [1], and for the Saturn satellites
and Triton [2] the following: "5 July 1954, Enceladus $(0\overset{''}{.}08)$, Tethys $(0\overset{''}{.}12)$,
Dione $(0\overset{''}{.}12)$, Rhea $(0\overset{''}{.}24)$, Titan $(0\overset{''}{.}67)$, Iapetus $(0\overset{''}{.}195)$, all at 9.43 astr. units;
and Triton $(0\overset{''}{.}173)$ and Neptune $(2\overset{''}{.}06)$, both at 30.1 astr. units". (Stars were
found to have spurious disks of about $0\overset{''}{.}05$, a value attributable to the Ross cor-
rector lens at the prime focus, which for safety reasons had to remain in place
during measurements, made in the prime focus cage).

High *photographic resolution* is not obtained nearly as readily as high visual
resolution. This appears due to the fact that high visual resolution results from
continued observation over many seconds to several minutes, during which the eye
and brain reject all visual records that do not reach to the desired standard,
and retain for "storage" only the best 10^3-10^4 individual impressions. The photo-
graphic plate can simulate this process to some extent by the use of multiple expo-
sures. Also, the photography can be monitored, by the observer watching the image
and selecting the best moments for the exposures or by some automatic device based
on image size. During a program of systematic planetary photography with the 82-
inch of the McDonald Observatory in 1948, using both color film and black-and-white,
the resolution gap between visual and photographic observation was found to be a
factor of about 4. Since then, with improved emulsions and improved thermal con-
trol of the air in both telescope and dome, the gap has been narrowed to about 2.
Thus, the best photographic resolution obtained with the 61-inch telescope,whose
Airy disk in visual light is 0.075 arc sec, is about 0.15 arc sec. (Achieved many
times in the CONSOLIDATED LUNAR ATLAS, 1967, e.g. on the Clavius photograph used
as the frontispiece). The finest Jupiter detail recorded on color film has dimen-
sions of $0\overset{''}{.}12$-$0\overset{''}{.}15$, though $0\overset{''}{.}2$ is more common. Under good-to-average conditions
of seeing there often is *no gap*, with all that is seen recorded photographically.

Numerous details affecting the *thermal regimes of telescope and dome* must be watched if maximum photographic resolution is to be achieved. Unfortunately, insufficient attention has been given to these factors in some observatories built on excellent sites. Briefly, the requirements are: (i) the entire observatory area must have a good climate in the usual astronomical sense, not too far from the western shore of a continent or on a favorably-located island; (ii) the building must be elevated, for the slit opening to be well above the atmospheric boundary layer caused by local topographic features, trees, etc. This level is determined by tests with small balloons and smoke bombs which make the air flow pattern visible. (iii) The building itself should be cylindrical, with a hemispherical dome, having a slit that moves up and over (not horizontally moving doors). This cylindrical observatory should have a diameter not greater than necessary to house the telescope. (iv) The dome should be painted white (TiO_2), which reflects more than 3/4 of the incident sunlight and effectively re-radiates in the infrared the small part absorbed; thus the outer surface remains cool during the day and cools rapidly at night, preventing an updraft of warm air from the building in front of the dome slit. (v) The thermal inertia of the dome should be minimal to achieve equalization of temperatures at night. This is also the cheapest way of building a dome, since a single metal skin over a rib structure of I-beams suffices. (vi) Inside the dome one should have 3 or 4 large exhaust fans spread in azimuth, at about the observing level, capable of running at different speeds, adjusted during operations to cause an inflow of air through the slit at a rate not so rapid as to cause turbulence. This can be checked from the Foucault test. The best arrangement is found to depend on the wind direction and speed. (vii) Small exhaust fans are also placed around the primary mirror to prevent the formation of air bubbles over it with temperature slightly different from that of the ambient air. These bubbles are well known to all visual observers who have studied the Foucault patterns of bright stars. The average diameter of such bubbles, when permitted to form, appears to be 30-40 cm. (The 82-inch telescope showed usually about 20 of them; the 200-inch, approximately 100). The bubbles grow to full size in 10-30 seconds, and then take off and rise, being replaced by cooler air. The (warm) bubbles act like weak negative lenses and cause the telescopic image to be that of a multiple interferometer. Stellar images are usually confined to an overall diameter of about 0.3 arc sec, containing from 5 to 15 visible components which slowly move over each other with a relaxation time of a few seconds. In double-star observations, one picks the brightest of these images for measurement but planetary photography is, of course, degraded. Experience has shown that these bubbles can indeed be prevented.

Considerable study of photographic materials, image sizes, and development techniques is also essential. In our color photography we have found High-Speed Ektachrome or, more recently, Ektachrome EF, to be the most satisfactory, not used routinely, however. In addition to normal exposures, processed commercially, we expose several rolls at 1/4 of the normal time (1/8s vs. 1/2s for Jupiter at F/75, or F = 115m) and compensate for this by special processing. This may lead to distinctly improved definition though often increased graininess and lack of good color balance that must be verified and corrected in copying with normal exposures. We have also found that underexposed (dark-looking) color frames can be copied with corrective filters to normal-appearing frames. This also requires that some normal exposures are available for reference, though these may have less resolution.

An examination of some 12,000 color frames of Jupiter (and many more black-and-white frames) obtained since October 8, 1965, when operations with the 61-inch telescope started, showed that with no more than 1/4 of the telescope time assigned to planetary photography each month, on almost every month a series of exquisite color photographs was obtained, supported by approximately three times the number of black-and-white photographs taken through filters, ultraviolet to infrared. Important supplementary series were acquired each month.

As regards the *use* of planetary photographs, with low-contrast features such as the clouds of Venus, composite prints are the most informative: one may combine from 5 to 10 frames into a single print, increase the contrast, and take out mechanically a linear gradient across the terminator.

The *examination* of the color photographs is best made in binocular vision, using two selected frames. Then, one is able to reject immediately all minor defects, such as scratches, which would be retained, though reduced, in composites. Binocular vision further appreciably enhances visibility of faint contrasts and minute details, giving the impression of a gain in resolution of approximately 1.5 over single frames. Accordingly, this Laboratory is preparing a file of color copies for the planet Jupiter, all 20mm in diameter, containing all frames from the original set of 12,000, that appear to contribute independent information. This number is larger than might be expected since the resolution is not constant over the entire planetary disk, so that many frames must be consulted. The number of frames actually selected for copying is about 1,500. A companion file of supporting black-and-white filter photographs will also be produced. Because of the longer wavelengths and higher contrast, the High-Speed IR frames often show somewhat higher resolution.

The *wavelength dependence* of photographic resolution is interesting. On moderately good nights, the resolution may go as $1/\lambda$; on poor nights, no λ effect is noted. This agrees with the visual impression that on poor nights the blurred stellar images do not have a blue fringe. The $1/\lambda$ effect on good nights is probably due to the near-validity of the Rayleigh criterion for good images (deviations less than $\lambda/4$ in the wave front). The criterion may be satisfied from 0.7-0.9μm (High Speed IR), but not 0.35-0.5μm, making a factor of 2 difference in resolution. Unfortunately, fast films beyond 0.9μm are not available or they would further improve earth-based resolution in planetary photography with large telescopes, possibly further closing the resolution gap referred to. For low-contrast features no gap is present.

Color photography has added a new dimension to photography of the planets. For Jupiter and Saturn the classification of clouds by color almost certainly is a classification by composition; and presumably also one of elevation within the atmosphere. The belts, when observed under the best conditions, usually break up into dozens of individual clouds all of the same color, suggesting a repetitive process of their formation. They appear analogous to terrestrial cloud streams formed by large forest fires or volcanic eruptions. The study of the Jovian planets will be one of the most active scientific endeavors of the 1970's; ground-based astronomy, if carried to the limits of its capabilities, will be able to contribute greatly in two main areas: atmospheric circulation and cloud composition. With still better facilities, resolutions down to 0.10 arc sec should be achievable on a fairly regular basis, on both High-Speed IR and fast color film.

Data processing, with allowance for the image blur function, can always yield
another factor of about 2 in image definition, as was first demonstrated in 1956
at Johns Hopkins University, and has, for example, been practiced in the process-
ing of the Ranger television records by the Jet Propulsion Laboratory in NASA's
Ranger Reports (1965, 1966).

Reference must also be made to the exquisite planetary photography with the
new 108-cm telescope at the Pic-du-Midi, clearly a superior site that will merit
further development; to the important comparative site tests in California by
Walker [3], recently extended to other sites in North and South America and
Australia [4]; and the extensive tests carried out from July 1965 to October 1969
in France, Spain, and Baja California, by the Paris-Meudon Observatory team (in-
terim reports by INAG). Earlier notable contributions are those by F. G. Pease
with the 100-inch telescope of the Mt. Wilson Observatory (lunar and planetary
photography in the 1920's); with the Lick 36-inch telescope by J. H. Moore and
F. Chappell (the moon about 1937) and by H. M. Jeffers (Mars 1950-1960); by R. B.
Leighton with the Mt. Wilson 60-inch telescope in 1960's, by M. L. Humason with
the 200-inch [5] and by G. H. Herbig with the Lick 120-inch telescope, both at
the coudé focus; by W. S. Finsen with the 26-inch telescope of the Union Obser-
vatory (Mars in 1954 and 1956 [5]);and by E. C. Slipher with various telescopes,
especially the Lowell Observatory 24-inch and the Lamont-Hussey 27-inch at Bloem-
fontein, South Africa [6]. The total photographic program represents a tremendous
effort (about 1,000,000 planetary and lunar photographs). This may have created
the general impression among astronomers that the limits of this technique have
been reached. No doubt further progress will be difficult and will require ad-
ditional refinements and even new approaches if not better observing sites; but
it is also true that *resolutions of 0".1 must be achievable photographically as
they have been achieved visually at all large observatories since the 1890's.*

It is probable that the most important advance still within reach is one of
seeking the *optimum elevations* above selected observing sites. Related to this
is the determination of the vertical distribution of seeing disturbances within
the first few hundred feet above the ground, the region usually assumed to be
responsible for the major part of the seeing disturbances, and improved dome-
tower design, so as to avoid the creation of new local disturbances. The atmo-
sphericprofile may be tested for irregularities in the refractive index by acous-
tical methods having a sensitivity some 1700x the optical sensitivity [7]. The
premium on achieving resolution of about 0".1 regularly, especially during the
next decade in the study of Jupiter and Saturn, is so great, in view of the pro-
hibitively expensive alternative of observing changing cloud-covered surface
from space probes, that these further efforts in ground-based photography are
warranted. It is true that a resolution of 0".1 might be achievable also from a
1-3m telescope in orbit, but the problems with this approach may have been under-
estimated. In any case, ground-based planetary photography of highest possible
resolution will remain a prime goal.

REFERENCES

[1] G. P. Kuiper, *Publ. Astr. Soc. Pacific, 62,* 133 (1950).
[2] *Trans. Int. Astron. Un., 9,* 250 (1955).
[3] M. F. Walker, *Publ. Astr. Soc. Pacific, 82,* 672 (1970).
[4] M. F. Walker, *Publ. Astr. Soc. Pacific, 83,* 1401 (1971).
[5] Summarized with reproductions in Chapters 16 and 17 of PLANETS AND SATEL-
     LITES: THE SOLAR SYSTEM, VOL. III, University of Chicago Press 1961.
[6] E. C. Slipher, BRIGHTER PLANETS, National Geographic Society and Lowell
     Observatory 1964.
[7] Freeman F. Hall Jr., "Acoustic Remote Sensing of Temperature and Velocity
     Structure in the Atmosphere", STATISTICAL METHODS AND INSTRUMENTATION IN
     RADIO METEOROLOGY, A. G. Kjelaas, ed., Teknologisk Forlag A/S, Oslo (1971).

NO. 193 WATER-VAPOR MEASURES, MT. LEMMON AREA

by G. P. Kuiper and L. Randić

August 1, 1973

ABSTRACT

Daytime atmospheric water-vapor measures were continued for Mt. Lemmon, the Catalina Observatory, and Tucson. As before (*LPL Comm. No. 158*), the three sets are closely related in terms of their altitude differences, with the average empirically-determined scale-height value, 2.3 km. During the Winter and Spring of 1971 observations were made for more than 90% of the days. The measures are listed in Tables I, II, and III, and are shown, reduced to Mt. Lemmon, in Figures 1 and 2. For comparison, Figures 3-6 show the 1969-70 data published in *LPL Communication No. 158*. The averages for the stations are shown in Figure 7.

The instrumental scale was checked in *LPL Communication No. 159* and confirmed below 2.2 mm; above this value a gradual departure set in, still uncertain beyond 3.0 mm. In this paper the calibration was continued to higher values by means of atmospheric radio-sonde data. Tables I-III and Figures 1-6 have been kept in the old scale (used in *LPL Comm. No. 158*); but the ordinates in the final Figure 7 have been adjusted to the readings of the radio-sonde data.

Section 3 interprets the nature of the fluctuations shown in
Figure 7 in terms of air masses of different origins, identified
with the aid of radio-sonde wind directions for the upper atmo-
sphere derived locally, above the Tucson airport.

1.   Introduction

This paper is a continuation of *LPL Communication No. 158* (containing H_2O
measures made in 1969 and 1970), which in turn followed the more general study of
astronomical high-altitude sites in *LPL Communications Nos. 142, 156,* and *157; No.
157* dealt with the medical problems.   The present paper together with *No. 158*
cover a fairly representative set of data for the *annual* run of H_2O values and
its short-period *variations* above Mt. Lemmon.   One more set of data, taken in
1971-72, will be published separately.

2.   The Measures

The measures here presented were made with the solar-beam H_2O meter, developed
and lent for this purpose by Dr. Frank Low.   Its calibration was tested in *LPL
Communication No. 159,* where Dr. Low's original calibrations were found confirmed
up to 2.2 mm H_2O, at which point a small deviation began up to 3 mm H_2O.   Beyond
3 mm no verification was possible with the new data.   In this paper the calibration
is extended to higher H_2O readings with the use of radio-sonde data taken at the
Tucson International Airport that measure the atmospheric water-vapor profile from
920-7 mb.   It is found that the tabular readings above 3 mm must be corrected up-
ward, as was suspected in *LPL Communication No. 159,* p. 398, while the lower values
are again confirmed (most past uses of the instrument have been concerned with low
and very low readings).

The most practical way to carry out this program appeared to be to present
the 1971 data by listing in Tables I, II, and III, the "tabular" H_2O readings in
the same manner as was done in *LPL Communication No. 158* for 1969 and 1970; then
plot the 1971 results (Figs. 1 and 2) as well as the published 1969-70 values
(Figs. 3-6); and combine the data from the three observing stations into a single
set of graphs (Fig. 7).   Representative maxima and minima of this graph were then
compared with the H_2O contents above Mt. Lemmon based on the free-atmosphere radio-
sonde data for those times; the radio-sonde abundances reduced to "equivalent"
H_2O absorptions with allowance for the mean pressure for the H_2O in the atmosphere
above Mt. Lemmon, 600 mb (cf. *LPL Comm. No. 158,* p. 394); whereupon the scale cor-
rection was derived for the higher readings and applied to the ordinates of Figure 7.

At the other extreme, the lowest readings of the radio-sonde calibration give
only an *upper limit.*   On dry nights the *reported* relative humidities are usually
14%, which is the recording limit of the equipment; some values may be considerably
less (comments on "motor boating" of the airborne humidity equipment were made in
LPL Communication No. 142, p. 126).

As in *LPL Communication No. 158,* Table I lists the measures made from the roof
of the Space Sciences Building in Tucson; Table II, measures made at the Mt. Lemmon
solar observatory (60 feet below the summit); and Table III, measures made at the
Catalina Observatory.   The equivalent values for Mt. Lemmon given in Tables I and
III are computed from the preceding columns, allowing for the elevation differences.

Figure 1   Tucson daytime H_2O measures reduced to Mt. Lemmon
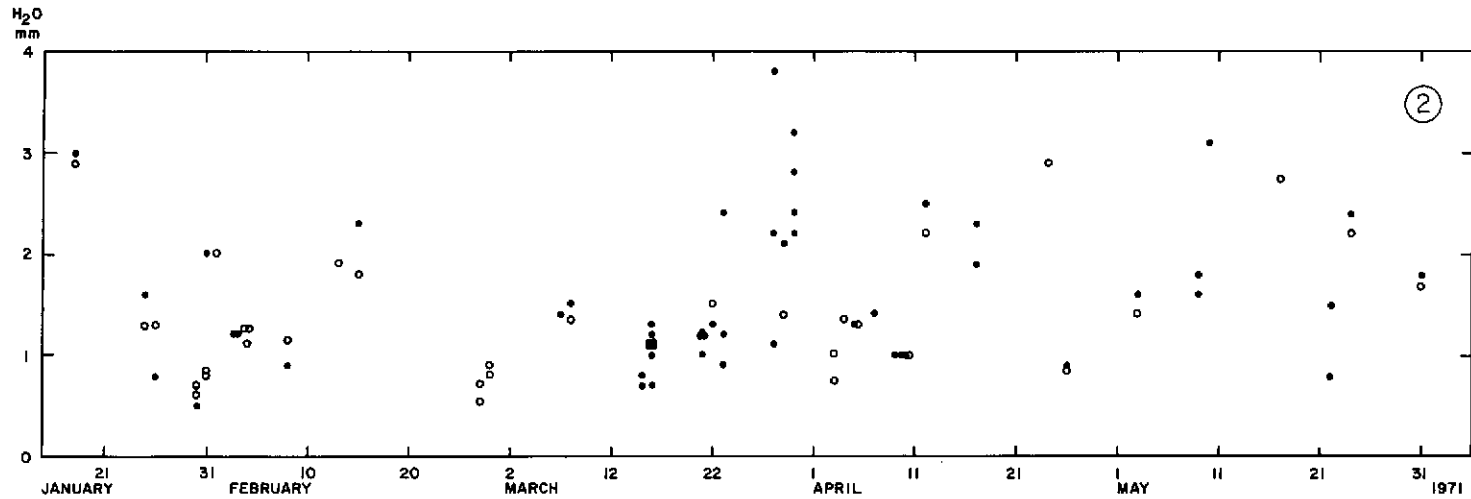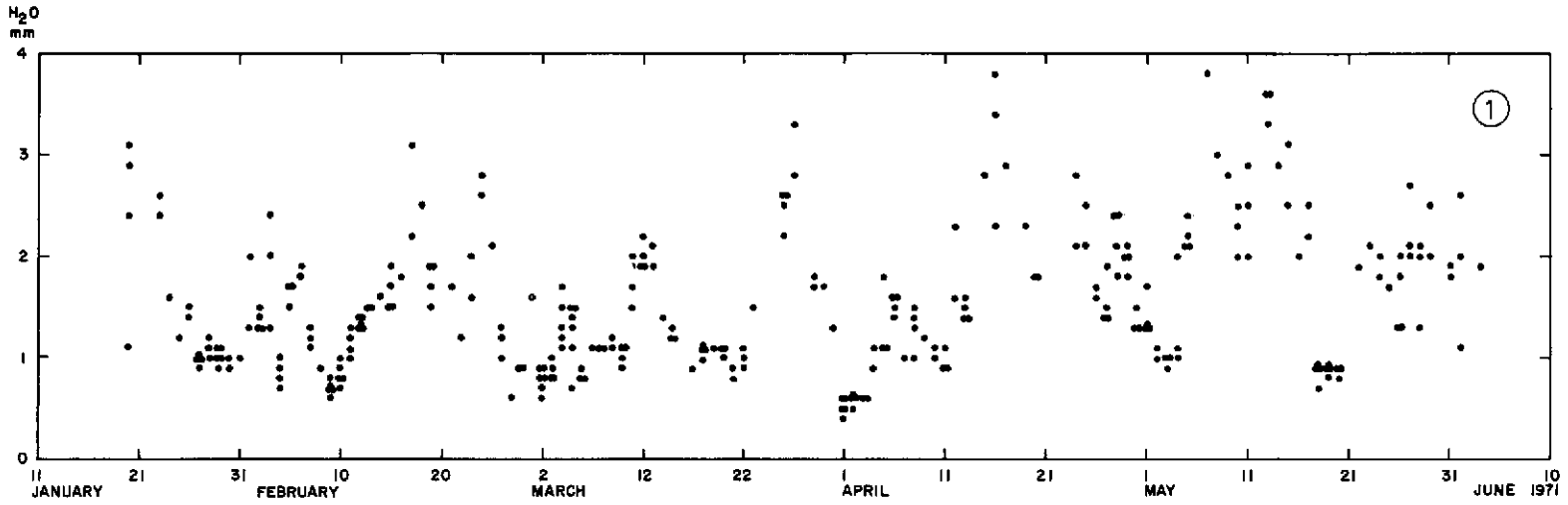
Figure 2   Mt. Lemmon daytime H_2O measures (dots) and Catalina (circles)

Figure 3   Tucson daytime H_2O measures reduced to Mt. Lemmon.   Precedes Fig. 1
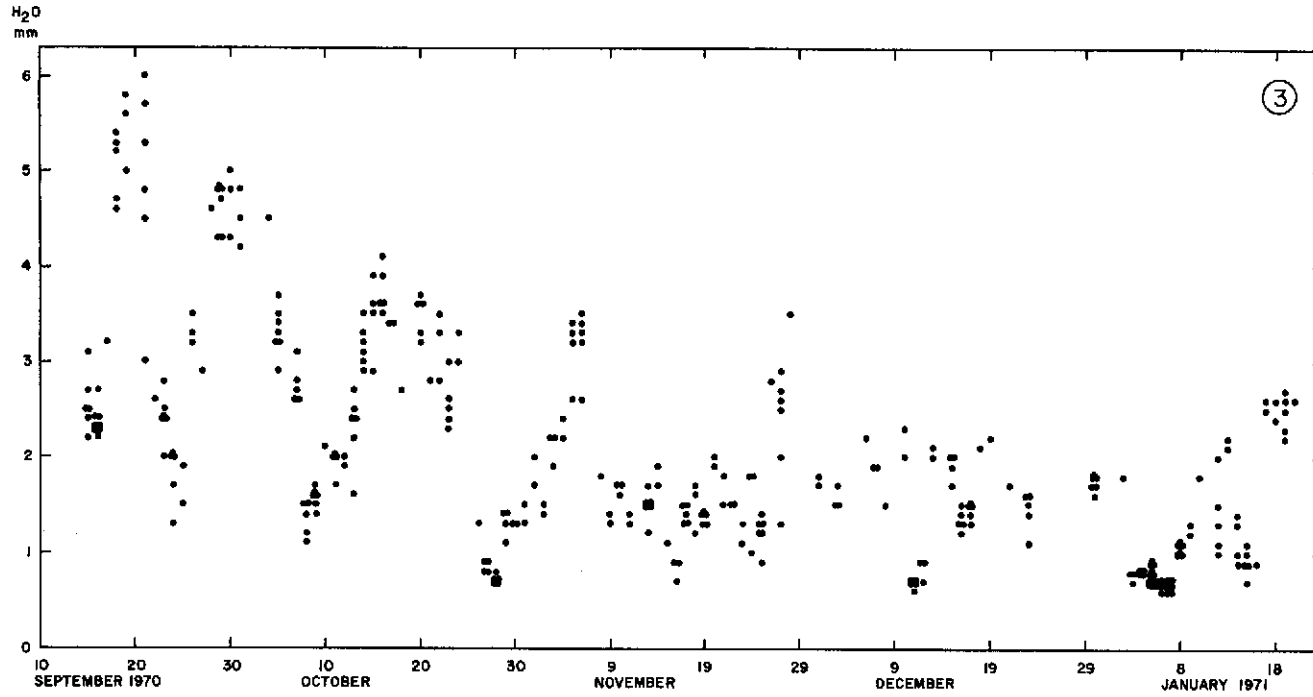
Figure 4   Mt. Lemmon daytime H_2O measures (dots) and Catalina (circles). Cf. Fig. 2
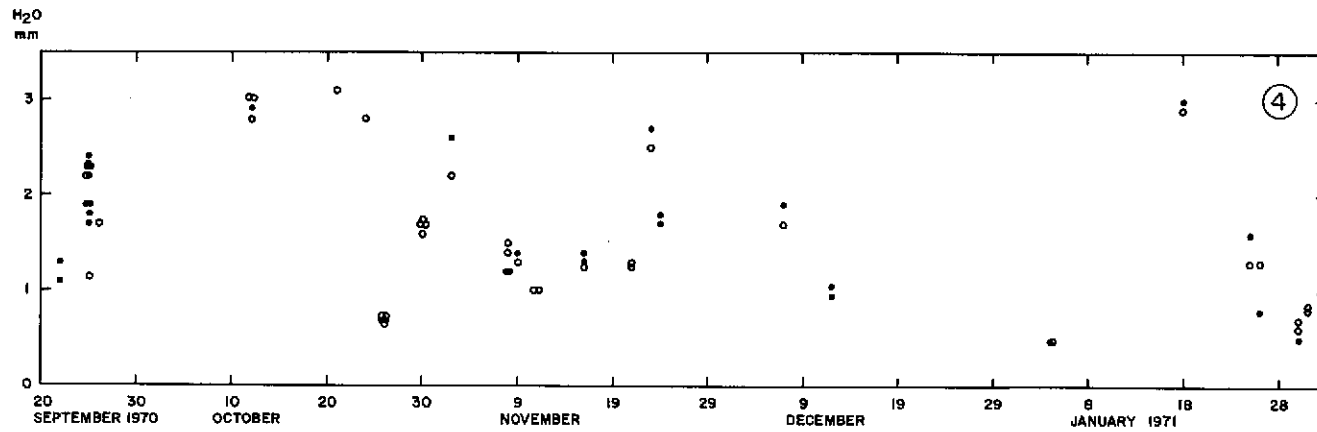
Figure 5 Tucson H$_2$O measures reduced to Mt. Lemmon. Cf. Figs. 1, 3
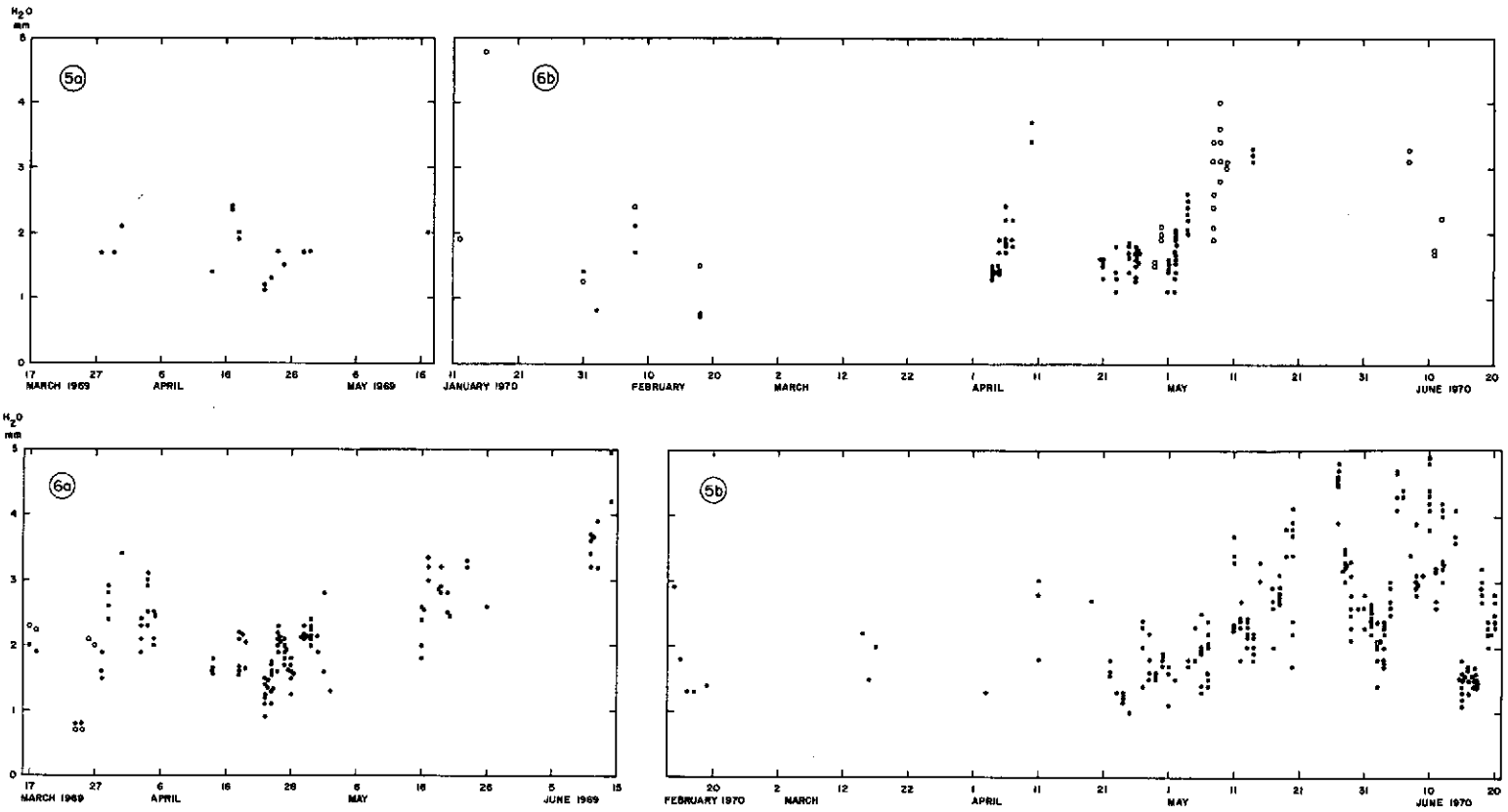
Figure 6 Mt. Lemmon daytime H$_2$O measures (dots) and Catalina (circles). Cf. Figs. 2, 4

The same scale height derived before, 2.27 km, was adopted in these reductions. (This scale height was derived *empirically* and thus compensates for minor scale errors).

Figure 1 shows the entries of the last column of Table I. Figure 2 combines the values of Tables II and III. The measures made in Tucson are nearly complete for all clear days during the interval, with the workload divided between the two authors. It is seen that measures were made on more than 90% of the days.

The figures show with unexpected clarity almost cyclic variations in the water-vapor content. These must be due to an alternation between air masses over Southern Arizona. The vertical spread of the dots for a given day is due in part to orographic effects. For this reason we average in Figure 7 the combined evidence of the Mt. Lemmon-Catalina data (Figs. 2, 4, 6) with the data derived in Tucson (Figs. 1, 3, 5), to obtain the day-to-day absorption variations.

Ideally, a graph similar to Figure 7 should be constructed showing the variation of the H_2O content over Mt. Lemmon based on the radio-sonde information (available on microfilms). Because of the considerable labor involved, we have limited here the comparison to the major minima and maxima. The correspondence between the two sets of data is quite good, with the minima and maxima readily identifiable in the microfilm records. The approximate levels below 1.5 mm were confirmed (for zenith objects the limit would be about 2.5 mm). For higher readings, we have corrected in Figure 7 the scale to correspond to the radio-sonde data.

3. Discussion

The data here presented are daytime measures. However, it has been our experience that the measured H_2O absorption in the solar beam on Mt. Lemmon is not minimal at noon (shortest airpath), but at 9 or 10 AM, and again around 3 PM. This appears due to the fact that the daytime solar exposure of the mountain causes updrafts which carry the higher H_2O mixing ratios from lower levels upward. Also, when the mountain is snow-covered (approx. 4-5 months of the year), the daytime evaporation causes the atmospheric boundary layer to contain more moisture than at night when the temperatures are lower. Nighttime observations have indicated that the water-vapor values sometimes drop down to 0.2-0.3 mm, a fact already suggested by the frequency curve of H_2O amounts above Mt. Lemmon published in *LPL Communication No. 156*, Fig. 25 (p. 363), and *No. 142*, Fig. 10 (p. 135). Even daytime values may be very low; we have witnessed solar observations at 20μ made with the University of Minnesota telescope, which found negligible extinctions for solar altitudes as low as 10-15°. A program is under consideration for regular nighttime observations using the 1.4μ H_2O band.

Attention is called to *LPL Communication No. 156* for the thermograph and relative-humidity records obtained at both the Mt. Lemmon and the Catalina Observatories for the period Oct. 26, 1970-Jan. 25, 1971, part of the interval covered by the integrated H_2O measures. It is seen that periods of very low relative humidity (5-20%) occur. In the radio-sonde data values of 14% (the lowest recordable value) are quite common at 700 mb and above.

The radio-sonde data also include the *wind direction* and *speed, temperature,* and *barometric pressure,* for all altitudes from 920-7 mb (Mt. Lemmon averages 720 mb). Correlation of these data with the occurrence of the maxima and minima
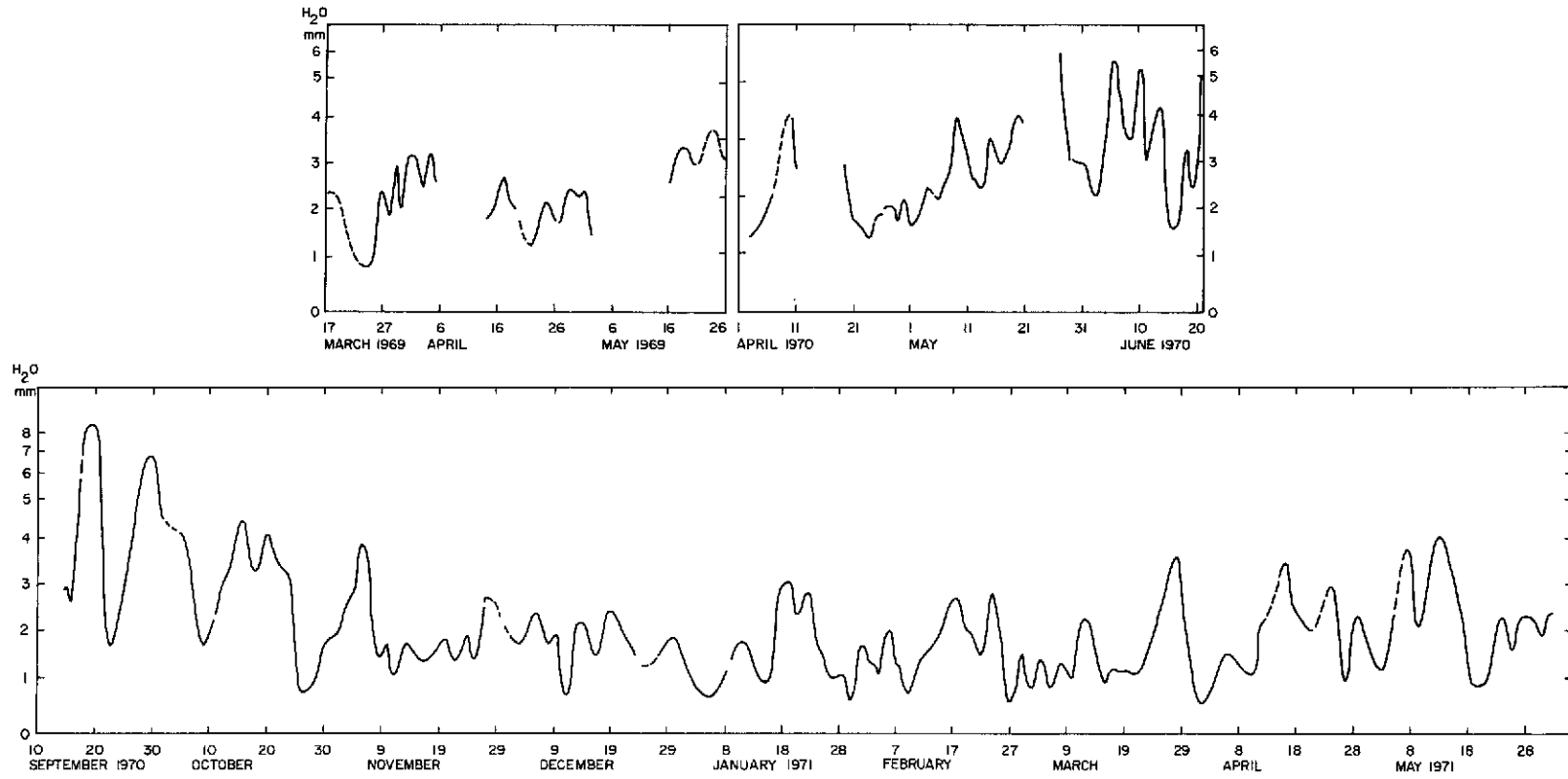
Figure 7 Combined results of daytime Mt. Lemmon H_2O data, with
ordinates adjusted to Tucson Airport radio-sonde data

in Figure 7 has led to the following preliminary conclusions: (a) the normal air
flow on Mt. Lemmon is from the West, so that the air mass is normally Pacific in
origin; (b) the exceptions are the period of the monsoon, mid- or late-June till
mid- or late-September, when more humid air masses move in from the Gulf of Mexico
(SE wind); the alternation shown in Figure 7, September 1970, is due to the de-
parting monsoon, with incursions of Pacific air causing drier periods.   Similar
alternations occur in June and sometimes throughout the Summer; (c) in mid-Winter
and Spring North-Continental air masses move in, causing at times periods of very
low humidity to follow snow falls; (d) the moisture content of the Pacific air
masses varies, depending on barometric pressure.   Barometric highs often persist
over the Continental Southwest, for one or more weeks at a time, throughout the
Fall, Winter, and Spring, which cause *subsidence of upper-atmospheric air* of low
moisture content (down to 3-15% relative humidity).   Samples of such air masses
were recorded during the same interval in *LPL Communication No. 156*, pp. 364-366.
Local subsidence, due to nighttime cooling of the summit, may cause a further
lowering of the humidity.   On the whole, however, the free-air values, measured
by radio-sonde, are good approximations of the actual conditions found over Mt.
Lemmon, an experience in common with a few other mountain sites similarly ex-
plored.   While most often the vertical H_2O profile of the atmosphere is quite
smooth and monotonic, exceptions (moist layers) do occur, so that surface humidity
data are no reliable substitute for integrated measures (solar beam or stellar
observations).

G. P. KUIPER AND L. RANDIC

TABLE I - Tucson, Space Sciences Bldg., 2510 ft (765 m), roof or surface(s)

Date	MST	H₂O(Sun)	H₂O(Zenith)	Mt.L.*
1971				
Jan 20	12:00	12.5	7.6	3.1
	13:56	12.8	7.2	2.9
	16:14	22.9	5.9	2.4
	17:10	29.3	2.8	1.1
23	10:50	10.8	5.9	2.4
	11:47	10.5	6.5	2.6
24	13:31	6.4	3.9	1.6
25	8:57	10.0	2.9	1.2
26	8:13	22.9	3.8	1.5
	12:45	5.5	3.5 s	1.5
27	9:26	6.5	2.4	1.0
	11:05	4.3	2.5	1.0
	13:37	4.0	2.4	1.0
	17:06	15.6	2.2	0.9
28	9:17	6.6	2.4	1.0
	10:45	4.7	2.6	1.1
	11:58	4.5	2.9	1.2
29	8:53	8.7	2.5	1.0
	11:00	4.9	2.8	1.1
	14:01	4.4	2.6	1.1
	15:57	7.3	2.5	1.0
	16:57	13.0	2.3	0.9
30	10:22	4.7	2.5	1.0
	11:55	3.6	2.3	0.9
31	9:43	5.7	2.4 s	1.0
Feb 1	9:08	9.1	3.1	1.3
	10:26	9.1	4.8	2.0
2	9:12	10.0	3.5	1.4
	11:05	6.0	3.6	1.5
	11:58	5.1	3.3	1.3
	15:18	6.9	3.2	1.3
3	9:05	14.6	5.0	2.0
	10:09	11.7	5.9	2.4
	14:23	5.7	3.3	1.3
4	9:03	5.2	1.8	0.7
	9:35	4.5	1.9	0.8
	15:46	6.1	2.5	1.0
	17:31	24.0	2.1	0.9
5	9:03	10.9	3.7	1.5
	11:13	6.5	4.1	1.7
	11:55	6.3	4.2	1.7
6	10:28	8.5	4.7	1.9
	11:51	7.1	4.7	1.9
	14:09	7.3	4.4	1.8
7	11:26	5.0	3.2 s	1.3
	12:23	4.4	2.9 s	1.2
	14:06	4.5	2.8 s	1.1
8	10:58	3.7	2.3	0.9
9	9:09	4.6	1.7	0.7
	11:08	3.1	1.9	0.8
	12:00	2.7	1.8	0.7
	14:54	3.2	1.7	0.7
	16:34	5.2	1.5	0.6
10	9:07	4.9	1.8	0.7
	10:38	3.3	1.9	0.8
	11:58	3.0	2.0	0.8
	14:05	3.4	2.1	0.9
	16:11	6.8	2.4	1.0
11	9:06	9.0	3.2	1.3
	11:16	4.6	3.0	1.2
	13:48	3.9	2.5	1.0
	15:52	6.2	2.6	1.1
12	9:17	7.4	3.1	1.3
	10:59	5.1	3.2	1.3
	12:02	5.0	3.5	1.4
	14:25	5.8	3.5	1.4
	17:03	15.3	3.1	1.3
13	10:30	6.1	3.6	1.5
	11:58	5.3	3.7	1.5
14	12:09	5.7	4.0	1.6
15	9:05	9.6	3.7	1.5
	10:11	7.0	3.8	1.5
	15:55	11.1	4.7	1.9
	16:58	17.7	4.1	1.7
16	9:18	10.6	4.5	1.8
17	11:57	7.7	5.5	2.2
	14:07	11.6	7.6	3.1
18	16:16	16.5	6.1	2.5
19	9:02	11.9	4.7	1.9
	11:55	5.7	4.1	1.7
	13:50	6.8	4.7	1.9
	16:54	14.1	3.6	1.5
21	13:02	5.8	4.2	1.7
22	9:17	6.7	3.0	1.2
23	9:15	8.7	3.9	1.6
	12:07	6.7	4.9	2.0
24	9:55	12.3	6.8	2.8
	15:39	12.6	6.3	2.6
25	12:05	6.8	5.1	2.1
26	10:00	5.4	3.1	1.3
	11:45	4.0	3.0	1.2
	15:59	5.5	2.4	1.0
27	11:33	1.9	1.4	0.6
28	10:10	3.5	2.1	0.9
	11:36	3.0	2.2	0.9
Mar 1	10:32	6.0	3.9	1.6
2	8:58	3.6	1.6	0.7
	9:01	3.3	1.4	0.6
	10:58	2.7	1.9	0.8
	11:59	2.7	2.1	0.9
	15:58	4.0	2.1	0.9
	17:24	10.3	2.0	0.8
1971				
Mar 3	9:38	3.7	2.0	0.8
	10:52	3.1	2.2	0.9
	12:10	2.6	2.0	0.8
	13:54	3.3	2.4	1.0
4	9:25	5.4	2.7	1.1
	10:51	4.1	2.9	1.2
	13:18	5.4	4.2	1.7
	15:18	6.4	3.7	1.5
	16:51	10.4	3.2	1.3
5	9:07	7.4	3.4	1.4
	10:34	5.3	3.6	1.5
	11:51	4.6	3.6	1.5
	13:55	4.4	3.2	1.3
	15:36	5.0	2.7	1.1
	16:49	5.5	1.8	0.7
6	9:34	3.6	2.0	0.8
	10:35	3.2	2.2	0.9
	11:46	2.6	2.0	0.8
7	12:10	3.4	2.7	1.1
8	8:57	5.9	2.7	1.1
	17:07	10.0	2.7	1.1
9	8:57	6.2	2.8	1.1
	11:36	3.7	2.9	1.2
10	8:58	4.9	2.3	0.9
	10:44	3.4	2.4	1.0
	15:01	4.4	2.8	1.1
	17:12	10.2	2.6	1.1
11	9:06	7.8	3.8	1.5
	10:50	6.3	4.6	1.9
	11:57	5.4	4.3	1.7
	14:06	6.7	5.0	2.0
12	8:59	9.7	4.6	1.9
	13:05	6.6	5.3	2.2
	15:09	7.7	4.8	2.0
	16:54	14.1	4.6	1.9
13	10:20	6.9	4.7	1.9
	12:37	6.4	5.2	2.1
14	11:50	4.4	3.5	1.4
15	9:16	5.9	3.2	1.3
	11:58	3.7	3.0	1.2
	12:55	3.6	3.0	1.2
17	17:06	7.2	2.1	0.9
18	9:06	5.2	2.7	1.1
	10:49	3.7	2.8	1.1
	11:55	3.4	2.8	1.1
	14:49	3.4	2.3 s	1.0
19	13:28	3.5	2.8	1.1
20	9:32	4.7	2.8	1.1
	10:42	3.3	2.5	1.0
	12:32	3.3	2.8	1.1
21	8:26	5.2	2.1	0.9
	16:02	3.8	1.9 s	0.8
22	9:38	4.0	2.5	1.0
	10:22	3.6	2.6	1.1
	17:23	9.4	2.3	0.9
23	10:39	4.8	4.8	1.5
26	9:44	9.2	6.1	2.5
	11:54	7.3 s	6.3	2.6
	14:11	8.2	6.4	2.6
	16:56	15.5	5.5	2.2
27	10:44	8.7	6.9	2.8
	14:30	10.9	8.2	3.3
29	9:35	6.2 s	4.1	1.7
	17:22	16.8	4.5	1.8
30	17:08	13.2	4.2 s	1.7
31	17:21	11.2	3.1	1.3
Apr 1	8:58	2.0	1.1	0.4
	10:23	1.5	1.1 s	0.5
	12:15	1.7	1.5	0.6
	13:48	1.7	1.4	0.6
	15:29	1.9	1.2	0.5
2	9:00	2.3	1.3	0.5
	11:18	1.7	1.4	0.6
	13:16	1.7	1.5	0.6
	17:06	4.1	1.4	0.6
3	10:13	1.9	1.4	0.6
	11:36	1.7	1.5	0.6
4	13:30	3.2	2.8	1.1
	16:38	5.2	2.3	0.9
5	9:04	4.7	2.8	1.1
	10:57	5.4	4.5	1.8
	17:01	7.1 s	2.6	1.1
6	9:05	5.7	3.4	1.4
	11:30	4.2	3.7	1.5
	13:23	4.6	4.0	1.6
	14:56	5.6	4.0 s	1.68
7	17:12	7.3	2.4	1.0
8	8:59	4.1	2.4	1.0
	11:41	3.4	3.0	1.4
	14:12	4.7	3.8	1.5
	16:52	7.9	3.1	1.3
9	14:03	3.6	3.0	1.2
10	10:53	3.1	2.6	1.1
	11:16	2.7	2.4	1.0
11	10:19	3.6	2.0 s	0.9
	12:01	2.3	2.1	0.9
	16:20	5.1 s	2.6 s	1.1
12	10:17	4.9	3.9	1.6
	16:37	12.6	5.7	2.3
13	9:01	5.7	3.5	1.4
	11:52	3.8	3.5	1.4
	14:22	4.5	3.6	1.5
	17:00	10.3	3.9	1.6
1971				
Apr 15	15:42	11.1	7.0	2.8
16	9:01	13.4	8.4	3.4
	12:36	10.2	9.4	3.8
	17:49	27.1	5.7	2.3
17	10:12	8.8	7.1	2.9
19	9:36	7.2	5.2	2.1
	10:30	6.8	5.7	2.3
20	9:17	6.4	4.4	1.8
	10:41	5.3	4.5	1.8
24	9:10	7.7	5.2	2.1
	11:28	7.5	6.9	2.8
25	12:45	5.5	5.2	2.1
	14:46	7.7	6.1	2.5
26	9:02	6.4	4.2	1.7
	10:09	4.9	4.0	1.6
27	9:08	5.0	3.4	1.4
	11:33	3.7	3.4 s	1.4
	14:05	5.3	4.6	1.9
	16:07	6.4	3.7	1.5
28	8:59	6.7	4.4	1.8
	11:07	6.6	6.0	2.4
	12:44	6.2	5.9	2.4
	17:04	12.7	5.1	2.1
29	8:57	7.4	4.8	2.0
	10:57	5.4	4.9	2.0
	14:03	6.0	5.2	2.1
	16:38	9.0	4.4	1.8
30	9:00	5.4	3.6	1.5
	10:59	3.5	3.2	1.3
	13:45	3.5	3.1	1.3
May 1	10:11	3.8	3.2	1.3
	13:27	3.6	3.3	1.3
	15:24	6.0	4.2	1.7
	17:01	7.9	3.3	1.3
2	11:06	3.1	2.8	1.1
	17:31	7.7	2.5	1.0
3	9:01	3.6	2.4	1.0
	10:29	2.8	2.4	1.0
	18:04	10.2	2.1	0.9
4	9:00	5.7	3.9	1.6
	11:47	5.3	5.0 s	2.0
	16:51	8.0	3.6	1.5
5	9:11	7.4	5.2	2.1
	11:19	6.4	6.0	2.4
	13:23	5.8	5.4	2.2
	17:58	22.3	5.1	2.1
7	11:34	9.8	9.3	3.8
8	15:26	10.4	7.5	3.0
9	11:27	7.1	6.8	2.8
10	9:35	7.3	5.7	2.3
	10:14	7.1 s	6.1	2.5
	17:21	13.9	5.0	2.0
11	8:59	7.1	4.8	2.0
	11:44	7.5	7.2	2.9
	15:39	9.0	6.1	2.5
13	9:00	12.7	8.8	3.6
	11:22	9.4	8.9	3.3
	14:29	9.5	8.0	3.3
14	15:33	10.4	7.2	2.9
15	9:40	7.9	6.2	2.5
	12:39	7.9	7.6 s	3.1
16	16:19	8.5	4.9	2.0
17	9:07	8.4	5.3	2.2
	10:14	7.1	6.1	2.5
18	9:11	2.9	2.1	0.9
	11:05	2.5	2.3	0.9
	13:06	2.4	2.3	0.9
	17:04	4.2	1.8	0.7
19	9:03	3.0	2.1	0.9
	12:01	2.1	2.0	0.8
	14:55	2.7	2.1 s	0.9
	17:17	5.4	2.1	0.9
20	9:27	2.7	2.1	0.9
	11:44	2.1	2.0	0.8
	14:40	2.8	2.3	0.9
22	11:06	4.9	4.6	1.9
23	11:00	5.5 s	5.1	2.1
24	9:11	6.7	4.9	1.9
	10:18	5.1	4.4 s	1.8
25	9:00	5.8 s	4.1	1.7
26	9:02	6.9	4.9	2.0
	10:59	4.8	4.5	1.8
	15:01	4.2	3.3	1.3
	17:30	9.0	3.2	1.3
27	9:07	7.1	5.1	2.1
	11:31	5.1	4.9	2.0
	14:35	8.0	6.7	2.7
28	9:27	6.5	5.0	2.0
	12:41	5.2	5.1	2.1
	15:55	4.8	3.2	1.3
29	9:52	5.9	4.9	2.0
	15:15	8.0	6.2	2.5
31	9:13	6.1	4.5	1.8
	10:36	5.2	4.7	1.9
Jun 1	12:59	6.6	6.5	2.6
	14:34	5.8	4.9	2.0
	16:22	4.6	2.1	1.1
3	8:29	7.4	4.6	1.9

* Computed from preceding column with known average scale height.

TABLE II - Mt. Lemmon Solar Obs. 9100 ft (2770 m)

Date	MST	H_2O(Sun)	H_2O(Zenith)
1971			
Feb 1	14:40	3.7	2.0
4	12:53	1.8	1.2
	12:59	1.8	1.2
8	15:00	1.8	0.95
15	13:30	3.3	2.3
Mar 7	16:56	4.6	1.4
8	14:25	2.2	1.55
15	15:35	1.4	0.8
	16:23	1.7	0.7
16	9:47	1.2	0.7
	11:54	1.3	1.05
	12:42	1.4	1.15
	12:47	1.4	1.15
	13:31	1.6	1.3
	14:44	1.8	1.2
	16:00	2.3	1.1
	16:41	2.9	1.1
21	10:31	1.6	1.2
	11:40	1.5	1.2
	12:39	1.4	1.2
	13:52	1.3	1.0
22	14:31	1.7	1.3
23	13:14	2.9	2.4
	16:00	1.8	0.9
	17:34	5.6	1.2
28	11:13	4.6	3.8
	14:15	2.8	2.2
	17:09	3.5	1.1
29	13:50	2.6	2.1
30	10:10	3.3	2.4
	11:33	3.8	3.25
	12:34	3.2	2.8
	13:37	2.7	2.25
Apr 5	14:40	1.7	1.3
7	14:56	1.9	1.4
9	11:40	1.1	1.0
10	14:23	1.3	1.0
	15:26	1.5	1.0
12	14:05	3.0	2.5
17	15:11	2.6	1.9
	15:50	3.7	2.3
26	14:25	1.1	0.9
May 3	14:35	1.9	1.6
9	15:26	2.5	1.8
	16:18	2.8	1.6
10	14:25	3.6	3.1
22	12:57	0.8	0.8
	14:23	1.8	1.55
24	14:25	2.8	2.4
31	15:30	2.45	1.8

Table III - Catalina Observatory, Site I (8270 ft - 2520 m)

Date	MST	H_2O(Sun)	H_2O(Zenith)	Mt.Lemmon*
1971				
Feb 1	13:15	3.5	2.3	2.0
4	11:45	1.9	1.2	1.1
	12:13	2.1	1.4	1.25
	13:29	2.2	1.4	1.25
8	13:50	2.0	1.3	1.15
13	14:45	3.6	2.1	1.9
15	12:17	2.8	2.0	1.8
27	13:41	1.1	0.8	0.7
	15:46	1.3	0.6	0.53
28	13:53	1.3	0.9	0.8
	17:05	3.9	1.0	0.9
Mar 8	12:55	1.9	1.5	1.35
22	12:50	2.0	1.7	1.5
29	12:07	1.8	1.6	1.4
Apr 3	14:58	1.6	1.1	1.0
	16:16	1.7	0.85	0.75
4	11:20	1.7	1.5	1.35
5	13:20	2.3	2.0	1.8
10	17:00	3.0	1.15	1.0
12	12:45	2.7	2.5	2.2
24	15:25	4.7	3.3	2.9
26	12:08	1.0	0.95	0.85
May 3	13:15	1.75	1.6	1.4
17	12:35	3.2	3.1	2.75
24	12:25	2.5	2.45	2.2
31	13:45	2.0	1.9	1.7

* Computed from preceding column with known average scale height.

NO. 194   ECCENTRICITY AND INCLINATION OF MIRANDA'S ORBIT

by Ewen Whitaker and Richard Greenberg

August 29, 1973

ABSTRACT

Careful re-measurement of all available plates showing Uranus V (Miranda), supplemented by some recently obtained images, shows that this satellite has both a pronounced orbital eccentricity and inclination (to the plane of the other satellites). Observations are sufficient in number and distribution to allow determinations of the precession rates of both pericenter and node, with implications for the dynamical oblateness of Uranus and the gravitational interaction of the satellites. An improved value for the revolution period is a by-product of the investigation. The success of this study is due to the improved precision of the measures resulting from the adoption of a very simple, direct method of measurement.

1. Introduction

Uranus' satellites Miranda, Ariel, and Umbriel display a near-commensurability of mean motions which may be expressed in the form $n_M - 3n_A + 2n_U \simeq 0$. Since an identical relation holds exactly for three Galilean satellites of Jupiter, it is reasonable to suspect that such relations are not due to chance alone, but that they contain information about satellite evolution.

Such consequences motivated an investigation into the remote possibility that the commensurability in the Uranus system appears inexact due to some error in the determination of Miranda's orbital period. We first consulted Van Biesbroeck's (1965) calculations which, apart from two plates taken in the mid-1950's, were based on plates obtained during the 1948-49, 1960, 1961, and 1962 oppositions of Uranus. On checking these figures it soon became apparent that several errors and inconsistencies were present; it was then recalled that at that time, the calculator used for the reductions had a mechanical fault which was not detected until a year or two later. Since the addition of one revolution in the years between these epochs would lower the orbital period from the accepted value of 1.4135 days to the commensurate value 1.4130 days, we decided to repeat Van Biesbroeck's investigation, including a quick check of the position angles of Miranda relative to Uranus. Sections 4 *et seq.* describe how this led to the detection and evaluation of orbital parameters which were previously unresolved.

2. Observations

Following the discovery of Miranda in 1948 by Kuiper (1949), an intensive program of observations was pursued for about one year by Harris (1949) and Kuiper, who obtained about 70 measurable plates with the 82-inch reflector, McDonald Observatory, Texas. Using the same telescope, a few further plates were secured in 1954 and 1955 by Kuiper, and larger numbers in 1960 and 1961 by Kuiper and Whitaker, and in 1962 and 1964 by Van Biesbroeck and Whitaker. Van Biesbroeck also obtained a series of plates with the 61-inch reflector, Catalina Observatory during the 1966 opposition of Uranus, at which epoch the satellite orbits were presented edge-on. Unfortunately, none of these plates contained an image of Miranda.

More recently, Sinton (1972) published a photograph of Miranda taken with the 88-inch reflector, University of Hawaii, using only the light of a methane absorption band. During the 1973 opposition, Whitaker obtained images of Miranda with the 61-inch telescope while testing a special camera which is based on an adaptation of the coronagraph principle. The image of the planetary disk is first occulted by a circular opaque stop; a lens at this location produces an intermediate image of the mirror system, at which point an appropriately-shaped mask occults all planetary light diffracted by the mirror edges, retaining clips and lugs, and the secondary mirror support vanes. Another lens re-images the sky. Figure 1 illustrates a typical image obtained with this camera; because of mediocre seeing, some light from Uranus by-passed the planet stop.

3. Previous Analyses

The 1948-49 group of plates was first measured by Harris (1949) using a standard astrometric measuring machine. He employed normal astrometric reduction techniques, utilizing comparison stars and the other satellites for scale, orientation, and position. The images of Uranus were not measured because of their large

size. He obtained improved elements for the four major satellites, and obtained results for Miranda which may be expressed as follows:

P   (orbital period)   1.413487 ± .000007 days
U_O (mean longitude at epoch) $105°.8 ± 0°.8$
e   (eccentricity)   <0.01 (not detected)

where the epoch is 1950.0 (J.D. 2433282.0), and longitude is measured from the ascending node of Miranda's orbit on Uranus' orbit.

Van Biesbroeck (1965) measured 19 plates selected from the 1948-1962 period, giving estimates of the position angle of Miranda relative to Uranus. From these he obtained a value of 1.41347 days for the period, but this result is not valid because of errors introduced by the faulty calculator as already noted.

Van Biesbroeck (1970) re-measured a comprehensive selection of plates taken from 1948 through 1966, once again using standard astrometric techniques, and gave results in the form of differential coordinates from Titania (in arc-sec). Astrometric coordinates (α and δ) for Titania were also given. On the basis of these and other measures, Dunham (1971) published the results of an exhaustive analysis of the motions of Uranus' satellites. His results for Miranda may be expressed as follows:

P   1.4134840 ± .0000003 days
U_O $105°.0 ± 0°.3$
e   < 0.01 (not detected)

with no other elements detected.

4. Method of Re-measurement

In order to make a quick check of the position angles of Miranda on the 19 plates tabulated by Van Biesbroeck (1965), Whitaker employed the simple expedient of a surplus glass reticle, originally intended for use in a finder telescope, which was marked $0°-360°$ by 5° increments. Each plate (Fig. 2 shows a typical good-quality image) was first carefully positioned over a pair of thin, orthogonal black lines drawn on tracing plastic placed on a light box. The diffraction cross on each image of Uranus, which is oriented at exactly 45° to true North for the 82-inch reflector, permitted remarkably accurate and reproducible orientation and positioning of each plate (Fig. 3). The reticle was placed symmetrically over the Uranus image-plus-lines and rotated until one of its four cardinal lines bisected the image of Miranda. The position angle was then read directly to the nearest degree by visual interpolation (Fig. 4). Because of the thickness of the diffraction bars, and the fuzzy appearance of many Miranda images, a 3x achromatic lens was found to be optimum for viewing. Measures were repeated with the plates held at various orientations to eliminate possible bias due to personal error. After a little practice, measures for good images were repeatable to ±1° probable error or better, and those of fuzzy images to ± 2° p.e.
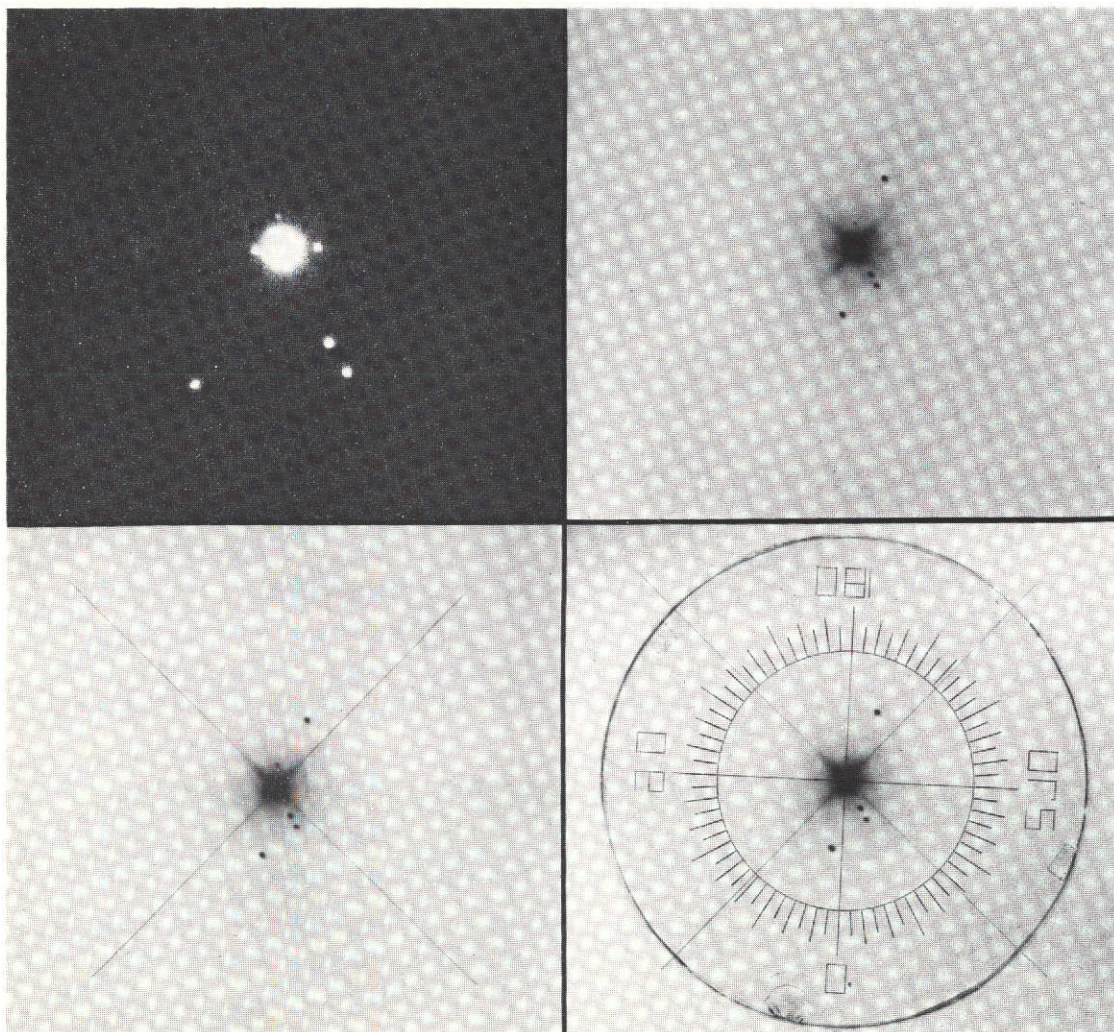
Figure 1   Uranus satellite system as photographed by special camera on the
           61-inch reflector, 1973 June 9d 04h 54m U.T.   South is up.   Lower
           image at left is a star.

Figure 2   Typical good-quality image ("1" in Table I) of Uranus and satel-
           lites from collection of 82-inch plates (CC 544, 1961 Apr 5d 04h
           46m U.T.).   South is up.   See Figure 4 for scale.

Figure 3   Same plate positioned over orthogonal cross.

Figure 4   Same combination of plate plus cross, with the 1-inch diameter
           reticle almost in correct position.   True p.a. = 178°.

5. Reduction of Measures

The new measures were initially reduced exactly as in Van Biesbroeck's Table 1 (1965), using the American Ephemeris tabulations to obtain the epoch of the nearest greatest southern elongation. This gave noticeably smaller residuals, and confirmed Harris' value for the period. However, we realized that the reduction was basically incorrect, since the greatest southern elongation as defined in the American Ephemeris is not a fixed point on the orbit. Furthermore, greatest southern elongation and position angle 180° are not the same point, as stated by Van Biesbroeck (1965, p. 7). Although we had shown to our satisfaction that the period of Miranda was not exactly commensurate with those of Ariel and Umbriel, we decided to investigate matters a little further to see whether the 12.3 year circulation period for contemporaneous conjunctions of these three satellites might not cause some periodic variations in Miranda's period.

6. Further Measurements

In order to obtain better accuracy, we decided to measure all available plates, using the quick and simple method already described. On nights when a large number of images were obtained, one or two of the poorer images were omitted. For the six images obtained in 1972-73, the zero of position angle was determined by calculation of the positions of Titania and Oberon from the American Ephemeris tabulations. Ariel and Umbriel were not used because of systematic divergences from the tabulated positions in each case. Table I lists all plates and images used in the final analysis; the criterion used for retention or rejection is explained in the next Section.

7. Further Reductions

Once again, the general method used by Van Biesbroeck (1965) was employed, except that the datum longitude was taken as Miranda's ascending node on Uranus' orbital plane. The time of next arrival at this longitude was computed from the position angle of each observation, assuming circular motion in Uranus' equatorial[*] plane and an orbital period of 1.41349 days. These results were compared with the arrival times calculated as integer multiples of 1.41349 days.

It was at once obvious from the run of the residuals that the chosen period was too long. The residuals for 1972-73 observations, compared with the earlier observations, indicated a period nearer 1.41348 days. Furthermore, on plotting the residuals against position in orbit (Figs. 5 and 6), it was clear that systematic trends were present. In particular, the points defined a convincing sinusoid, although the scatter about this curve was still larger than could be accounted for by measuring errors alone. However, when only residuals from 1948-49 were plotted (Fig. 5), the scatter was significantly reduced. We interpreted this sinusoid as representing Miranda's orbital eccentricity for the following reasons: during the 1948-49 epoch the orbit was viewed nearly pole-on so that the residuals would be relatively insensitive to any error in the plane of the orbit, whereas

---

[*] Assumed throughout this paper to be coplanar with the orbits of Ariel and Umbriel.

TABLE 1

Measures and Residuals

Plate or Image	Time U.T.	Image Quality	Observed Position Angle°	Residual O-C p.a.°	Plate or Image	Time U.T.	Image Quality	Observed Position Angle°	Residual O-C p.a.°
McD, 82"					McD, 82"				
1	1948 Feb 15, 2ʰ55ᵐ	4	327	-0.9	238	1954 Jan 29, 7 00	3	15	+2.0
9	" Mar 1, 2 38	2	108	-2.2	274	1955 Jan 28, 7 40	2	182	-1.2
10	" Mar 1, 2 46	1	107	-1.9	276	" Jan 28, 7 45	2	182	-0.4
11	" Mar 24, 2 00	2	21	+0.4	464	1960 Apr 15, 3 24	4	215	+1.5
12	" Mar 24, 2 08	1	18	-1.6	465	" Apr 15, 3 28	4	213	+0.2
21	" Mar 24, 3 32	3	3	-0.3	467	" Apr 15, 3 40	4	213	+1.5
22	" Mar 24, 3 46	2	0	-1.2	468	" Apr 15, 4 22	1	208	+1.0
					469	" Apr 15, 4,28	2	206	-0.3
31	" Mar 25, 2 30	3	118	-0.2	470	" Apr 15, 4 56	1	204	0
32	" Mar 25, 2 37	3	117	-0.2	471	" Apr 15, 5 02	1	203	-0.5
33	" Mar 25, 2 42	3	115	-1.2	472	" Apr 15, 6 11	2	196	-0.9
34	" Mar 25, 2 47	1	114	-1.3					
					474	" Apr 16, 2 19	1	358	-1.4
43	" Oct 19, 9 58	3	348	+2.0	475	" Apr 16, 2 24	1	358	-0.8
44	" Oct 19,10 03	3	345	+0.2	476	" Apr 16, 2 33	1	357	-1.2
45	" Oct 19,10 09	3	345	+0.2	479	" Apr 16, 2 55	1	356	+0.5
					480	" Apr 16, 3 09	1	355	+0.8
46	" Oct 21,10 50	3	185	+0.8	481	" Apr 16, 3 14	1	354	+0.6
47	" Oct 21,10 55	3	183	-0.2	482	" Apr 16, 4 13	3	347	+1.7
48	" Oct 24, 8 25	2	163	-2.8	539	1961 Apr 5, 3 42	3	183	-1.2
49	" Oct 24,11 31	4	132	-1.4	540	" Apr 5, 3 47	3	182	-1.7
50	" Oct 24,11 45	4	133	+0.5	541	" Apr 5, 3 52	3	182	-1.4
52	" Oct 24,12 00	4	130	+0.7	542	" Apr 5, 3 57	3	182	-1.2
					543	" Apr 5, 4 37	1	178	-1.3
53	" Oct 25, 8 30	2	273	-0.1	544	" Apr 5, 4 46	1	178	-0.2
54	" Oct 25, 8 50	1	271	+1.0					
55	" Oct 25, 8 56	2	268	-0.7	546	" Apr 7, 5 24	2	9	-1.6
56	" Oct 25, 9 06	3	267	+0.5	547	" Apr 7, 5 31	1	9	-1.1
57	" Oct 25, 9 12	3	265	-0.5	549	" Apr 7, 5 45	3	8	-0.7
58	" Oct 25,10 08	2	256	+0.6					
59	" Oct 25,10 14	2	255	+0.7	550	1962 Mar 27, 6 37	1	193	+0.3
60	" Oct 25,10 24	1	253	+0.8	551	" Mar 27, 6 42	1	192	-0.3
61	" Oct 25,10 30	3	252	+0.9	552	" Mar 27, 6,47	1	192	+0.1
62	" Oct 25,11 16	1	243	+1.0	553	" Mar 27, 6 51	1	192	+0.5
63	" Oct 25,11 22	3	242	+1.1	554	" Mar 27, 7 14	2	191	+0.7
					555	" Mar 27, 7 18	1	190	+0.1
73	" Oct 26,10 06	2	364	+2.0	556	" Mar 27, 7 21	2	190	+0.5
74	" Oct 26,10 12	2	363	+2.0	557	" Mar 27, 7 45	2	188	-0.2
77a	" Oct 26,11 30	3	347	-0.2	558	" Mar 27, 7 50	1	188	+0.2
78	" Oct 26,11 40	1	345	-0.2	559	" Mar 27, 7 53	2	187	-0.4
79	" Oct 26,11 48	2	344	-0.1					
80	" Oct 26,11 55	1	342	-0.9	573	" Mar 29, 7 03	3	25	+0.2
					574	" Mar 29, 7 07	2	24	-0.3
91b	" Oct 27,11 16	2	93	-1.3	575	" Mar 29, 7 11	2	24	+0.2
92a	" Oct 27,11 22	2	92	-1.4	576	" Mar 29, 7 15	3	24	+0.5
93a	" Oct 27,11 42	2	92	+1.6	577	" Mar 29, 7 18	2	23	-0.4
94a	" Oct 31, 9 44	2	170	+0.8	591	" Apr 25, 3 42	3	25	+0.3
95a	" Oct 31,10 18	2	164	+1.0	592	" Apr 25, 3 47	1	25	+0.7
95c	" Oct 31,10 34	2	162	+2.0	593	" Apr 25, 3 56	1	25	+1.2
96a	" Oct 31,11 01	2	157	+1.2	594	" Apr 25, 4 01	1	24	+0.8
97a	" Oct 31,11 25	3	151	-0.7					
					664a	1964 May 30, 3 08	2	34	-0.2
98a	" Nov 6, 8 08	2	98	-2.3	665a	" May 30, 3 16	2	34	+0.5
99b	" Nov 6, 8 59	2	90	-1.0	666a	" May 30, 3 22	2	34	+1.1
100b	" Nov 6, 9 49	2	82	-0.8					
101a	" Nov 6,10 34	3	73	-1.3	667b	" Jun 2, 3 04	3	18	+0.5
102a	" Nov 6,10 51	4	72	+0.7	668b	" Jun 2, 3 10	1	18	+0.8
102b	" Nov 6,10 59	4	72	+1.7	669a	" Jun 2, 3 14	1	17	0
103a	" Nov 6,11 07	4	70	+0.7	670h	" Jun 2, 3 25	1	17	+0.6
103b	" Nov 6,11 15	4	68	+1.0	671a	" Jun 2, 3 29	1	17	+0.8
					672a	" Jun 2, 3 37	1	17	+1.1
104a	" Nov 7, 8 34	2	197	0					
104b	" Nov 7, 8 41	2	196	0	Sinton				
104c	" Nov 7, 8 48	2	195	0	88" H.	1972 Mar 17, 10 37	2	7	+0.2
107b	" Nov 8,10 03	3	292	-0.2	61" Catalina				
108a	" Nov 8,10 10	3	288	-0.8	W1	1973 May 8, 7 06	2	345	+0.7
108b	" Nov 8,10 17	3	288	+0.2	W2	" May 9, 5 14	1	200	0
					W3	" May 28, 4 33	3	3	-1.0
109a	" Nov 10, 7 36	3	163	-0.6					
111b	" Nov 10, 8 11	3	158	+0.6	W4	" Jun 9, 4 54	1	185	+1.0
					W5	" Jun 9, 5 15	1	186	+0.1
119a	" Nov 11, 8 44	3	261	+1.1					
120	1949 Feb 24, 1 53	4	228	-1.7					
122	" Feb 24, 2,09	4	226	-1.6					
124	" Feb 24, 3 51	4	208	+0.3					
125	" Feb 24, 4 00	2	207	+0.3					
126	" Feb 24, 4 07	2	207	+1.4					

McDonald 82-inch, CC series; Catalina 61-inch W(hitaker) series

Image Quality:

1. Sharp, small, or circular
2. Fuzzy, large, or asymmetrical
3. Very faint
4. In or touching diffraction ray or planetary halo

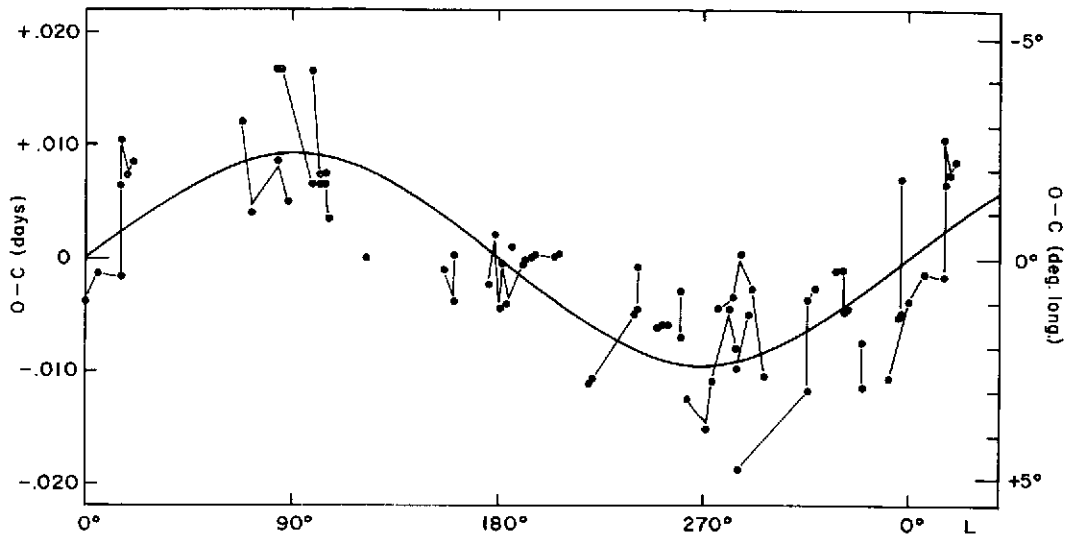|				
145a	" Feb 27, 1 51	3	184	-1.2
146b	" Feb 27, 2 32	2	176	-1.8
146d	" Feb 27, 2 48	2	174	-0.7
147a	" Feb 27, 3 47	3	165	+0.9
147c	" Feb 27, 4 00	2	162	-0.1

Figure 5 Plot of deviations from circular motion against
position in orbit (L, longitude) for 1948-49(approx. pole-
on) observations. Results from a single night are joined.
The curve represents eccentricity e = 0.02

later residuals would be expected to reflect such orbital inclination because the
Earth crossed the Uranus equator in 1966. We estimated the eccentricity to be
about 0.02, with the pericenter at 180° longitude.

The scatter in the post-1949 residuals could then be considerably reduced if
Miranda's orbit was assumed to be inclined to Uranus' equator by about 7°, with
its ascending node 90° from the datum longitude. However, this orbit was rejected
for two reasons. First, the residuals were still too large to be accounted for by
measuring errors. Second, the oblateness of the planet, with $J_2 \simeq 0.012$ (Dunham
1971), would cause precession of both the apse and the node with periods on the
order of 6 years (see Section 8). Thus, a model which neglects precession would
not be satisfactory. It was suspected at this point in our investigation that
the surprisingly good fit of a fixed inclined orbit was due to the fact that the
bulk of the observations were made in three groups at intervals of 12 years, there-
by obscuring any 6-year precession.

We next computed the change in each residual as a function of orientation of
the orbital plane. With this information we were able to obtain by graphical
methods estimates of precession rates and of a plane orientation at epoch which
reduced the residuals to acceptable levels. The following list of orbital para-
meters summarizes our estimate:

P	(orbital period)	1.413480 to 1.413483 days
U_0	(mean longitude at epoch)	107°
e	(eccentricity)	0.02
$\tilde{\omega}_0$	(Longitude of pericenter at epoch)	210°
P_a	(apsidal precession period)	14.6 to 15.1 yr. (direct)
i	(inclination to Uranus' equator)	3.5° to 4.5°
Ω	(longitude of ascending node on Uranus' equator at epoch)	137°
P_n	(nodal precession period)	14.6 to 17.2 yr. (retrograde)

The epoch for U_0 and $\tilde{\omega}_0$ is taken as 1950.0 (J.E.D. 2433282.0); for Ω it is taken as 1962.0, a date which was much closer to edge-on apparition of the orbit and thus allowed a more precise estimate of Ω. Longitudes are measured from the ascending node of Miranda's orbit on Uranus' orbit.

Using the IBM 1130B computer, Greenberg devised and executed a program that adjusted the eight parameters to obtain the least squares of the observed-minus-calculated values of the position angles. The observations were weighted on a 1 or 0 basis: measurements of 133 good images of Miranda were weighted equally, while eight measurements of poor images were disregarded. Images were considered poor if they were pear-shaped due to poor guiding or mirror distortion, if they were of dubious identity or if the positions of the other satellites indicates gross clock errors. The residuals for these poor images were unacceptably large.

Miranda's orbital plane was assumed to precess relative to the equator of the planet. That equator's inclination and node longitude, referred to the Earth's equator and equinox of 1950.0, were taken as 74°.96 and 166°.72 respectively (Dunham 1971). The direction of Uranus relative to the Earth, at the instant of each observation, was calculated from the orbital elements of the two planets given in the Explanatory Supplement (1961).
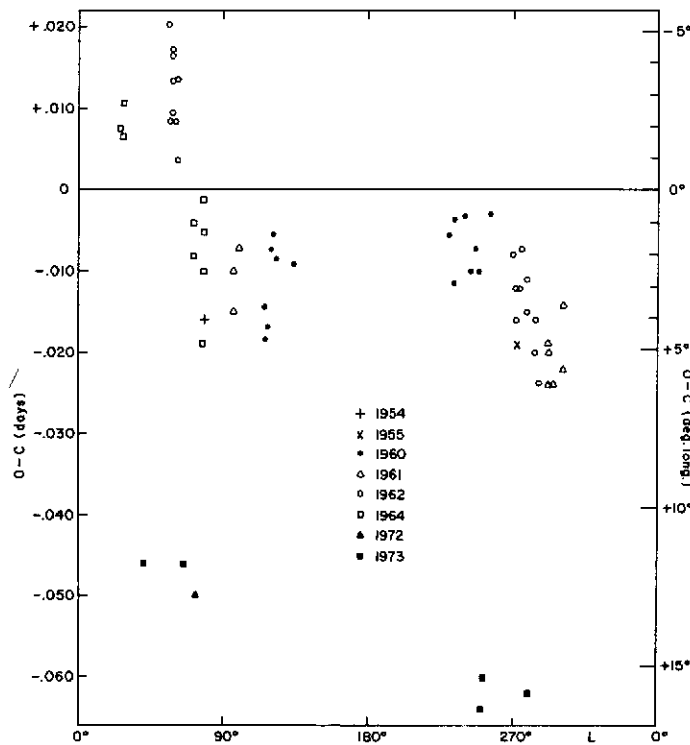
Figure 6 Plot of deviations from circular motion with P = 1.41349 days against position in orbit for 1954-1973 observations

The following parameters (shown with their probable errors) give the best fit:

P	(orbital period)	1.4134823 ± .0000005 days
U_o	(mean longitude at epoch)	$106°.48 ± 0°.07$
e	(eccentricity)	0.017 ± .001
$\tilde{\omega}_o$	(longitude of pericenter at epoch)	199° ± 2°
P_a	(apsidal precession period)	14.2 ± .2 yr. (direct)
i	(inclination to Uranus' assumed equator)	$3°.36 ± 0°.26$
Ω	(longitude of ascending node on Uranus' equator at epoch)	$136.4 ± 3°.4$
P_n	(nodal precession period)	15.8 ± .5 yr. (retrograde)

with symbols and epochs as given for the graphical solution. Reducing Ω to epoch 1950.0 for uniformity gives $\Omega_o = 49°.6 ± 10°.6$.

With these parameters, the root mean square of the residuals in position angle is ±1°, in agreement with our *a priori* estimate of the measurement precision. Figure 7 gives a plot of these residuals against date.

8. Discussion

A. Measuring technique

The apparent lack of sensitivity of previous measurements to Miranda's eccentricity and inclination can be attributed largely to the relatively high magnification of standard astrometric measuring machines (typically 20x). At that power, many of the images of Miranda appear as scarcely discernible fuzz-balls, and bisection of the Uranus image is impossible. Thus orbital computations have to be made indirectly from the positions of the other satellites. A second factor is the relatively large scale (7.4 arc-sec/mm) at the Cassegrain focus of the 82-inch, which causes a paucity of field stars and hence unreliable scale and orientation determinations.
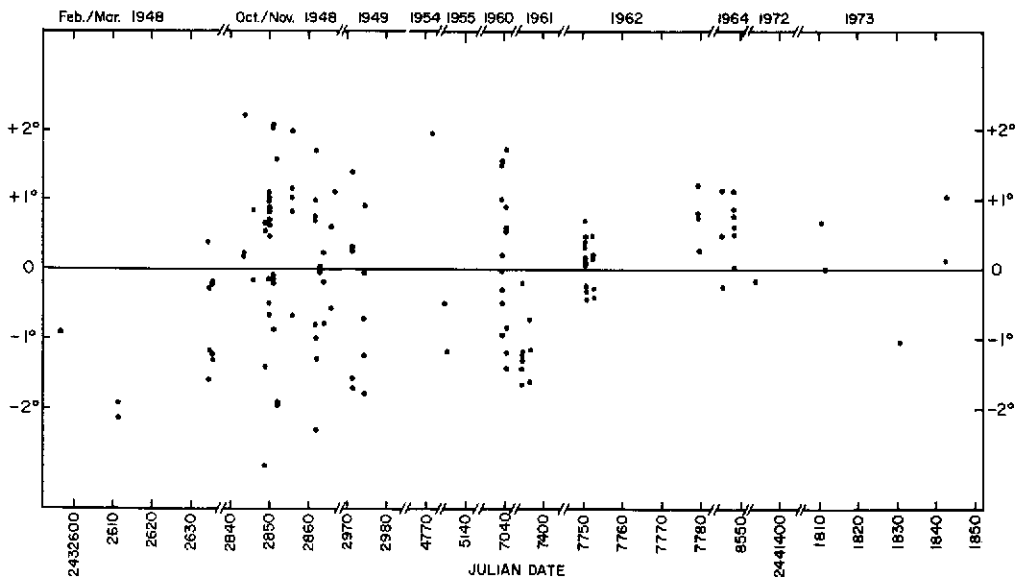
Figure 7 Plot of final O-C residuals in position angle against date

It is apparent that the combined errors arising from these causes are large enough to mask the effects of the eccentricity and tilt of Miranda's orbit, and that the direct measurements made as described in Section 4 are considerably more accurate and reliable.

One possible source of systematic error in our measurement method would be a misalignment of the diffraction cross from its assumed orientation of 45°. Numerical experiments indicate that changing each measurement of Miranda's position angle by 1° (to compensate for an imaginary orientation error for the diffraction cross) would alter the least-square-fit parameters by amounts on the order of their probable errors. The necessity for such a change is unlikely. It would increase the sum of the squares after best fit by 20%. Moreover, Whitaker has determined the orientation of the cross to be 45° ± ~0.1° by comparing it with the shift of star positions on plates with multiple exposures made at constant declination and different right ascensions.

B. Miranda's orbit

For some time, the five satellites of Uranus have enjoyed the reputation of forming the most orderly system known, with eccentricities and inclinations close to or below the limits of detectability. Our study shows that Miranda is an exception to this remarkable symmetry. Moreover, the Uranus system now contradicts the generality that outer satellites of the major planets tend to have the more irregular orbits. In this sense, the discovery of Miranda's inclination and eccentricity is important evidence for any comprehensive theory of the dynamical properties of the solar system.

Miranda's theoretical apsidal precession rate, $\dot{\tilde{\omega}}$, is given (in degrees/yr.) to a reasonable approximation by

$$\dot{\tilde{\omega}} = 4632 \, J_2 + 4.65 \times 10^4 m_T$$

where the first term represents secular precession due to the oblateness of the planet (J_2 being the dynamical oblateness coefficient) and where the second term represents secular precession due to the other satellites (m_T being the mass of Titania expressed in units of the mass of Uranus) (Dunham 1971). The nodal precession rate is given by $\Omega = -\dot{\tilde{\omega}}$.

Similar equations for the measured apsidal precession of Ariel and Titania in terms of J_2 and m_T allowed Dunham to solve for these constants, yielding

$$J_2 = 0.012 \pm 0.001 \text{ or } 0.034 \pm 0.02$$

$$m_T = (1.0 \pm 0.7) \times 10^{-4}.$$

Two values for J_2 were given because of an ambiguity in the determination of Ariel's precession rate. However, Dunham accepts the lower value as being the more reasonable. With these values, Miranda's precession rate should be $\dot{\tilde{\omega}} = 60° \pm 8°$, corresponding to a period of 6 yr ± 1 yr. Our measurements are not consistent with this period. Using the secular theory, the longer periods that we obtain indicate that J_2 should be about half of Dunham's value. On the other hand, the significant difference between our values for the nodal and apsidal precession periods indicates that the secular theory may be inadequate. As a tentative explanation, we would point out that the circulation period for the Miranda-Ariel-Umbriel near-commensurability is about 12.3 yr and that Dunham's

period for the Ariel precession is about 20 yr, both of the order of magnitude
of Miranda's apparent precession rates. It is thus conceivable that long-period
perturbations, disregarded in the secular theory, may be important. Dr. G. P.
Kuiper points out to us the possibility that the plane of Uranus' equator may
actually be inclined to the mean plane of the four major satellites, a circum-
stance which could conceivably account for the observed precession rates. An
analogous situation exists in the planetary orbits, where the solar equator and
the mean orbital plane of Mercury are both inclined about 7° to the invariable
plane of the Solar System.

In Section 7 we described our original explanation of the surprisingly good
fit of a model with non-zero inclination and no precession. Since the precession
periods are not the expected 6 yr periods equal to 1/2 the intervals between obser-
vation blocks, we must modify the explanation: apparently, the precession periods
are close enough to the observation intervals to explain the fit of the fixed
plane model. It should be emphasized that there are sufficient observations to
define the precession rates unambiguously.

It is possible, however, that other long-period variations due to the near-
commensurability have been disguised by the 12-yr spacing of observations. A few
plates showing Miranda at well-distributed points in its orbit, taken at each op-
position of Uranus over the next few years, could resolve this problem as well as
confirm the orbital parameters. Naturally, in light of our success, we would sug-
gest that such future plates be measured by means of our position-angle method.

Furthermore, our measurement technique might be applied to past and future
images of the other Uranus satellites in order to improve, possibly, the deter-
mination of their orbits and, more specifically, to search for long-period effects
of the near-commensurability.

REFERENCES

Dunham, D. W. 1971, "The Motions of the Satellites of Uranus" (Yale, Doctoral
    Dissertation).
Explanatory Supplement to the Astron. Ephemeris, 1961, H.M. Stationery Office,
    London.
Harris, D. L. 1949, "The Satellite System of Uranus" (Chicago, Doctoral Dis-
    sertation).
Kuiper, G. P. 1949, *Pub. A. S. P., 61,* 129.
Sinton, W. M. 1972, *Sky and Telescope, 44,* 304.
Van Biesbroeck, G. 1965, *LPL Comm. No. 42, 3,* 7-8.
Van Biesbroeck, G. 1970, *LPL Comm. No. 145, 8,* 179-188.

NO. 195 A MODEL OF THE EASTERN PORTION OF SCHRÖTER'S VALLEY

by Ralph Turner

1 March 1973

ABSTRACT

A relief model of the eastern portion of Schröter's Valley has been completed using Lunar Orbiter, Apollo 15, and Earth-based photography. The main results derived from this study are as follows: (1) the head of the Valley (the "Cobra head") is not a simple crater, but rather a slightly-widened section of the Valley emanating from a shield, (2) the east side of the "Cobra head" is a very high peak (2.3 km above the surrounding plains) forming part of a broad shield with an average slope of 12°, and (3) both sides of the Valley display a raised rim in the region measured. These and other observations indicate the Valley was formed by fluid processes, probably lava, and that *the Valley may therefore be a lava drainage channel*, the drained lava presumably underlying the more recent Oceanus Procellarum basalts.

Orbiter V medium- and high-resolution photographs yielded much detail of the Schröter's Valley region of the lunar surface which has made possible the production of a relief model of the entire Valley and its surroundings. This paper describes the first part of a two-part study. The dimensions of the Valley are about half of those of the Grand Canyon in Arizona (3 to 11 km width compared to 6 to 30 km, with the greatest depths 0.8 km compared to 1.6 km, and the total length 160 km compared to 300 or 400 km). Thus, it might be more appropriate to call this Valley a "Canyon". Slopes of the walls often average 30°-40°.

We present results on the eastern half of the Valley based on a carefully composed 3-dimensional scale model. This has been constructed from Orbiter IV and V records and telescopic views (Table I). At a scale of 1:60,000, the model contains information accurate to 100 meters or better (vertically and laterally) for more than 90% of the region modeled. Accuracy was determined by the scale of the model rather than by the resolution of the Orbiter records. Apollo 15 views,

TABLE I

Photographic Records Referred to in Constructing the
Model: Indicating the Range of Illuminations Available.

Designation		Sun Altitude	Sun Azimuth
Orbiter V	M202-206, H202-206	14°.0	5°.1 S. of E.
Orbiter IV	138	4.1	1.2 S. of E.
" "	144	9.6	3.7 S. of E.
" "	150	15.0	6.5 S. of E.
" "	151	15.2	6.5 S. of E.
" "	157	20.6	9.4 S. of E.
" "	158	20.8	9.4 S. of E.
" "	162	26.0	12.3 S. of E.
" "	169	31.4	15.6 S. of E.
" "	174	36.7	19.3 S. of E.
" "	182	41.8	23.4 S. of E.
" "	188	46.7	28.2 S. of E.
Mt. Wilson	226	12.5	6.3 S. of W.
" "	231	1.3	1.4 S. of W.
Lick 120"		64.8	72.2 S. of W.
Catalina 61"	269	11.5	5.3 S. of E.
" "	471	4.6	3.4 S. of E.
" "	1651	2.0	1.4 S. of E.
" "	2391	13.1	4.8 S. of W.
" "	2928	18.2	7.9 S. of W.
" "	3063	2.5	0.4 S. of E.
" "	3105	3.4	1.4 S. of E.
" "	3239	25.5	12.2 S. of E.

recently made available, have been studied after the completion of the model to verify and interpret the area. Advantage was taken of the stereoscopic effects from some of the Orbiter and Apollo records. The method described earlier for integrating information from several sources under simulated illuminations was used (Turner 1970).

The model reveals three characteristics not obvious from the study of any one photograph: (1) The "Cobra head", or southern extremity of the Valley, is not a simple crater, although it appears to be in Orbiter V photographs and in the model when photographed under illumination simulating Orbiter V conditions (Figs. 1 & 2). (2) The east side of the "Cobra head" is a very high peak, forming part of a broad shield-like structure, probably the highest point in the Aristarchus uplift ($A-A^1$, Fig. 3). This is supported by Apollo 15 metric camera stereoscopic comparison. These records also show that specific peaks in this structure have a high albedo (Fig. 4). (3) Both sides of the Valley display a raised rim in the region measured ($E-E^1$, $F-F^1$, Figs. 3 & 5).

The above characteristics were first noted in the Fall of 1970 and are best illustrated by topographic maps taken from the model (Figs. 6 & 7). The maps reveal that the Valley begins as a depression in the side of the large shield, at least 18 km in diameter (Fig. 8). The "Cobra head" is definitely not a bowl-shaped depression but rather a slightly-widened section of the Valley originating on the side of the shield. Cross sections of the Valley illustrate this well ($C-C^1$, $E-E^1$, $F-F^1$, Fig. 3). The Valley maintains a width of about 5 km throughout its length, although it is slightly expanded at the "head" and narrows somewhat at the "tail" (Fig. 4). Sections taken down the Valley (from the "Cobra head" through the plains), a distance of 45 km, show a continuous decrease in elevation of 2.7 km ($D-D^1$, $G-G^1$, Fig. 3), an average of 6%.

The peak immediately to the east of the head of the Valley is very high. It attains an elevation of 2.3 ± 0.1 km above the lowest spot in the plains 10 km due north at 49°04'30"W/24°42'N. This yields an average slope of over 12° ($B-B^1$, Fig. 3). Slopes reach 32° on the flanks of the shield and 46° at the steepest part of the peak ($A-A^{-1}$, Fig. 3). Although the precise elevations of the peak above Oceanus Procellarum cannot be determined until the last half of the model is completed, it is fairly certain that the peak is about 4.5 km higher than the mare at its intersection with the rille.

The topographic map, cross sections, and relief contour map show that *the Valley has raised rims*, in some places attaining elevations of 400 meters above the surrounding plains (Figs. 5 & 9). These are probably natural levees analogous to those found on terrestrial lava drainage channels. Observations of the meanders in the Valley further west show spurs which are opposite to rounded meander banks (Fig. 4). This type of morphology is not characteristic of faulting. The presence of possible natural levees and spurs indicate that the main Valley was the result of fluid processes. Since the Apollo results indicate the absence of a permafrost layer and rock formation under anhydrous conditions, the fluid was probably lava and the Valley therefore a lava drainage channel (Kovach 1972; Charles, et al. 1971).

Lineaments were plotted throughout the region from an Orbiter V photograph (Fig. 1). These were mapped in four general areas (Figs. 10 & 11); (1) The
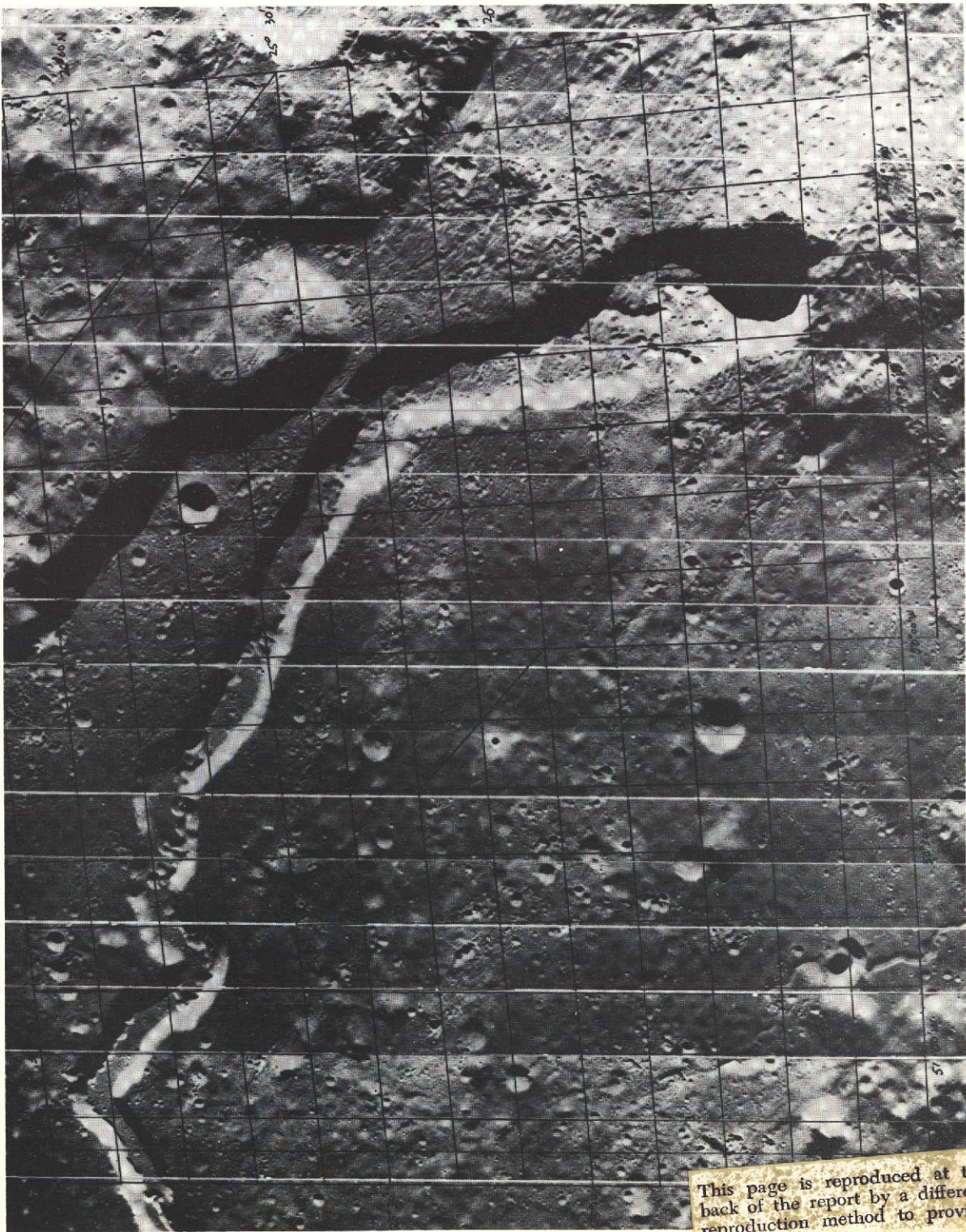
Figure 1   Orbiter V view of eastern portion of Schroter's Valley

(East up)

Figure 2 Relief model of the eastern portion of Schröter's Valley
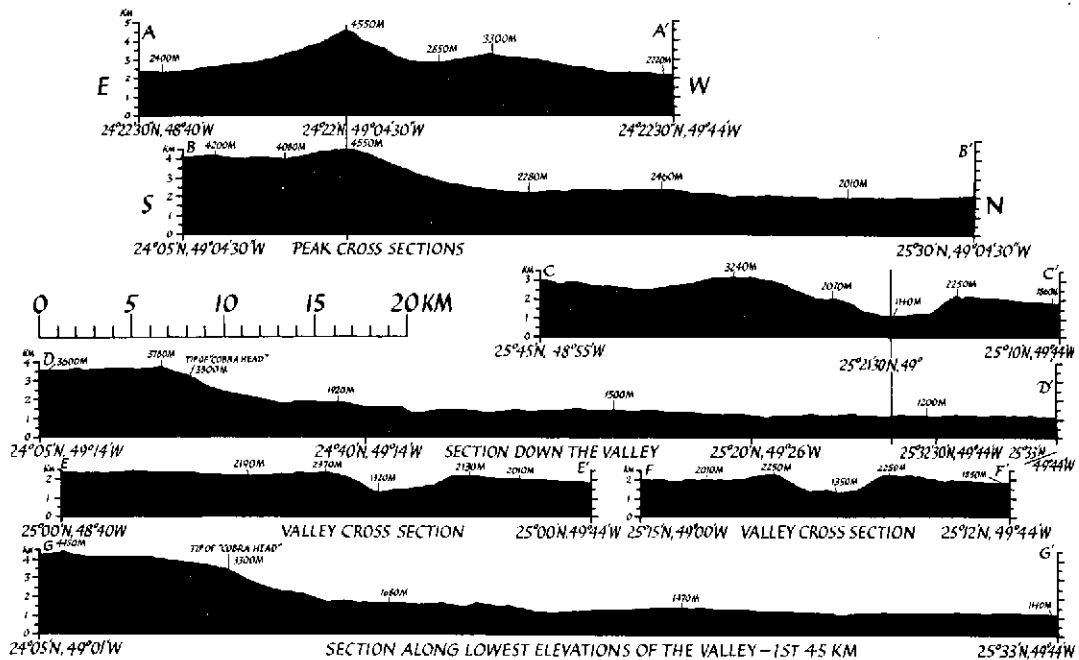(Orbiter V illumination)

(East up)

Figure 3 Schröter's Valley "Cobra Head" cross sections

northern highlands; (2) The shield; (3) The plains and SW hills; and (4) the
Valley walls and floor. In three areas a strong NW trend is present. This trend
to a great extent probably represents strings of secondary impacts from Aristar-
chus. However, many of the NW trending lineaments are major scarps and ridges
which cannot be accounted for by Aristarchus ejecta. Also, the main portion of
the NW trend in the shield area is not radial to Aristarchus (see Fig. 11). There-
fore, at least part of this trend may be tectonic in origin. A NE trend is present
in the northern highlands and shield but not in the other mapped areas. These two
major trends are probably related to the global NW and NE lineament systems (Strom
1969). The apparent absence of a NE trend in the plains - and possibly a NW trend
if the Aristarchus secondaries are removed - may reflect an age difference between
the shield-highlands and the adjacent plains. The plains may represent more recent
lava flows which have largely obliterated the lineaments. The linear portions of
the Valley wall and floor are more or less randomly distributed which suggests they
are not tectonically controlled in the small portion mapped. Detailed mapping of
the remainder of the Valley should help clarify this question.

Another characteristic of this area is an apparent difference in surface
texture. The Valley floor and a portion of the surrounding plain are generally
smoother, more heavily pitted with small craters, and more level than other por-

Figure 4 Apollo 15 view of Schröter's Valley -
with coordinates

(East up)
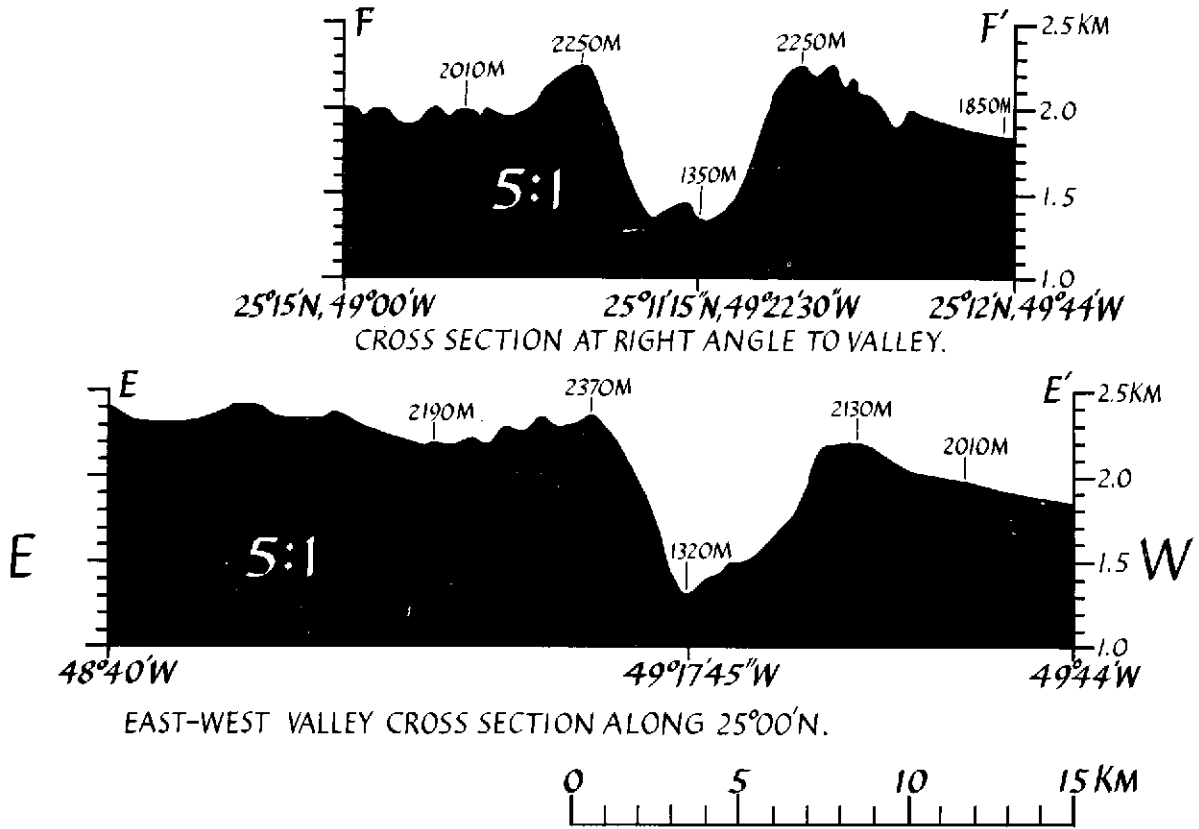
Figure 5 Cross Sections of Schröter's Valley, 5:1 vertical exaggeration

tions of the Aristarchus plateau, i.e. more mare-like in appearance. The rough
highlands and the hills protruding above the plains have a powdery, softened
character with fewer small, sharp pits. This again suggests that the plains may
be mare-type lava flows (Fig. 4).

REFERENCES

Charles, R. W. *et al.* 1971, "H_2O In Lunar Processes", Proceedings of the Second
   Lunar Science Conference, Vol. 1, MIT, Cambridge.
Kovach, R. L. 1972, "Near Surface Lunar Structure", in LUNAR SCIENCE III, re-
   vised abstracts of papers, Houston 10-13 January 1972, ed. Carolyn Watkins.
Strom, R. 1964, "Analysis of Lunar Lineaments. I: Tectonic Maps of the Moon",
   LPL Comm. No. 39, 2.
Turner, R. 1970, "The Northeast Rim of Tycho", *LPL Comm. No. 149,* 8.
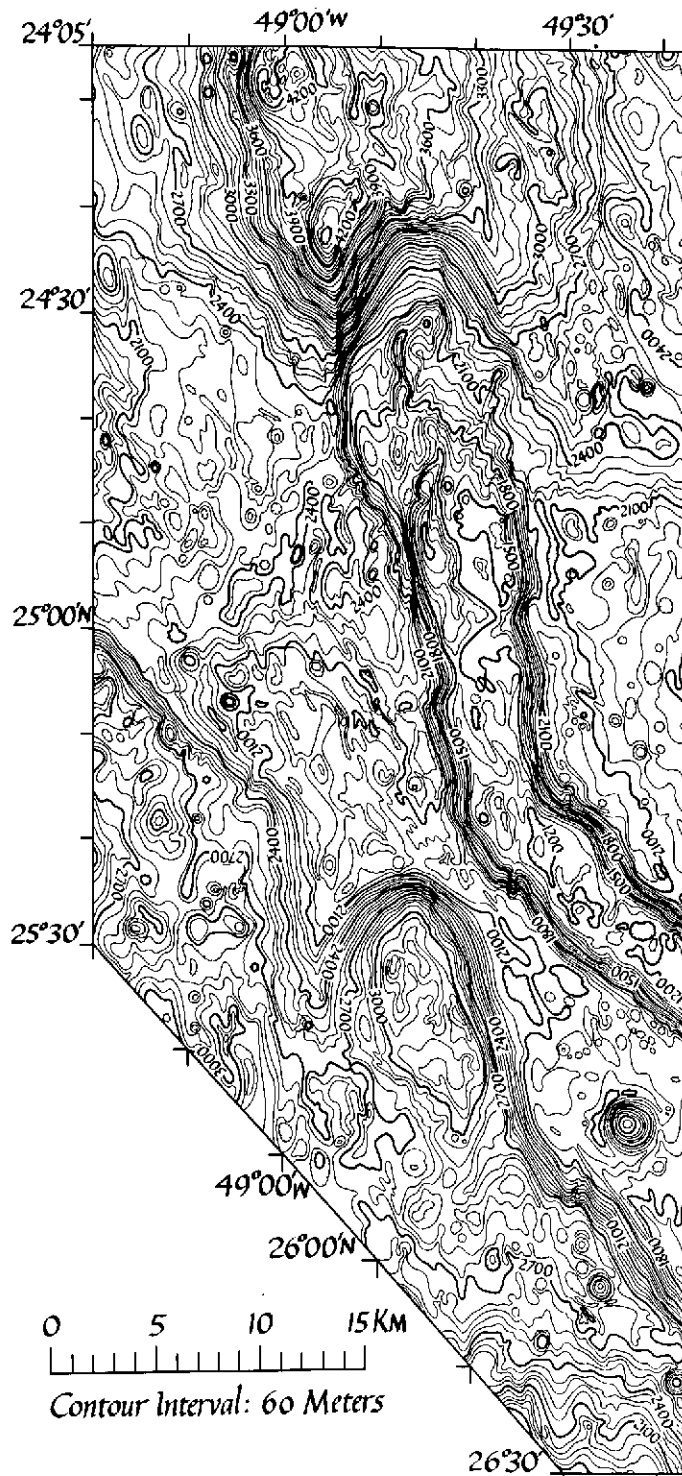
Figure 6   Schröter's Valley contour map
made from model

(South up)
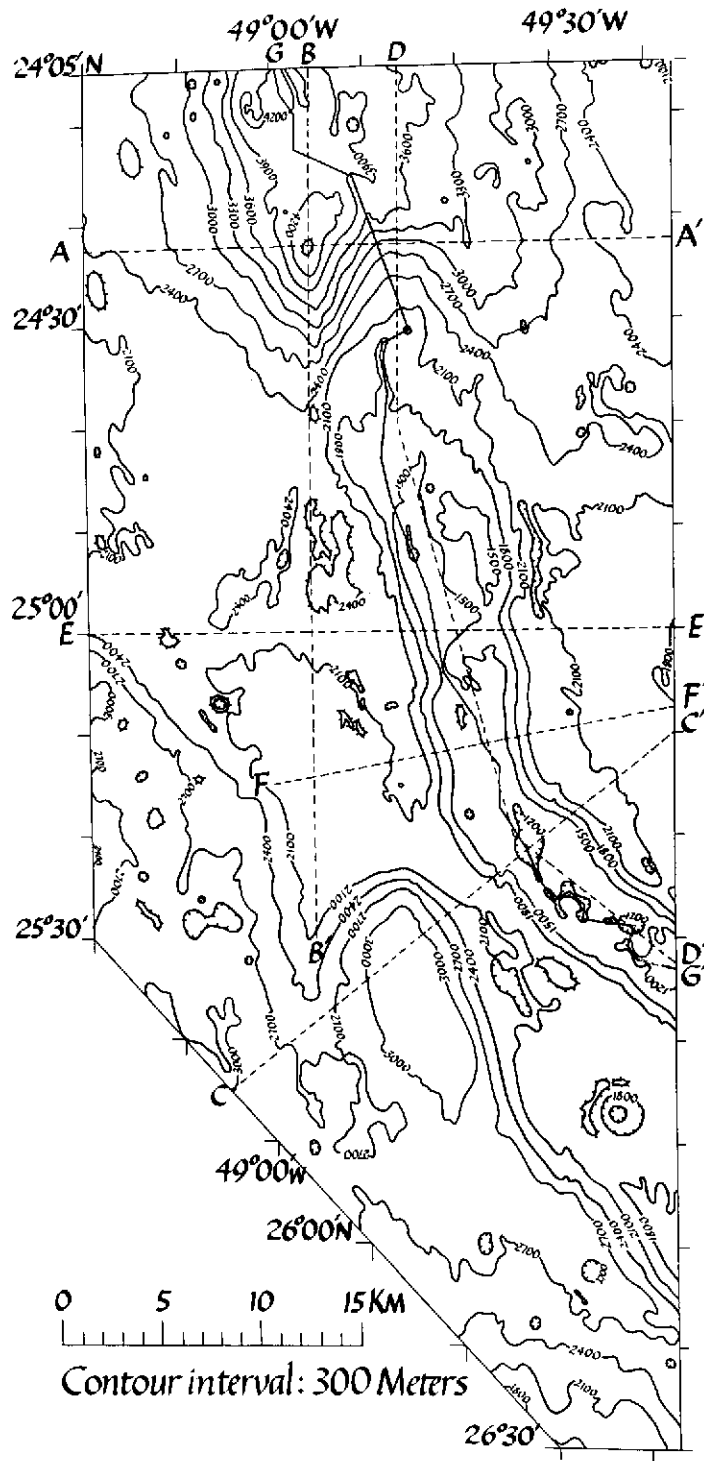
Figure 7 Topographical map of the east portion
of Schröter's Valley - 300 m contour interval

(South up)
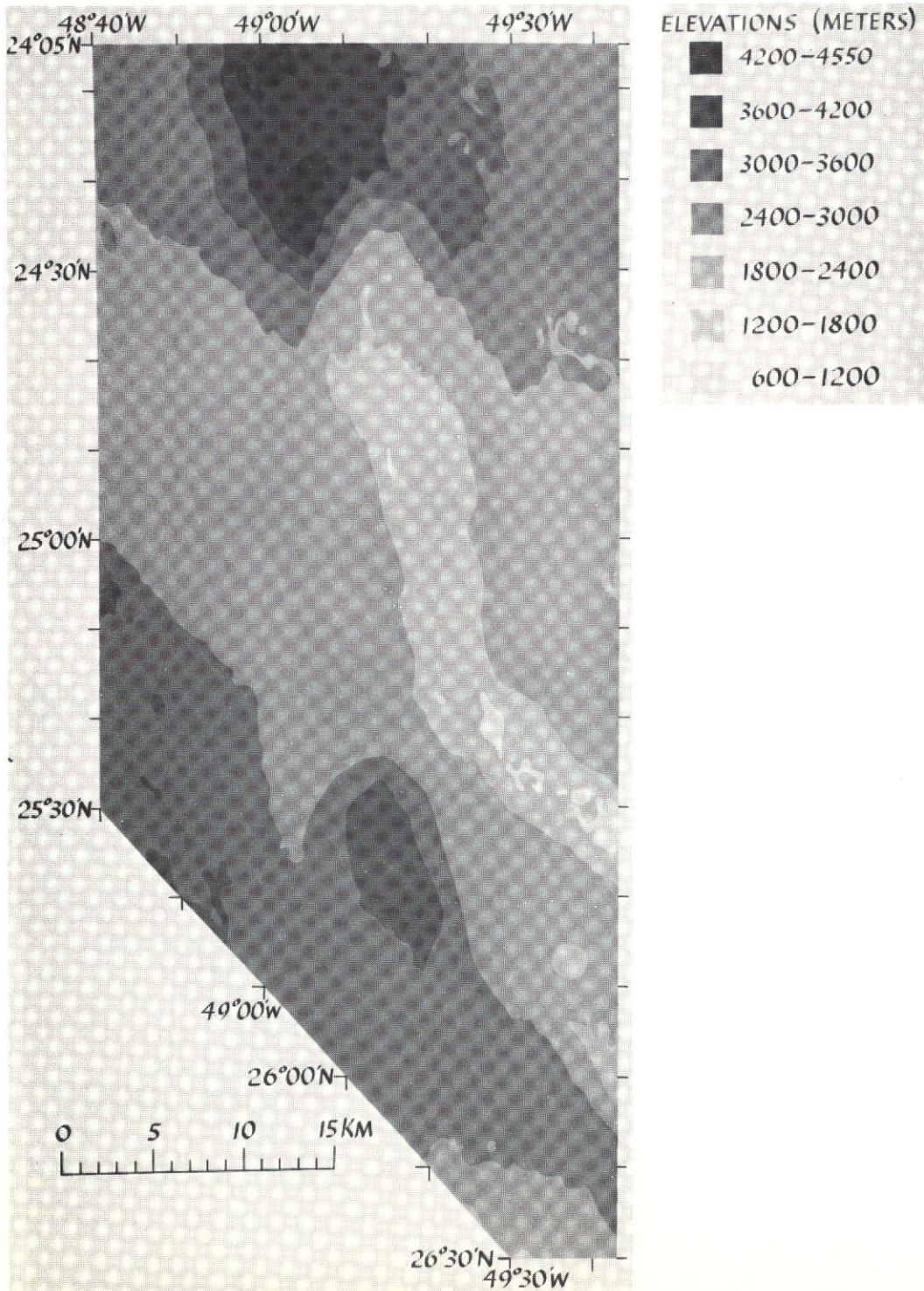
Figure 8 Equal height map of Schröter's Valley from model
(South up)
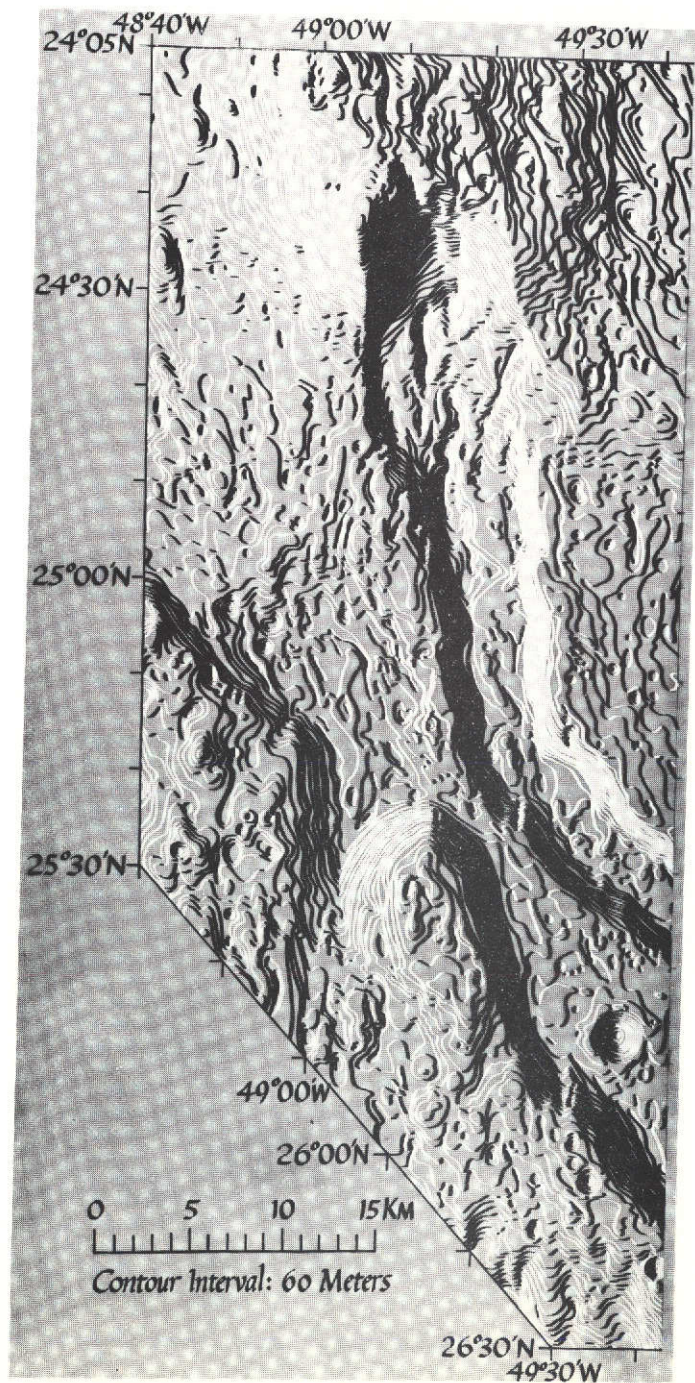
Figure 9   Relief contour map from Schröter's
Valley Model I

(South up)
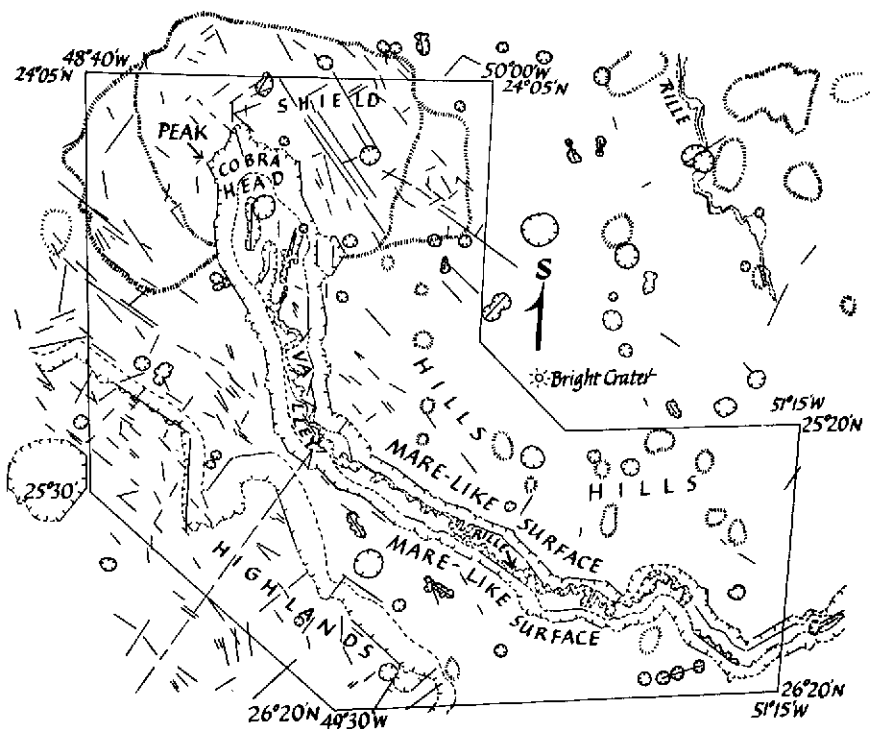
Figure 10   Identification of features and lineaments
in the Schröter's Valley area
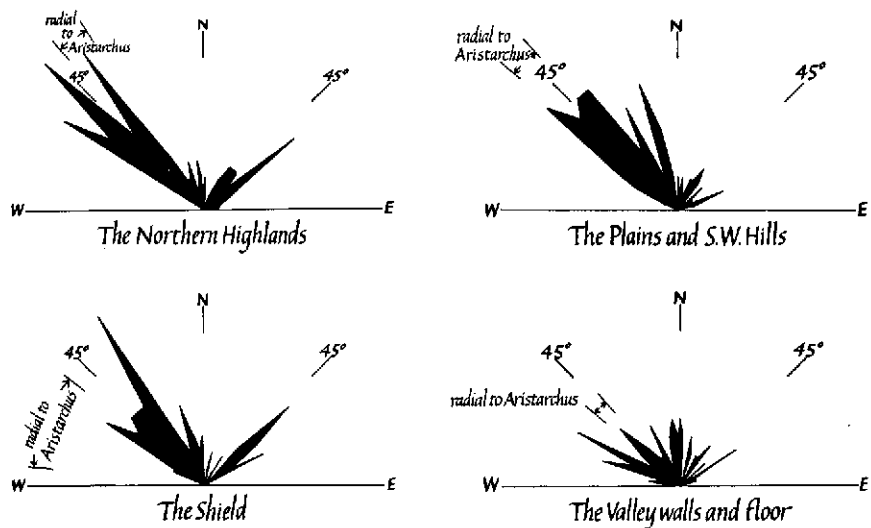
Figure 11   Lineaments in the Schröter's Valley area

TABLE OF CONTENTS